Fundamental Studies of Corrosion on Soft Metal/Lubricant Interfaces Using X-ray Spectroscopy

James Michael Bucag

University of Leeds

School of Chemical and Process Engineering

Submitted in accordance with the requirements for the degree of

Doctor of Philosophy

July 2023

Intellectual Property Statement Acknowledgement

The candidate confirms that the work submitted is his own and that appropriate credit has been given where reference has been made to the work of others.

This copy has been supplied on the understanding that it is copyright material and that no quotation from the thesis may be published without proper acknowledgement.

The right of James Michael Bucag to be identified as Author of this work has been asserted by James Michael Bucag in accordance with the Copyright, Designs and Patents Act 1988

Acknowledgements

First and foremost, I wish to extend my deepest and sincerest gratitude to Prof. Sven Schroeder, Dr. Anna Kroner, and Dr. Andrew Britton for their unwavering patience and unwavering encouragement throughout the duration of this project. Without their invaluable guidance and support, this thesis would not have reached its completion.

I am indebted to all those who directly contributed to this work. To Thokozile Kathyola, Gunjan Das, Saphora Dabo, Paul Edwards, and Oliver Towns, I am grateful for your contributions to the beamtime at I18. A special mention goes to Peter Nicholson, Ed Woodhouse, Rob Harris, and Scott Prichard for their unparalleled expertise in providing design advice and fabricating the necessary components for the TEY devices.

I also wish to express my heartfelt appreciation to Dr. Beth Willneff and Dr. Andrew Britton for their invaluable assistance with my XPS measurements. Also, to Dr. Nathan Hollingsworth, Mr. Oliver Delamore, Mr. Marcus Popowicz and Prof. Peter Dowding for their support of this project. This work has greatly benefited from their expertise.

Thank you to my loving family for their support throughout my academic pursuit. I am indebted to my parents for their sacrifices, without which everything I have accomplished would not have been possible. I am also grateful to my sister, Lolo, Lola and the rest of my extended family for their encouragement and pushing me to finish.

To my girlfriend Camille, who has always supported me unconditionally. She was always there to pick me back up when I was down. You were always at your best even when I couldn't be my best. Thank you for everything.

Thank you to my elite office mates, Anuradha Pallipurath , Bethan Evans, Arturs Pugejs and Rosi Elliott, I look forward to the next time we go to a musical! To Bradley Tyson, I'll miss our rivalry. And to many others that has changed my PhD life for the better.

I would also like to give my deepest gratitude to the medical physics team at Torbay. Thank you for encouraging me and allowing me the flexibility to finish this work.

Table of Contents

List of Figures

xi

List of tables

List of Nomenclature

Pb	Lead
Sn	Tin
Sb	Antimony
SEM	Scanning Electron Microscopy
EDX	Energy Dispersive X-ray
VI	Viscosity Index
SN	Synthetic Naphtha
NMR	Nuclear Magnetic Resonance
BE	Binding Energy
NCC	Naphtha of Catalytic Cracking
PAO	Polyalphaolefins
FWHM	Full Width at Half Maximum
HPLC	High-Performance Liquid Chromatography
MS	Mass Spectroscopy
FT-IR	Fourier-Transform Infrared Spectroscopy
ESCA	Electron Spectroscopy for Chemical Analysis
IMFP	Inelastic Mean Free Path
ISO	International Organization of Standardization
CHA	Concentric Hemisphere Analyzer
HSA	Hemisphere Sector Analyzer
XANES	X-ray Absorption Near Edge Spectroscopy
XAFS	X-ray Absorption Fine Structure
LCF	Linear Combination Fitting
UHV	Ultra-High Vacuum
FY	Fluorescent-yield

S	Sulphur
BO	Bridging Oxygen (BO)
NBO	Non-Bridging Oxygen
XRD	X-ray Diffraction
TEM	Tunnelling Electron Microscopy
FIB	Focused Ion Beam

Covid Statement

The pandemic severely impacted the experimental work required for this thesis. No practical work was conducted with the laboratory closed (March – October 2020). From October 2020, though the laboratory was accessible, COVID-19 precautions created barriers to the overall workflow. Bookings were required one week in advance. This made the experimental workflow slower than usual. In addition, during the early opening of CaPE, limited staff was available to support research activities.

In addition, synchrotron experiments have been postponed several times and could only be completed in December 2021 (4th year of the project). Furthermore, due to travel restrictions imposed by the pandemic, other synchrotron-related experiments have been limited.

Abstract

Automotive engine corrosion presents a significant economic and engineering challenge, with estimated global costs reaching billions.[1] The main research focus has been on the steel components of engines, but copper has traditionally been used in critical engine parts due to its high heat conductivity and there is an increasing use of Cu-based alloys in the main engine components.[2,3] Cu is known to be susceptible to corrosion by common lubricant additives such as zinc dialkyl dithiophosphates (ZDDP) and molybdenum dithiocarbamate (MoDTC). The mechanistic details of Cu corrosion by these additives are essentially unknown. The research reported in this thesis therefore sought to obtain information on the mechanisms of Cu corrosion by MoDTC and ZDDP in typical lubricant phases at elevated temperature. To achieve practical relevance, studies of Cu corrosion were performed under the conditions of the high-temperature corrosion bench test (HTCBT), which is widely used in commercial lubricant R&D for the qualitative assessment of metal corrosion by lubricant formulations. Advanced surface characterization techniques, including X-ray Photoelectron Spectroscopy (XPS) and X-ray Absorption Spectroscopy (XAS) were used to determine the chemical species and phases formed on Cu metal surfaces. The strong corrosive effect of MoDTC on Cu was immediately apparent, revealing the chemical nature of dark tarnish layers developed within a short time interval, and tracing its slow chemical transformations to substantial Cu_2S corrosion layers. For ZDDP, results revealed varying tarnish compositions as a function of its concentration in the lubricant. As for MoDTC the corrosion ultimately forms Cu_2S as the final product. In addition to characterizing the corrosion of Cu surfaces by MoDTC and ZDDPs, developments of surface-sensitive *operando* and *in situ* techniques for XAS analysis by total electron yield (TEY) detection were carried out. An *in situ* XAS cell was designed to subject metal samples to HTCBT conditions, allowing for multi-modal XAS characterization with sensitivity to bulk and surface speciation, as well as the detection of impurity species. Integration of a TEY detector for an existing research tribometer for real-time surface characterization during tribological testing was demonstrated.

1 Introduction

The global annual cost of automotive corrosion in 1999 was estimated to be $23.4 billion (£18.2 billion).[1] Corrosion is an electrochemical reaction occurring on metal surfaces due to environmental factors. Corrosive reactions involve the loss of metal atoms from the surface, weakening the structural integrity of the material/component leading to failure. A fundamental understanding of the physical and chemical corrosion processes is essential to engineer a system to inhibit corrosion.

In the 1920s, corrosion in the crankcase had generally been believed to be driven by generating sulphuric acid. Sulphur compounds, contained in low-grade fuels and lubricating oils, react with oxidisers and water that enter or are generated in the engine.[4] Sulphuric acid can be formed, which can react with the walls of the cylinder and crankcase, forming rust on the steel.[5] Ever since the invention of formulated lubricants, the additive systems in the formulation thus incorporated detergents to neutralize acids and prevent acid corrosion.[6] Although adding detergents in lubricant formulation has addressed acid corrosion, other lubricant components introduced to protect steel may themselves corrode other metals in the engine. The mechanisms of these non-aqueous corrosion processes are not very well understood. Popular lubrication additives, such as zinc dialkyl dithiophosphate (ZDDP) and molybdenum dithiocarbamate (MoDTC), have raised concerns, as they have been found to be corrosive to copper (Cu).

Due to environmental concerns, lead (Pb)-based alloys used in bearings in the crankshaft are being phased out in favour of Cu-based alloys.[3] Cu is found in various engine components, including bearings, pistons, and oil coolers, where its corrosion can significantly impact the performance and longevity of the engine. Due to the increasing use of Cu-based alloys in engines, understanding the corrosion of Cu surfaces has become a critical issue. The American Society for Testing and Materials (ASTM) D6594, also known as the high temperature corrosion bench test (HTCBT), is an industrial test used to screen for an oil formulation's affinity to corrode soft metals such as Cu.[7] Following the test, the surface of the Cu metal is

visually inspected and given a rating. By its very nature such ratings have a strong subjective element and do not provide insight into the chemical nature of the surface of Cu and hence the corrosion products and the mechanism of their formation.

The research reported in this thesis sought to identify chemical phases formed at the lubricant/Cu metal interface, combining the HTCBT and advanced X-ray characterization techniques such as X-ray photoelectron spectroscopy (XPS) and X-ray absorption spectroscopy (XAS). As part of this effort, *operando* and *in situ* cells for the surface characterization of metals by total-electron-yield (TEY) detection of X-ray absorption spectra were developed, which will also be described.

Before discussing the characterization of Cu surfaces in subsequent chapters, Chapter 2 will provide a literature review that establishes the context for the entire body of work reported here. This review offers a concise overview of Cu's significance in engines, lubricants, and its susceptibility to corrosion. Furthermore, the fundamental principles of XPS and XAS, the primary characterization techniques utilized throughout this research, are introduced. This foundation of knowledge lays the groundwork for the subsequent analyses but also enhances the understanding of the corrosion behaviour of Cu in lubricants within the context of engine technology.

In Chapter 3, an outline of this thesis' overarching goals and specific objectives. This section serves as a guide for readers through the core intentions of this body of research.

In Chapter 4, an investigation of the corrosive action of MoDTC using a combined XAS and XPS approach will be presented. MoDTC is found to have a strong corrosive affinity to Cu, with a dark tarnish layer observed to form on the surface within a short time scale. It is found that the corrosion is initiated by the reaction of Cu with base oil followed by a reaction with degradation products of MoDTC.

The corrosion mechanism of ZDDP on Cu was also studied using XPS and the results will be discussed in Chapter 5. The chemical composition of the tarnish found on the surface of the Cu is altered by varying the ZDDP concentration. The study was built on the knowledge that

the submersion of Cu in a heated ZDDP solution forms a phosphate-based thermal layer. This thermal layer is profiled using Ar$^+$ etching, and the results are compared with previous literature.

Chapter 6 presents the advancements in developing surface-sensitive *in situ* and *operando* techniques. Chapter 6 discusses the design and commissioning of an *in situ* XAS cell specifically designed for multi-modal measurements. This cell is designed to subject metal samples to HTCBT conditions. These developments enable the characterization of metal surfaces by XAS using the integrated TEY detector, enhancing our ability to explore the behaviour of additive systems and the surface properties of metals in response to operating conditions.

In addition, Chapter 6 also presents the design and commissioning of a novel TEY detection system to facilitate the characterization of additive systems in *operando* conditions. The primary objective is to integrate this TEY device into an existing tribometer, allowing for the real-time evaluation of additives during tribological testing. Integrating the TEY detection system into *operando* tribological investigations and the novel *in situ* XAS cell opens up exciting possibilities for additive structure/performance research.

Overall, the body of work in this thesis aims to address automotive Cu additive corrosion, a costly global issue that weakens metal surfaces and weakens the structural integrity of vital components. Through a comprehensive literature review, we establish the context for our research, emphasizing the importance of understanding the chemical corrosion processes to devise effective corrosion inhibition strategies. The investigation focuses on the corrosion of Cu surfaces, especially concerning the increasing use of Cu-based alloys in engines and their susceptibility to corrosion from lubricant additives.

2 Literature Review

2.1 Copper

2.1.1 Use in Engines

2.1.1.1 Oil Cooler

Due to its high thermal conductivity, copper (Cu) is commonly found in the engine's oil coolers,[8] where it efficiently conducts and transfers the heat of the engine oil to the cooling circuit; this heat removal is critical to the continuous operation of the engine, so the heat exchanger in the oil cooler is one of the most extensively exposed Cu surfaces during engine operation.

2.1.1.2 Pistons

Pistons are a central component of engines. Pistons convert energy from fuel combustion to linear motion (Figure 2.1.1). Cast iron and steel pistons were originally used in automotive engines, but modern technology uses pistons cast out of aluminium (Al) alloys, reducing weight and engine vibrations during operational use.[3] Al has a high coefficient of thermal expansion compared to iron-based materials. The design of pistons needs to account for an optimum clearance at running temperatures. However, with many Al alloys, the clearance would be too large at lower temperatures, leading to excessive engine vibrations. To address this, Cu is added to Al alloys, lowering the coefficient of thermal expansion.[3]

2.1.1.3 Bearings

The crankshaft is another central engine component. The crankshaft converts the linear motion of the pistons to circular motion (Figure 2.1.1). Bearings are used to reduce the energy lost through frictional forces. The bearing must combine good wear resistance, embeddability, conformability, and a degree of corrosion resistance.[2] Modern automotive engines use tin/antimony/lead (Sn/Sb/Pb) or Sn/Sb/Cu alloys in bearings. However, with growing

environmental concerns, Pb-alloys in bearings are being phased out in favour of Cu-based alloys developed to replace them.[9–12]
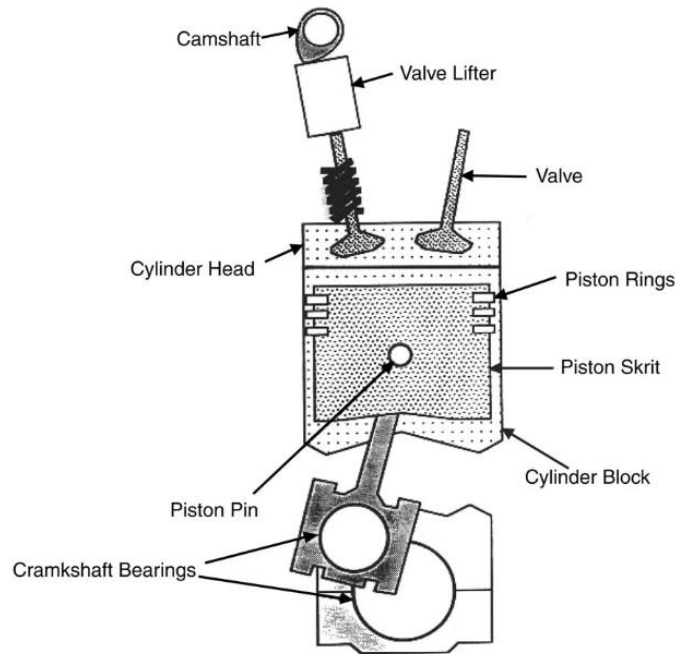
Figure 2.1.1 Schematic depiction of a single cylinder from an overhead camshaft engine.[3]

The elemental composition of a coating found on bearings consists typically 76% Cu, 22% Pb, and 2% Sn, with a Pb/Cu matrix providing the bulk overlayer. This coating is often used on hard steel because it balances soft and hard material requirements under the conditions of engine operation.[3,13] Often, Sn is used as an overlayer, which can provide corrosion protection due to its relative chemical stability under engine operation conditions.[13,14] Corrosion of this Sn layer can be due to faults with its manufacturing (inhomogeneous Sn layers) or due to mechanical processes wearing and/or damaging the Sn layer. With lead being phased out in the automobile manufacturing industry due to adverse environmental impact, Cu has become of greater importance.[14]

2.1.2   Industrial Corrosion Test

Before fully formulated lubricant oils are manufactured and sold to consumers, they must pass several standardized tests. Industrial tests are designed for rapid turnaround, convenience, and

economic benefit compared to field testing. For example, the ASTM D130 and ASTM D6594 are industrial corrosion tests used to examine the oil formulations' affinity to corrode soft metals such as Cu. These mimic the conditions in an engine; however, to an extent, they also oversimplify the corrosion process in an engine.

2.1.2.1 ASTM D130

The ASTM D130 immerses a Cu coupon in an engine oil held at 100°C for 3 hours.[15] The result of the analysis is obtained by comparing the colour of the Cu tarnish to a qualitative rating chart (Figure 2.1.2).
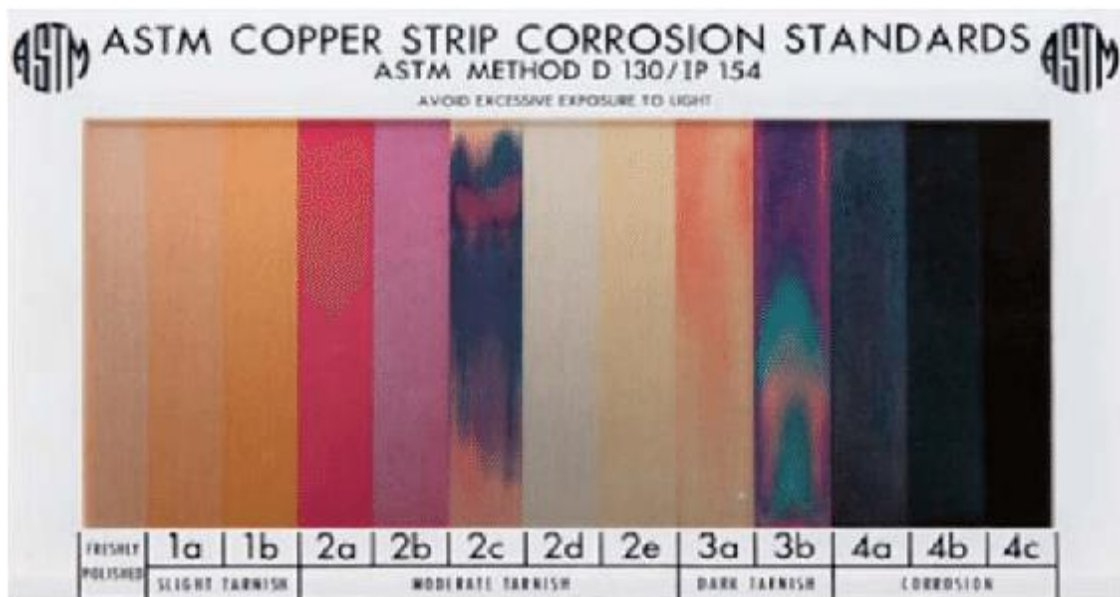
Figure 2.1.2 ASTM D130 Cu corrosion chart.[16]

2.1.2.2 High Temperature Corrosion Bench Test (HTCBT)

ASTM D6594, also known as the High-Temperature Corrosion Bench Test (HTCBT), immerses Cu, Sn, Pb, and phosphor bronze coupons in oil at 135°C for 168 hours while bubbling air through the oil at a rate of 5 L/h.[15] The result is compared to the same chart as in ASTM D130. However, the test also accounts for the dissolution of the metal in the oil. The

coupon must not lose more than 0.002% by mass, and dissolved metal must not exceed concentrations over 5 ppm.[15]

Since HCTBT comprises a constant supply of air, it is, therefore, likely that the products of antioxidants in the oil formulation will play a more prominent effect in the HTCBT than the ASTM D130, where the reaction of sulphur in the form of sulphides or even elemental sulphur may be more critical.

2.1.3 Oxidation of Cu Surfaces
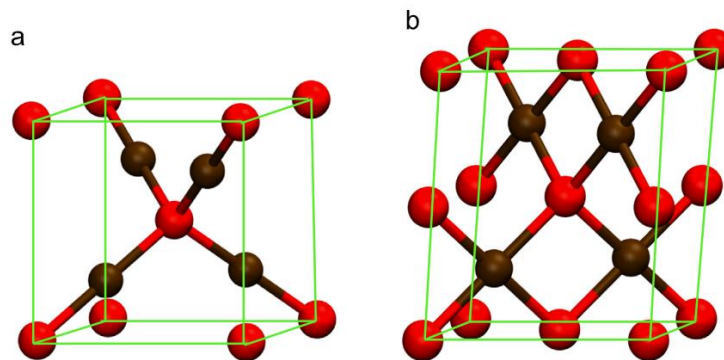
Figure 2.1.3 Molecular model of the crystal structure of (a) cuprous oxide Cu_2O and (b) cupric oxide CuO. Red balls represent oxygen and brown balls Cu. The unit cell is shown in green. From ref([17]).

There are two primary forms of Cu oxide, cuprite (Cu_2O) and tenorite (CuO), with Cu oxidation states of +1 and +2, respectively. Paramelaconite (Cu_4O_3) is another form of Cu oxide, a mixed Cu^+/Cu^{2+} oxide with an overall oxidation state of +1.5. It is a rare mineral found in hydrothermal deposits of Cu.

The preparation of Cu samples for industrial tests is carried out in ambient air. Under ambient air, Cu quickly oxidizes at the surface, forming an oxide overlayer. It is this native oxide overlayer that reacts with the oil formulation in the industrial tests, and therefore an understanding of this native oxide layer is essential for the mechanism of Cu corrosion.

7
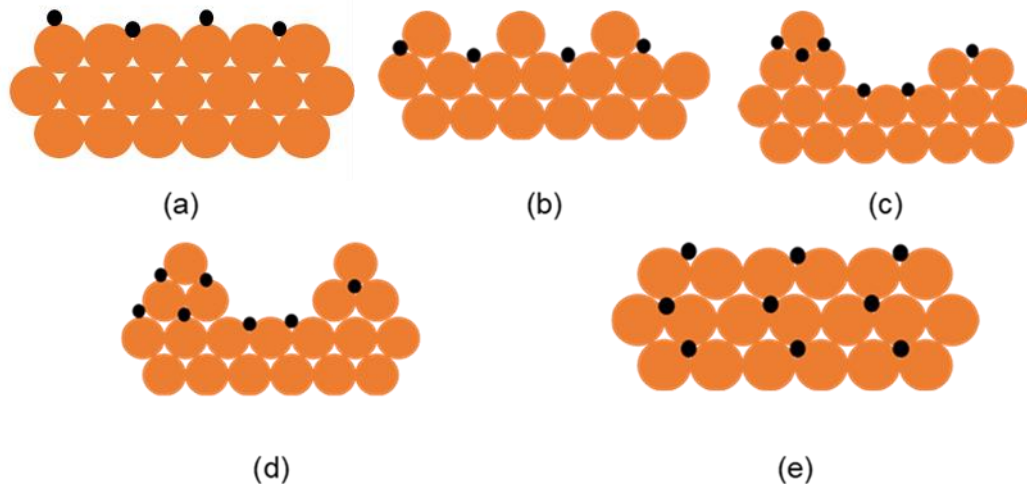
Figure 2.1.4 Diagram of the five stages of Cu oxide grown by the reaction with Cu metal. (a) adsorption of oxygen molecules and clean Cu surface. (b) Reconstruction of the Cu surface. (c) Nucleation of oxide islands upon diffusion of oxygen on the reconstructed surface. (d) Growth of the oxide islands. As the islands grow bigger direct oxygen impingement on the islands starts playing a more important role. (e) Oxide growth proceeds through the interfacial diffusion of oxygen.

O_2 reacts with Cu metal surface to form Cu_2O in five stages (Figure 2.1.4):

i) **Chemisorption of gas-phase oxygen.** Oxygen adsorbs dissociatively on Cu surfaces at room temperature with activation barriers of ~ 0.1 to 0.3 eV depending on the surface facet exposed to the oxygen (Figure 2.1.4 a).[17] Different types of adsorbed oxygen species can be formed, including sub-surface oxygen species.

ii) **Reconstruction of the Cu surface.** Cu and adsorbed oxygen atoms at the surface and sub-surface rearrange to minimize the surface energy (Figure 2.1.4 b).[18]

iii) **Nucleation of oxide islands** (Figure 2.1.4 c). A reconstructed Cu surface with adsorbed oxygen slows down further adsorption of oxygen. Therefore, additional physisorbed O_2 molecules diffusively migrate below towards higher-Cu concentration areas, vacancies, or surface defects, where they can dissociate and form adsorbed atomic oxygen species.[19–21] The diffusion of O atoms on the reconstructed (100)-surface has a barrier of 1.3 eV.[21] Nucleation of oxide islands requires overlayers with a minimum dimension of ~4 Å to form.[22] The oxide island morphology and the time required to reach saturation density depend on temperature, with higher temperatures requiring a much shorter time to saturation.[17]

iv) **Growth of the oxide islands** (Figure 2.1.4 d). The nucleated oxide islands begin to grow laterally until they merge. Several models have been proposed to explain the growth of these islands based on oxygen impingement and surface diffusion.[23] A model proposed by Yang et al., based on oxygen impingement and surface diffusion, fit well experimental data on Cu(100), with island growth proportional to $t^{1.3}$.[23]

v) **Oxide growth proceeds through the interfacial diffusion of oxygen**. An early *ex situ* study of Cu oxide formation at a temperature range of 50°C to 150°C concluded that Cu_2O is formed with a rate law of $y^n = kt$, where y is the thickness of the oxide layer, t is the time elapsed, and n is a temperature-dependent exponential parameter.[24]

According to Platzman et al., the oxidation process of a Cu surface in the presence of ambient air can be described using three distinct phases.[25] In the first phase, a surface layer of Cu oxide (Cu_2O) is formed, which aligns with the Cabrera-Mott model.[26] After the formation of Cu_2O, a metastable layer of Cu hydroxide ($Cu(OH)_2$) is generated. Finally, the metastable $Cu(OH)_2$ layer transforms, leading to a more stable Cu oxide (CuO) layer. This is consistent with some reports where the formation of a ~ 2.0–5.0 nm Cu_2O initial layer is followed by ~ 0.9–1.3 nm CuO overlayer.[25,27–29]

Preparing the Cu surface before oxidation also plays a role in determining the characteristics of the final oxide overlayer formed. According to Lim et al., the texture and microstructure of a thin Cu film directly influence the properties of the resulting oxide film.[30] When oxidizing a sample with a columnar structure and small grains, a bilayer of Cu_2O/CuO was observed. Conversely, when oxidizing a uniformly prepared sample without a prominent columnar structure or grain boundaries, only a layer of cuprous oxide (Cu_2O) was observed, and the oxidation process occurred at a slower rate.[30]

2.1.4 Copper Corrosion

Cu corrosion poses significant challenges in various applications, including nuclear waste management, heat exchangers, and water supply pipes.[31–33] In these scenarios, corrosion

primarily occurs in aqueous environments. Cu corrosion manifests differently in non-aqueous environments, such as electrical transformers and engine lubrication systems. Non-aqueous Cu corrosion is particularly relevant in applications such as insulating transformer oil and lubricating oils, where the oil often contains sulphur-based additives.[16]

In engine Cu corrosion, carboxylic acids are produced in free radical chain reactions of hydrocarbons (discussed in section 2.2) and by fuel combustion.[34] These acids can be neutralized by directly reacting with metal surfaces. This is one chemical path to the corrosion of any metals in contact with the lubricant in the engine. As discussed in section 2.1.1, many essential engine components contain Cu. One of the driving forces for Cu corrosion in engines is reactive sulphur compounds. The reaction of Cu with these sulphur compounds is well known to produce Cu (I) sulphide (Cu_2S).[35] Cu_2S is black and constitutes the major component of the dark tarnish observed in the ASTM D130 Cu corrosion chart (Figure 2.1.2).

Many additives in oil lubrication contain sulphur and are used for various functions, such as alkyl polysulphides as antioxidants, zinc dialkyl dithiophosphate (ZDDP) as an antiwear additive, and molybdenum dithiocarbamate (MoDTC) as a friction modifier. Sulphur-containing additives play a crucial role in effective lubricants. However, sulphur has a strong affinity to Cu, which drives corrosion.[35] In addition to the sulphur-containing additives added to base oil, some base oils may contain sulphur (this is discussed further in section 2.2). These are in the form of elemental sulphur and thiol-like compounds. Operating engine conditions are highly oxidating and could oxidise elemental sulphur to produce SO_x ($x = 1 - 3$). Complete oxidation of SO_x would form SO_3, which could react with the residual water in the engine to produce H_2SO_4 (sulphuric acid).[36] Similarly, with thiol compounds, their reaction with hydrogen peroxides leads to the formation of sulfonic acid.

2.1.4.1 Use of SEM/EDX to probe Cu corrosion

A previous study by scanning electron microscopy (SEM) and energy dispersive X-ray (EDX) analysis systematically investigated the effect of Cu corrosion by thiol using the ASTM D130 conditions.[37,38] The studies measure the corrosion by quantifying the amount of sulphur on the surface of the Cu coupon with EDX. One of the interesting findings from this study is that the

hydrocarbon matrix containing elemental sulphur may reduce its corrosive affinity to Cu (Figure 2.1.5).[37] Synthetic naphtha (SN) contains 70% petroleum ether and 30% benzene. In contrast, non-corrosive naphtha or naphtha of catalytic cracking (NCC) contains mainly alkanes. Adding 2% NCC in the matrix can significantly reduce the sulphur on coupons.
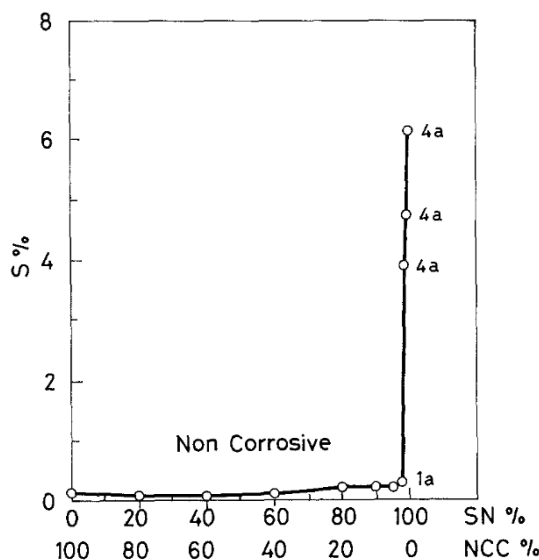
Figure 2.1.5 Sulphur concentration on the Cu coupon measured by EDX vs the ratio of synthetic naphtha (SN) to non-corrosive naphtha (NCC naphtha of catalytic cracking). The elemental sulphur concentration in the mixtures is 20 mg/L. The label on the data points is the visual rating of the Cu pound based on the ASTM D130 corrosion chart.[37]
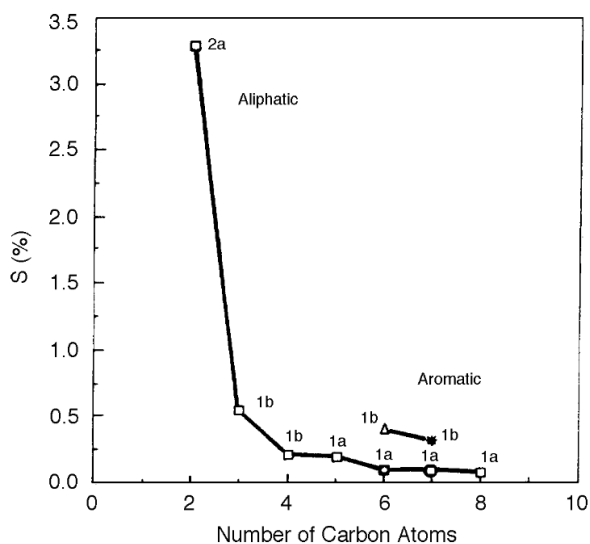
Figure 2.1.6 Sulphur concentration on the Cu coupons obtained by EDX vs the thiol's carbon linear/aromatic chain length. The label on the data points is the Cu coupon's visual corrosion rating based on the ASTM D130 corrosion chart.[38]

11

The effects of the thiol alkyl chain length on corrosion were also investigated using the same methodology. It was found that the sulphur concentration on the Cu coupons decreases with increasing chain length (Figure 2.1.6).

These corrosion studies give insightful results. However, the visual ASTM D130 corrosion chart rating, paired with the quantification of the sulphur on the coupon's surface (by EDX), is only partially conclusive. The visual rating is subjective and assumes that the dark black tarnish is Cu_2S. EDX provides only the elemental composition, but no chemical information for the elements and hence cannot confirm the presence of Cu_2S. Some of the results from these studies are internally inconsistent. For example, for an increasing concentration of elemental sulphur mixed in naphtha (Figure 2.1.7),[37] at a lower concentration of sulphur, ~1-2 ppm, the resulting ASTM D130 ratings are 4a. However, at larger concentrations of sulphur, >3 ppm, the rating is 2d or 2e while having a greater sulphur concentration on the Cu coupon.[37] This would indicate that the sulphur species are deposited on the surface but do not react with Cu to form Cu_2S and do not contribute to a black tarnish. The EDX data collected does not provide the required chemical information to identify the sulphur species deposited.
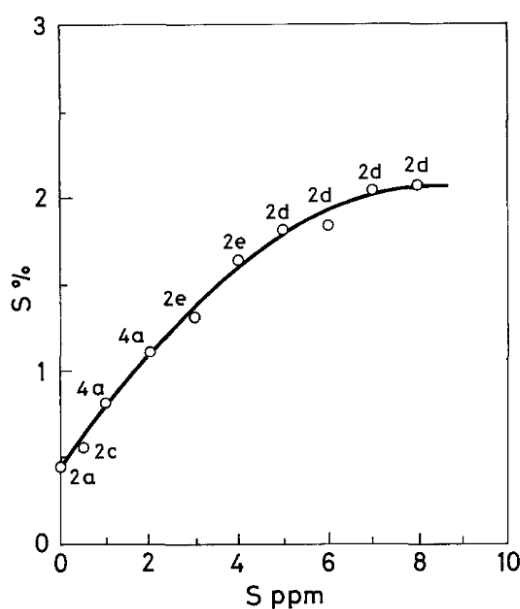
Figure 2.1.7 Sulphur concentration on the Cu coupon obtained by EDX vs. the sulphur concentration in the naphtha.[37]

2.1.4.2 Use of XPS to probe Cu corrosion

Comparable studies have been carried out by X-ray photoelectron spectroscopy (XPS) by Reid et al.[39] XPS has a greater surface sensitivity than EDX. While EDX has a bulk probing depth on the order of μm, XPS is sensitive to the top 1-10 nm near the surface. The difference in probing depth was noticeable in the quantification of the sulphur. In studies done by EDX, the quantification of sulphur is 0.5–6% (Figure 2.1.5 and Figure 2.1.6), while XPS indicates concentrations in the range 2–25% (Figure 2.1.8). In EDX, the probing depth probes below the tarnish layer (into the bulk Cu), while XPS probes selectively the tarnish layer. XPS can also provide chemical information on the measured elements detected on the surface via the chemical shifts of the core-level binding energies. Interestingly, the visual ASTM D130 rating provides a greater corrosion rating than the measured sulphur content on the surface of the coupon. For example, the measured sulphur concentration on the surface of the Cu is larger than for surfaces with a lower ASTM D130 rating (Figure 2.1.8). This would indicate that the sulphur is deposited on the surface but does not react with Cu to form Cu_2S, similar to the EDX studies.

Reid et al. included XPS measurements of S $2p_{3/2}$ binding energies. However, it fails to provide sufficient information to identity the sulphur species on the surface, such as the full width at half maximum (FWHM) and the values of spin-orbit splitting used for the fitting.[39] Furthermore, the study lacks crucial details regarding the energy calibration in XPS, which prevents confident comparison and validation with other results reported in the literature.
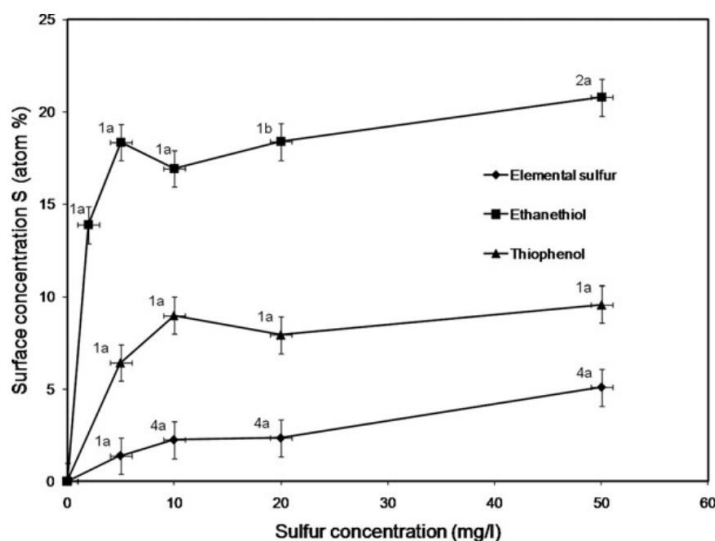
Figure 2.1.8 Surface sulphur concentration in the surface of the Cu coupon with elemental sulphur, thiophenol, or ethanethiol vs the sulphur concentration in solution. The corresponding ASTM D130 visual test ratings are indicated.[39]

In contrast, although not as comprehensive, XPS studies of sulphur corrosion of Cu by Welbourn et al. offer a better description of the energy calibration procedure.[40] Unfortunately, since the data and the fitted components are not presented in the publication, independent evaluation of the validity of the analysis is not possible. Assessing the reliability of the binding energy reported for the S 2p is difficult. XPS characterization of the Cu surface was performed after submersion in a non-aqueous solution of 1-hexadecane thiol. The authors report three photoemission peaks at 161.64 eV, 162.48 eV, and 163.32 eV, corresponding to sulphides and elemental sulphur.[40] It is unclear whether the author meant three doublet peaks (since the p orbitals exhibit spin-orbit splitting) with the S $2p_{3/2}$ peaks taking binding energy positions 161.64 eV, 162.48 eV, and 163.32 eV or if the spectra are fitted inappropriately with three independent components positions at 161.64 eV, 162.48 eV, and 163.32 eV. In addition, the full width at half maximum (FWHM) of the peaks is also not reported, making any determination impossible whether the components fitted to the data are appropriate.

As discussed previously, polysulphides are used as antioxidants in lubricant formulations. The sulphur bridges can cleave, producing thiols and elemental sulphur. Such S-S bond cleaving

is facilitated by acidic conditions.[16] Disulphides may also incorporate elemental sulphur from the solution, increasing the length of the sulphur bridge.[41]

2.2 Lubricant Oil

2.2.1 Base Oil

2.2.1.1 Base Oil Groups

Lubricating engine oils contain additives, including antioxidants, detergents, etc., suspended in base oil. Base oil composes 75-85% of the oil lubricant volume. There are four fundamental properties of base oils that dictate their performance within an engine:[4]

- Pour point – The lowest temperature at which the oil is too viscous to flow is the pour point.
- Viscosity - A measure of the oil's resistance to flow. The viscosity is, of course, a function of temperature.
- Viscosity Index (VI) – The VI measures the viscous response to a change in temperature. The higher the VI, the less the viscosity increases with temperature.
- Purity – Constituents of many lubricants, such as sulphur, nitrogen, and polycyclic aromatic compounds, must be held within strict limits.

From a performance viewpoint, manufacturers prefer base oil with a high VI that works over a larger temperature range. The American Petroleum Institute classifies base oil into five groups. As seen in Table 2.2.1, the groups are defined by their components and performance characteristics.

For example, a group I base oil has a VI in the range of ≥ 80 and ≤ 120, which is relatively low. In addition, oils in this the Group contain upwards of 0.03% sulphur, which is highly detrimental to Cu, and less than 90% saturates. From the VI and constituents, it is easy to explain why Group I base oil demand is declining, although they are still the largest single category in the global market.[4]

Group	Sulphur Content (%)	Saturates (%)	Viscosity Index (VI)
I	≥ 0.03	< 90	$80 \leq VI \leq 120$
II	≤ 0.03	≥ 90	$80 \leq VI \leq 120$
III	≤ 0.03	≥ 90	$VI \geq 120$
IV	synthetic polyalphaolefins; no sulphur, no saturates		$125 \leq VI \leq 200$
V	any other type of base oil		

Table 2.2.1 The table gives some typical values of the Sulphur, saturate, and Viscosity Index. Adapted from[4].

Group II and III base oils have similar purities, characteristically containing 99% saturates, and are obtained by hydroprocessing. The two oils can be distinguished by their VI with Group III having VI value of 120 or greater.[4]

Group IV consists of polyalphaolefins (PAOs), the traditional synthetic stocks. Using mixtures of different alphaolefins, formulators can create oils with a VI as high as 140. However, the use of these oils is severely limited by the cost and availability of feedstocks, which face competition from other applications.[4]

Group V embraces everything else, from low-quality naphthenics to exotic synthetic oils. Other occupants of this group are organic esters, compressor oil, some biodegradable fluids, and polyethylene glycols that are extremely non-flammable and thus suited for use as high-temperature hydraulic fluid.[4]

2.2.1.2 Thermal Oxidation of Base Oil

Hydrocarbon chains in base oil can undergo free-radical chain reactions. These self-accelerating reactions consist of four stages: initiation, propagation, chain branching, and termination.[34,42] The initiation phase begins with forming peroxy radicals (Reaction 2.2.1). R refers to the alkyl hydrocarbon chain, and k_1 is the reaction rate constant. This initial reaction

is very slow with a rate constant of $k_1 = 10^{-10}$–10^{-9} dm^3 mol^{-1} s^{-1}. Transition metal ions can catalyze and accelerate this reaction.[34,42]

$$RH + O_2 \underset{k_1}{\rightarrow} R\bullet + HO\text{-}O\bullet$$
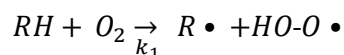
Reaction 2.2.1 The initial step of the free radical chain reaction forming alkyl radical and hydroperoxide radicals

Although the initiation is very slow, its products are reactive, so the subsequent reactions are relatively fast. For example, the reaction rate constant for the second step, k_2, has typical values of $10^7 - 10^9$ dm^3 mol^{-1} s^{-1}.[34,42] In the propagation phase, alkyl radicals, R•, from Reaction 2.2.1 quickly react with oxygen to create an alkyl peroxy radical.

$$R\bullet + O_2 \underset{k_2}{\rightarrow} R\text{-}O\text{-}O\bullet$$
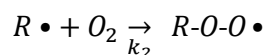
Reaction 2.2.2 Formation or alkyl peroxy radical from alkyl radicals

The alkyl peroxy radicals can further react with other hydrocarbons to regenerate alkyl radicals (Reaction 2.2.3). These reactions are much slower than Reaction 2.2.2 with reaction rate constant $k_3 = 10^{-5}$–10^{-1} dm^3 mol^{-1} s^{-1}.[42]

$$R\text{-}O\text{-}O\bullet + RH \underset{k_3}{\rightarrow} R\text{-}O\text{-}OH + R\bullet$$
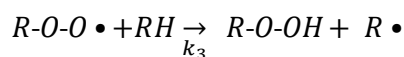
Reaction 2.2.3 Regeneration of alkyl radicals by reaction of hydroperoxides radical with hydrocarbons.

17

The chain branching phase differs based on the concentration of hydroperoxides present. Where there is a low concentration of hydroperoxides, the hydroperoxide group can produce alkoxy and hydroxyl radicals (Reaction 2.2.4).[34,42] This reaction requires a high activation energy and only occurs at temperatures over 120°C

$$R\text{-}O\text{-}O\text{-}H \rightarrow R\text{-}O \bullet + OH \bullet$$

Reaction 2.2.4 Fragmentation of hydroperoxides to alkoxy and hydroxyl radicals.

The alkoxy radical can react further with other hydrocarbons to regenerate alkyl radicals (Reaction 2.2.5).

$$R\text{-}O \bullet + RH \rightarrow R\text{-}O\text{-}H + R \bullet$$
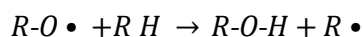
Reaction 2.2.5 Reaction of alkoxy radical with hydrocarbons from alcohols and alkyl radicals.

Similarly, the hydroxy radical can react with other hydrocarbons to form water and alkyl radicals (Reaction 2.2.6).

$$HO \bullet + RH \rightarrow H_2O + R \bullet$$
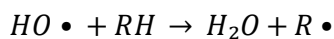
Reaction 2.2.6 Reaction of hydroxy radical with hydrocarbons from water and alkyl radicals.

At higher concentrations of the chain branching phase of the alkyl hydroperoxides, more complex reactions could occur via a bimolecular mechanism (Reaction 2.2.7).[34]

$$R\text{-}O\text{-}O\text{-}H \ + \ R\text{-}O\text{-}O\text{-}H \ \rightleftharpoons \quad \begin{matrix} R\text{-}O\text{-}O\text{-}H \\ \vdots \quad \vdots \\ H\text{-}O\text{-}O\text{-}R \end{matrix} \quad \rightarrow R\text{-}O\text{-}O \bullet \ + R\text{-}O \bullet \ + H_2O$$
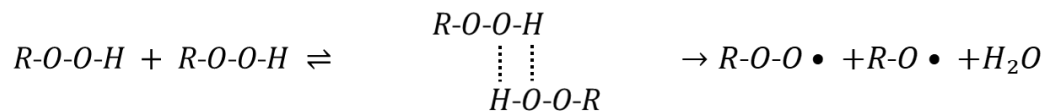
Reaction 2.2.7 Two hydroperoxides forming hydroperoxides radicals, alkoxy radical, and water.

There is a large number of different radicals that form in free radical chain reactions; these radicals recombine in different combinations, forming a wide range of products, including alkanes, ketones, esters, organic peroxides, aldehydes, and alcohols (Reaction 2.2.8). [34,42] Aldehydes and alcohols further oxidize to produce carboxylic acids.

$$R \bullet \ + R \bullet \rightarrow R - R$$

$$R \bullet \ + R\text{-}O\text{-}O \bullet \rightarrow R\text{-}O\text{-}O\text{-}R$$

$$R \bullet \ + R\text{-}O\text{-}O \bullet \rightarrow R\text{-}O\text{-}R$$

$$R\text{-}C\text{-}O\text{-}O \bullet \ + R\text{-}O\text{-}O \bullet \rightarrow R\text{-}(C = O)\text{-}R + R\text{-}OH$$
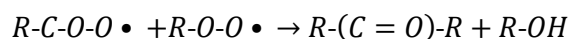
Reaction 2.2.8 Termination reactions producing a range of products.

2.2.2 Zinc Dialkyldithiophosphate (ZDDP)

Zinc dialkyldithiophosphate (ZDDP) is a multi-functional additive added to lubricant formulation primarily for its anti-wear but also anti-oxidation and anti-corrosion properties.[6,43,44] Since its introduction in the 1940s, it has remained one of the most popular additives used commercially. Several companies have attempted to identify an alternative to ZDDP over the last 30 years, but a cost-effective compound with similar anti-wear

performance is yet to be identified.[6] As ZDDP contains sulphur moieties, it has an intrinsic propensity to corrode Cu.
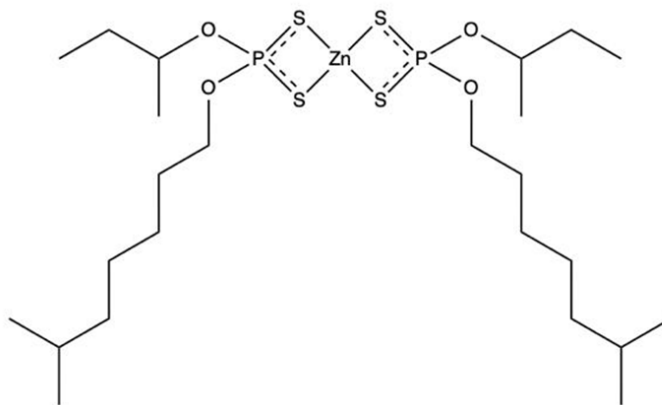
Figure 2.2.1 Chemical structure of Zinc bis[O-(6-methylheptyl)] bis[O-(sec-butyl)] bis(dithiophosphate). In a general structure of ZDDP the sec-butyl and 6-methylheptyl can be any alkyl group, R

Under conditions of friction ZDDP forms a glassy zinc thiophosphate tribofilm on surfaces that protect against wear. The phosphate tribofilms formed by ZDDP are typically 50-150 nm thick and stabilize at this level. These films form pad-like structures on the metal surface.[45,46] On their outside, the 'pads' are zinc polyphosphate, while pyro-orthophosphates are in their bulk.[45,46] These pad-like structures have an indentation modulus of 90 GPa and a hardness of 3.5 GPa, as measured by AFM and nanoindentation at room temperature.[6] Similar films are formed on the surface of certain metals such as Cu when submerged in a heated ZDDP solution (temperatures > 100°C). These films are similar to tribofilms.[47]

The antioxidant nature of ZDDP is due to its ability to scavenge peroxy-radicals, retarding the free-radical chain reaction occurring in the oil. Furthermore, dithiophosphate can also scavenge metal ions via a ligand substitution displacing the Zn^{2+}. Dissolved in solution and on metal surfaces, metal ions such as Cu and Fe can catalyze the free-radical chain reaction. Finally, ZDDP can also decompose peroxides. A summary of the main antioxidant mechanisms of ZDDP is summarised in Figure 2.2.2, taken from Willermet et al.[48]

20

ZDTP: zinc dialkyldithiophosphate; [(RO)$_2$P(S)S]$_2$Zn
HDTP: dithiolic acid; (RO)$_2$P(S)SH
BZDTP: basic ZDTP; [(RO)$_2$P(S)S]$_6$Zn$_4$O
DS: (RO)$_2$P(S)S-SP(S)(RO)$_2$; DS•: (RO)$_2$P(S)S•

DS — +ROOH → ROO
DS ←
BZDTP ← +ROOH −ROH ← ZDTP → +H$_2$O → HDTP → +ROOH −ROH
+ROOH −ROH   H$_2$O
+ZnO   −H$_2$O   (RO)$_2$P(S)SZnOH
−ZnO   +ROOH −ROH   (RO)$_2$P(S)SOxH
(RO)$_2$P(S)SZnOCR″
+ROO +O$_2$ −SO$_2$ +H$_2$SO$_4$ +ROOH −R″CHO   −SOx^{-1}
ZnSO$_4$
(RO)$_2$P(S)OH   H$_2$O   +ROOH −R′CHO   H$_2$SO$_4$ (RO)$_2$P(S)OR   (RO)$_2$P(S)OH
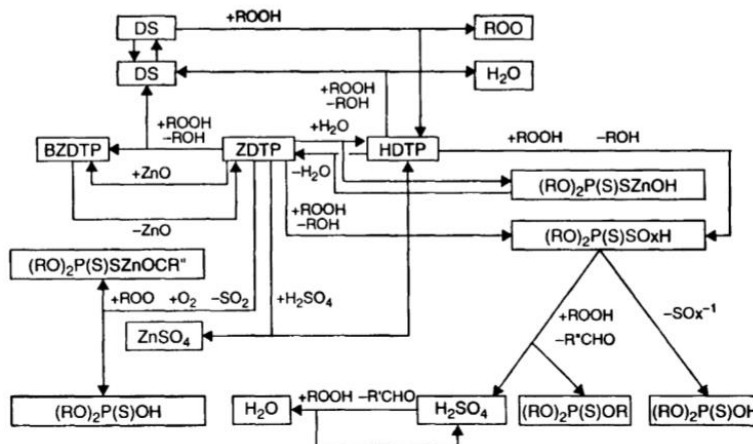
Figure 2.2.2 Chemical pathways of ZDDP antioxidant action.[48]

Although ZDDP has been in use since the 1940s, until the 1980s, there was considerable debate about the mechanistic chemical pathways taken by the additive during its thermal decomposition.[6,49] Thiophosphates are also an essential class of insecticides, and great efforts have been made to understand their chemical properties.[50]

A fundamental property of thiophosphate is that they are highly alkylating agents, allowing self-propagating reactions with neighbouring dithiophosphate to form the dithionylphosphate isomers (Figure 2.2.3).[6,49] This has been confirmed using ^{1}H- and ^{31}P-NMR.[49]
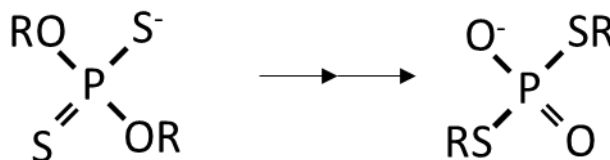
Figure 2.2.3 Alkyl exchange process from O to S in diphosphates. The doble arrows denote the formation of intermediate species during the reaction pathway.

The polymerization of dithionylphosphate into polythiophosphates generates thiols as a by-product[6,49] Thiols cause detrimental corrosion of Cu, as already discussed in section 2.1.4.

2.2.3   Molybdenum Dialkyldithiocarbamate (MoDTC)

Molydenum-containing compounds were first introduced as anti-wear additives in the 1950s.[50–52] A method of synthesizing Molybdenum dialkyldithiocarbamate (MoDTC) was first documented in a patent in 1964.[53] Molybdenum-containing additives, including MoDTC, continued to be used as anti-wear additives until the late 1970s when MoDTC and other molybdenum-containing additives began to be used as a friction modifier.[52,54] MoDTC continues to be used as friction modifiers in modern lubrication formulations with secondary functions as extreme pressure and antioxidant additives.[50]

The ability of MoDTC to reduce friction between sliding surfaces is due to the formation of MoS_2.[55–61] It was generally thought that friction reducing ability of MoS_2 is due to its ability to shear along crystallographic planes held together by weak van der Waals forces.[62] However, more recent computational studies have suggested that repulsive Coulomb repulsion between the sulphur layers rather than the weak van der Waals forces are responsible for this behaviour.[63] An alternative to MoDTC is using MoS_2 as a directly solid additive in lubrication formulation.[64] A limiting factor in using dispersed MoS_2 in oil is its solubility. The oil soluble MoDTC is easier to include in the formulation as a precursor to MoS_2, which is then formed under operation conditions and reduces friction.[65]

A mechanism for the conversion of MoDTC to MoS_2 has been suggested by Grossiord et al.[66] The proposed mechanism is shown in is shown in Figure 2.2.4. It begins with the cleaving of the Mo-S bond, forming •$Mo_2O_2S_2$ and two secondary amine radicals. The two secondary amine radicals can recombine forming a thiuram disulphide. The $Mo_2O_2S_2$ radical further decomposes to MoO_2 and MoS_2.[66]
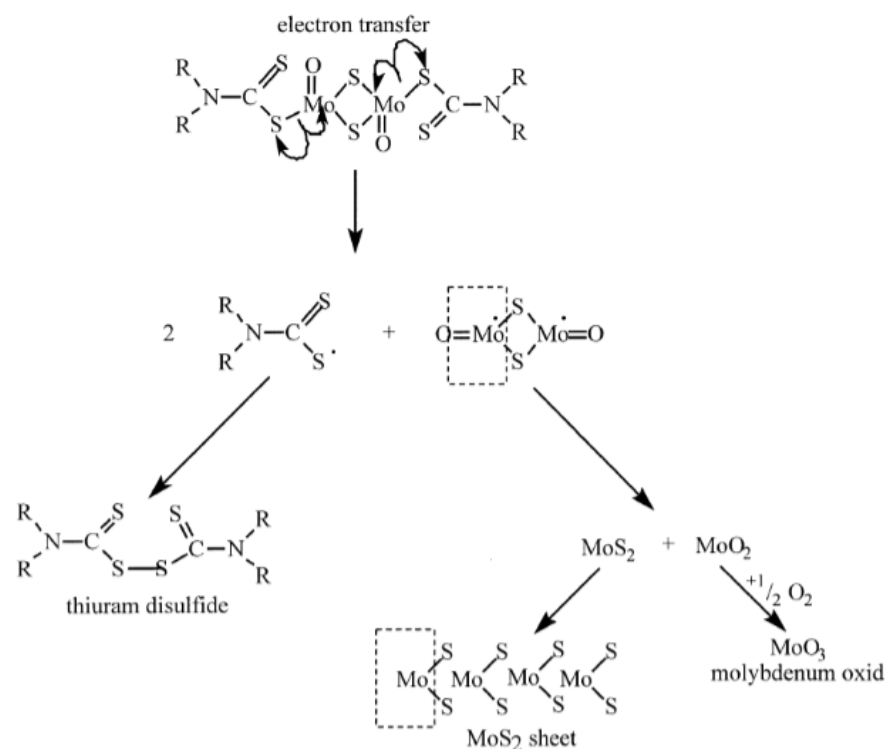
Figure 2.2.4 Chemical decomposition of MoDTC to Mo_2S and MoO_2/MoO_3 and thiuram disulphide.[66]

The decomposition of MoDTC was more recently examined by a combination of high-performance liquid chromatography (HPLC), Fourier-transform infrared spectroscopy (FTIR), and mass spectroscopy (MS).[67] The study suggested that non-stoichiometric MoS_xO_y particles form. This chemical path is initiated by isomerism and a reaction with oxygen, omitting two sulphur atoms from the molecule. This product then decomposes, forming secondary amines CO_2 and MoS_xO_y particles.

MoDTC is an essential component of commercially available fully formulated lubricants to reduce friction and increase efficiency. However, as for ZDDP, MoDTC is known to have a detrimental corrosive reaction with Cu.[68] The mechanism of this corrosive reaction is unclear and requires further investigation.

2.3 X-ray Photoelectron Spectroscopy (XPS)

2.3.1 History of XPS
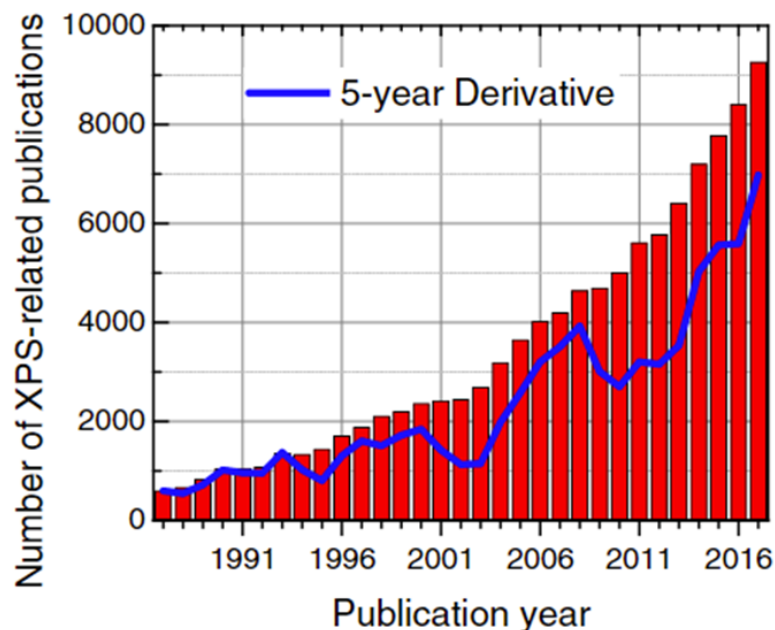
Figure 2.3.1 Number of publications per year where XPS was used based on a Scopus database search performed in June 2018 for the term "XPS." From ref([69])

Photoelectron emission is a phenomenon first observed by Heinrich Hertz in 1887. However, this phenomenon remained unexplained until 1905, when Albert Einstein suggested the photoelectric effect that won him the Nobel prize in 1921. X-ray-induced photoelectron emission was observed, in 1914 by Robinson and Rawlinson, but it was not until much later, in 1951, that Steinhardt and Serfass demonstrated how photoemission could be used as an analytical method. The development of its analytical power was enabled by K. Siegbahn's work through the 1950s and '60s, shaping the technique as it is known today. The work done towards developing electron spectroscopy for chemical analysis (ESCA) won Siegbahn the Nobel prize in 1981. XPS is a highly versatile characterization technique providing surface-sensitive, element-specific, chemical, and electronic information. Since the technique's development, spectrometers have only become more user-friendly, opening the technique to a broader user base. As a result, XPS has become one of the most utilized material

characterization techniques in many areas, such as material science, chemistry, engineering, and physics. Figure 2.3.1 shows the number of publications relating to XPS, showing an exponential-like increase over the years from 1987, showing an exponential like increase in the publications.[69]

2.3.2   Binding Energy
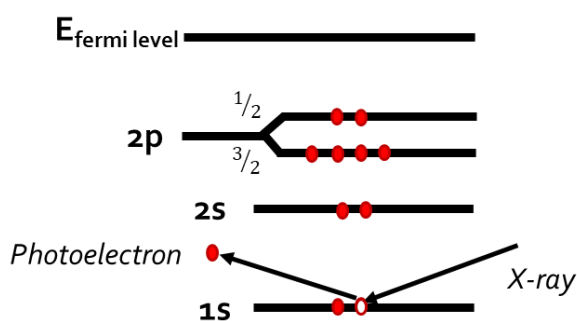
Figure 2.3.2 Visually represents the photoelectric effect with an X-ray interacting with a 1s electron.

XPS is based on the photoelectric effect (Figure 2.3.2). Monochromatic X-ray photons are incident on the sample interacting with core-level electrons. The X-ray transfers its energy to the core-level electron. If the energy of the photon (hv) is greater than the binding energy (E_B), $hv > E_B$, the electron escapes the atom as a photoelectron with a particular kinetic energy (E_k).

Considering the conservation law, an expression for E_B can be made using E_k and hv.

$$E_B = hv - E_k$$

Equation 1

Equation 1 is known as the basic photoelectric equation. In XPS, the spectrum measured shows photoemission peaks that can be analysed to obtain the value of E_B, giving valuable insight into the chemical and electronic nature of the element that is the origin of the photoemission event.

E_B can be further formalized by considering Coulomb interactions as the photoelectron escapes the material. Equation 2 is an expression for E_B for a core-level, C.

$$E_b(C) = E_b{}^{(n)} + qk + V - R^{ea} + qR^a(n)$$

Equation 2

$E_b{}^{(n)}$ is the binding energy of the core electron C in a free atom (with n valence electrons), q is the valence charge, k is the change in core potential resulting from the removal of a valence electron, V is the Madelung potential, R^{ea} is the relaxation energy associated with the rest of the system, that is with the flow of electron density from the surrounding toward the core-ionized atom, $qR^a(n)$ is the atomic relaxation energy lost ($q > 0$) or gained ($q < 0$) by the ion in the compound with respect to the free atom.[70] The binding energy shift relative to its elemental form is often called the chemical shift.

Qualitatively dissecting Equation 2, it is shown that due to the $E_b{}^{(n)}$, XPS can provide element and core-level specific information. Furthermore, the E_B can also give information on the oxidation state of the chemical species present from the terms qk and V, respectively. Finally, electronic R^{ea} and $qR^a(n)$ provide electronic information.

2.3.3 Photoemission Line Shape

Due to the uncertainty principle, the probability density function (PDF) of electronic energy levels within atoms is Lorentzian in nature. However, due to intrinsic phenomena occurring in the samples (such as phonon coupling) and instrumental factors, the final line shape measured will have some Gaussian character.[71,72] The final line shape is a convolution of a Lorentzian and Gaussian function known as a Voigt function.[72] Analytically, the weighting of Gaussian or Lorentzian components in a Voigt function is altered by defining a mixing parameter $glmix$ from the Gaussian (ghm) and Lorentzian (lhm) FWHM,

$$glmix = \frac{lhm}{lhm + glm}.$$

Equation 3

When *glmix* = 1.0, the Voigt function is purely Lorentzian; conversely, when *glmix* = 0, the function is purely Gaussian.

For metals, the line-shape often has a more dominant Lorentzian character. This is because metals have a low-energy acoustic phonon, while compounds have optical phonons, increasing vibrational broadening for these peaks, and thus increasing the Gaussian characteristics. Metals also have an asymmetric line shape. This is due to the photoelectron's interaction with the conduction band, resulting in a "tail" towards the higher binding energy range.[71]

2.3.4 Full Width at Half Maximum (FWHM)

The shapes of photoemission lines are often characterised by their full-width at half maximum (FWHM). Several factors, such as the line width of the core-hole lifetime, the monochromaticity of the X-ray source and the energy resolution of the detector influence the FWHM. The latter two contributions will be discussed below. The core-hole lifetime contribution to the FWHM arises from Heisenberg's uncertainty principle, Equation 4.

$$\Delta E \Delta \tau \leq \hbar/2$$

Equation 4

Where ΔE is the FWHM, $\Delta \tau$ is the core-hole lifetime, and $\hbar$ is the reduced Planck constant. Several published sources tabulate the natural line widths based on X-ray emission spectroscopy, Auger electron spectroscopy, and calculations.[73,74] The FWHM of a peak can change depending on the chemical environment around the atom from which the photoelectron is emitted. For example, as mentioned above, in solids the intrinsic photoelectrons can couple with phonons, broadening the photoemission peak and giving the peak a Gaussian characteristic. Metal oxides and carbonates have extensive optical phonons, resulting in multiple solid-state vibrational modes. This results in the FWHM being sharper and more Lorentzian in nature for metals than for oxides and carbonates.[71]

2.3.5 Spin-Orbit Coupling

Core levels in XPS follow the nl_j nomenclature, where n is the principal quantum number, l is the angular momentum quantum number ($l = 0, 1, 2, or 3$ corresponding to s, p, d, or f), and j is the total angular momentum defined as $j =|l + s|$ where s is the spin angular momentum s $= \pm 1/2$. Due to j-j coupling or spin-orbit coupling, all orbitals except the s (where $l = 0$ and, therefore, $j = 1/2$) levels give rise to a doublet with the two possible states having different binding energies. The peaks from this splitting have specific area ratios based on the degeneracy of each spin state, i.e., the number of different spin combinations that can give rise to the total j. The area ratios are summarised in the table below.

Orbital	$j = \lvert l \pm s \rvert$	Area ratio
s	$1/2$	-
p	$1/2 , 3/2$	1 : 2
d	$3/2 , 5/2$	2 : 3
f	$5/2 , 7/2$	3 : 4

Table 2.3. The table lists the angular momentum quantum number, l, with the total angular momentum quantum, j, and the area ratio observed in XPS.

2.3.6 Auger Peaks

As the photoelectron is created, the atom is left in an excited state with a core hole. The excited atom must decay to a ground state done radiatively or non-radiatively. In radiative decay, an electron from a higher energy level fills the core hole (Figure 2.3.3 a). The transition of this electron produces a fluorescent X-ray. In non-radiative decay, a higher energy level fills the core hole, but the energy produced in this transition is transferred to another core-level electron. This electron is then emitted from the atom as an Auger electron (Figure 2.3.3 b).
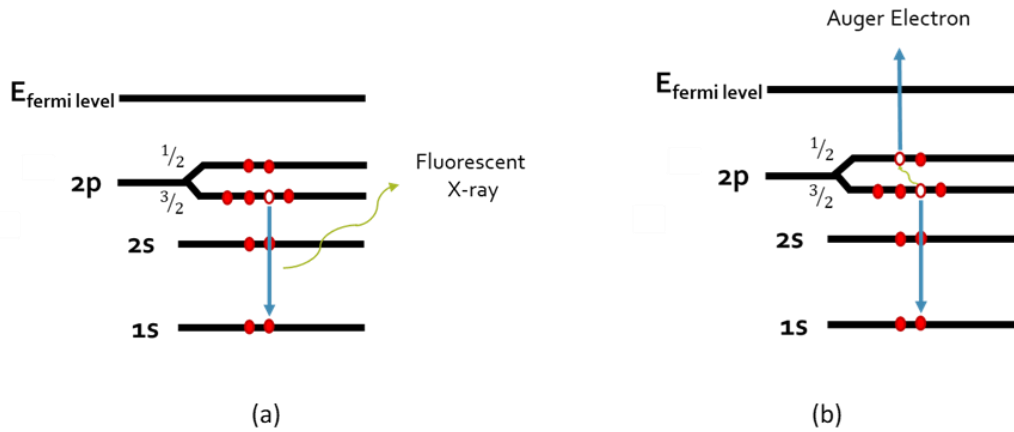
Figure 2.3.3 Radiative decay of an excited atom producing fluorescent X-rays (a) and the non-radiative decay of an atom producing an Auger electron (b).

For an Auger transition *(C, C', C'')*, we can follow energy conservation to arrive at an expression for its kinetic energy:

$$E_K(C,C',C'') = E_b(C) - E_b(C') - E_b(C'') – U(C',C''; s)$$

Equation 5

In this expression, $E_K(C, C', C'')$ is the kinetic energy of the emitted Auger electron, and $U(C', C''; s)$ is the spin-dependent hole-hole repulsion energy between the two holes in the Auger final state. Assuming that the polarization energy is proportional to the square of the charge (i.e., $R^{ea}\{2 \text{ holes}\} = 4 R^{ea}\{1 \text{ hole}\}$) - $U(C', C''; s)$ can be simplified.[70]

$$U(C',C''; s) = \text{const'} -2 R^{ea}$$

Equation 6

Further evaluation of our expression for the kinetic energy of Auger electrons, it can be quickly realized that the first two terms correspond to the energy of the fluorescent X-ray, which is a constant. Equation 6 may therefore be further simplified to Equation 7.

29

$$E_K(C,C',C'') = const'' - E_b(C'') + 2\ R^{ea}$$

2.3.7 Auger Parameter

The Auger parameter is the sum of the binding energy of the photoelectric peak and the kinetic energy of the Auger peak. Using our previous expressions for the photoelectric peak's binding and the kinetic energy of the Auger peak, an expression for the Auger parameter can be written (Equation 7).

$$\alpha' = E_b(C) + E_K(C,C',C'') = const + 2\ R^{ea}$$

It is evident here that the Auger parameter only depends on the extra-atomic relaxation energy.[70] An Auger parameter is a powerful tool in XPS that allows for chemical assignment. Practically, when calibrating the binding energy scale XPS, as the binding energy shifts higher, the kinetic energy of the Auger energy lowers by the same amount, and vice versa. As a result, the Auger parameter remains invariant of the binding energy scale calibration.[76] For example, the literature for BE and Auger kinetic energy positions for Cu_2O have been collected and compared to an independently measured a Cu_2O standard.[76] The BE and Auger kinetic energy positions were found to vary significantly across different studies in the literature values, while the Auger parameter remained invariant.

The Auger parameter is particularly useful when assigning Cu(I) environments, as the BE has a narrow range while the Auger peak varies over a wide range of kinetic energies. This is obvious when the BE and Auger peak kinetic energies are plotted against each other on what is known as a Wagner plot, as shown in Figure 2.3.4.
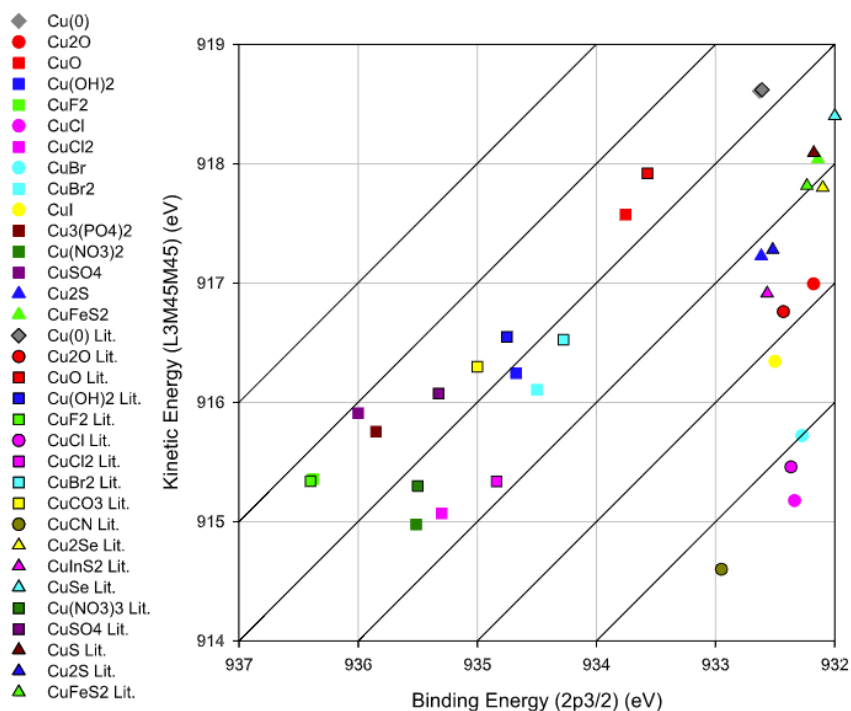
Figure 2.3.4 Wagner plot of Cu standards. From ref([75]).

2.3.8 Peak Fitting

In many spectroscopic techniques, curve fitting or peak fitting is used to extract information from spectral data. The curve fitting method depends on the technique for which it is used. However, generally, the curve-fitted spectra have overlapping peaks. For over 50 years, peak fitting methods have routinely extracted chemical information from overlapping XPS spectra.[71]

In core-level spectra, it is often the case that peaks overlap as a result of the atoms of an element being in different chemical environments. The aim of curve-fitting core-level spectra is to distinguish individual photoemission signals originating from distinct elemental or chemical states. Peak fitting core-level spectra extract parameters such as the BE, FWHM, line shapes, and area. The BE provides evidence for its chemical or elemental nature, while the FWHM and line shape indicate the chemical and physical environment of the atom. While the area is proportional to the quantity of the species present. Quantitative information about the

31

concentrations of each chemical environment can be obtained by measuring the area of each component peak for which the determination of a background signal is essential.

Peak fitting in XPS starts by establishing a background. The choice of the background type and the start and end point selection significantly impact the area under the curve and, consequently, the quantitative analysis. Generally, a simple linear background between the start and end points is incorrect and will lead to errors in the peak fitting of spectra where the measured background is not flat. A Shirley background is mostly used in the peak fitting for this work. The start and end points are chosen such that the background runs through the noise of the data before and after the peak.[71]

Peak fitting takes a series of components to form an envelope, simulating the experimentally measured photoemission spectra. Using an algorithm to minimize a figure-of-merit (such as the standard deviation of the residual) as a quantitative measure of how well the envelope matches the experimental data.[71] The algorithm used to fit the data incrementally adjusts parameters that transition from a current state to a termination state that represents a local minimum with respect to the figure of merit. The fitting algorithm requires an initial guess to produce a fit. The quality of the fit can vary depending on the initial guess – thus, it is vital to choose an appropriate guess based on the physics and chemistry of the systems under investigation. A mathematically excellent fit can result from poor initial guesses which are not physically or chemically appropriate. In theory, fitting the data with many components would give an excellent fit but is often inappropriate as it would suggest many chemical states are present with very small FWHM.

In software such as CasaXPS, the basic optimization algorithm fits peaks to data without considering any constraints that arise from the known physics or chemistry associated with the sample.[76] However, physical and chemical constraints can be manually added to the peak model by selecting area ratios (from spin-orbit coupling), line shapes, FWHM range, etc. Which forces known physical relationships between otherwise independent parameters. Using relationships based on scientific principles increases the likelihood of producing a physically and chemically reasonable fit.

As previously discussed, line shapes typically take the form of a Voigt function. Sums or products of Gaussian and Lorentzian peaks are different from the Voigt function but are often used for peak fitting. In CasaXPS, a Gaussian–Lorentzian product, with a 70% Gaussian and 30% Lorentzian mix (GL(30) within the software), is often used to fit peaks, and this has worked for most samples examined in this study.[71,76] For Cu, the line shape changes between compounds, especially with cupric compounds, which makes peak fitting the Cu 2p challenging, especially with the strong satellite feature on Cu(II) compounds. For the most part, Cu(I) compounds can be fitted using a Gaussian-Lorentzian product with a high Lorentzian component. An interesting approach to fitting the Cu 2p peak is uses multiple Gaussian-Lorentzian peaks with well-defined relative peak positions and FWHMs to create a new line shape obtained from reference spectra to investigate hybrid systems.[75] Using this approach, it was demonstrated that the relative abundance of each component in a mixed system can be obtained.

2.3.9   Surface Sensitivity

Soft X-rays used in XPS penetrate the sample in the order of a few microns. However, the information obtained from XPS is sensitive to 1-10 nm from the surface.[77] The surface sensitivity of the XPS arises due to the electrons from deep in the samples being unable to escape to the surface without inelastically scattering with atoms in the material (Figure 2.3.5). Only photoelectrons that escape the surface without inelastic scattering contribute to the photoemission peak. Therefore, it can be deduced from Figure 2.3.5 that as d → 0, more photoelectrons would escape the surface without inelastic scattering.
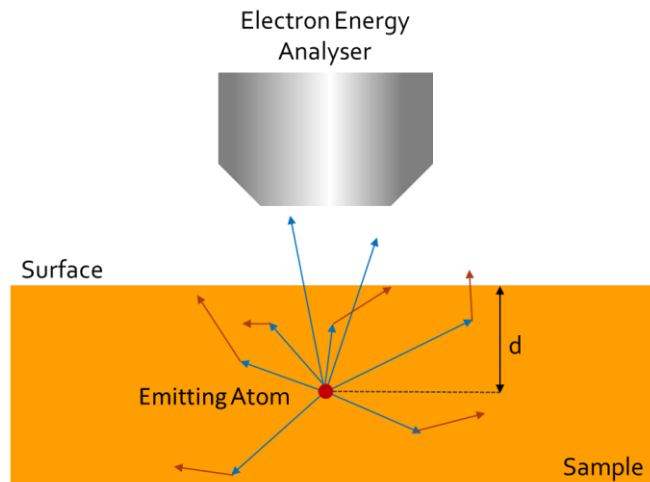
Figure 2.3.5 Diagram depicting photoelectron trajectories emanating from an atom a distance, d below the surface. The blue arrows show the trajectories of the photoelectrons prior to inelastic scattering. The red arrows are the trajectories subsequent to inelastic scattering.

The inelastic mean free path (IMFP) is defined by Technical Committee 201 of the International Organization of Standardization (ISO) as the "average distance that an electron with a given energy travels between successive inelastic collisions."[78] The IMFP is dependent on the initial kinetic energy of the electron. The universal curve was established by Seah and Dench in 1979, which complies with the IMFP of electrons in solids in the range of 1 - 10,000 eV (Figure 2.3.6).[77]
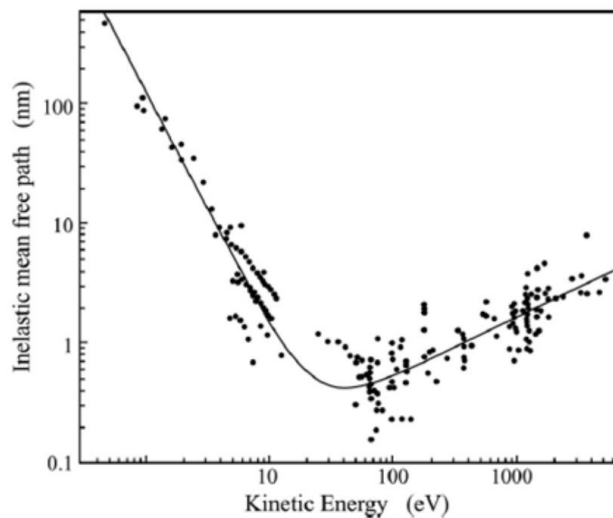
Figure 2.3.6 "Universal curve" of electron inelastic mean free paths in condensed matter as a function of their kinetic energy.[77]

2.3.10 X-ray Photoelectron Spectrometer
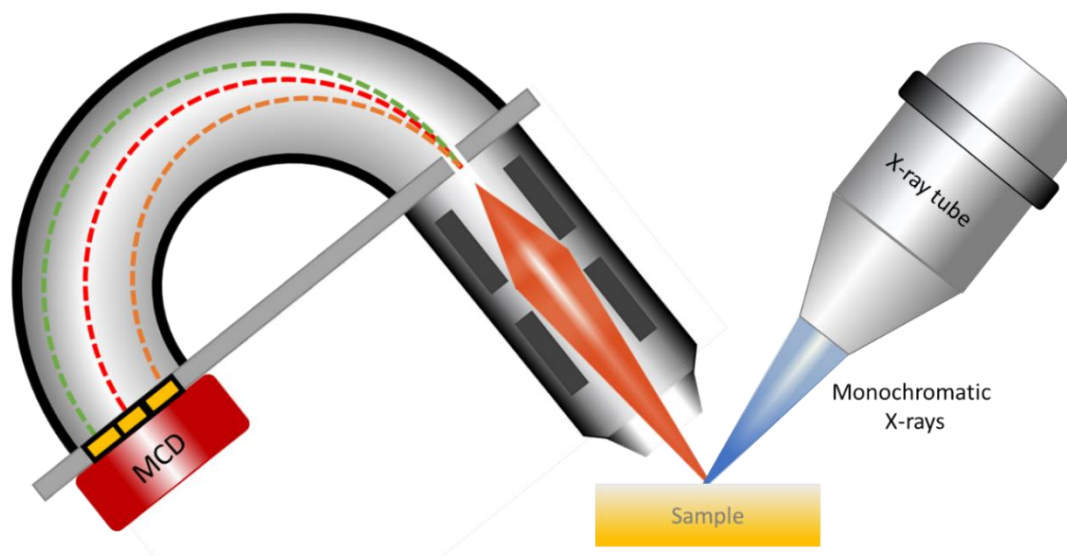
Figure 2.3.7 Schematic diagram of an XP spectrometer.

2.3.10.1 X-ray source

A lab-based spectrometer uses an X-ray tube to produce X-rays. A current is passed through a filament (usually a tungsten filament), releasing thermionic electrons. A high potential difference towards an anode then accelerates the electrons. The X-rays produced have a broad energy spectrum with sharp, intense fluorescent peaks as electrons decelerate in the anode, a continuous spectrum of X-ray energies known as the bremsstrahlung spectra. The thermionic electrons may also excite the electron in the anode to higher energy levels which, when deexcites, produces fluorescent X-rays. Again, the fluorescent X-rays have a sharp, intense peak.

The choice of anode material for XPS determines the fluorescent lines available. The criteria for choosing the anode is an energy high enough to produce an intense photoelectron peak for all elements across the periodic table, with a sharp natural line width such that it does not excessively broaden the resultant spectra.[79] For example, Al K_α and Mg K_α are popular anodes for XPS with photon energies of 1486.6 eV and 1253.6 eV, respectively. This is usually supplied in a single X-ray gun with a twin anode configuration. There are, however, advantages with higher energy sources, (i) It increases the available photoelectron transitions.

35

For example, the Ti K_α can probe into the Ca 1s electron, (ii) increasing the photon energy increases the kinetic energy of the photoelectrons, increasing the IMFP, which probes deeper into the sample.

Element	Line	Energy (eV)	FWHM (eV)
Y	M_ζ	132.3	0.47
Zr	M_ζ	151.4	0.77
Mg	$K_{\alpha1,2}$	1253.6	0.7
Al	$K_{\alpha1,2}$	1486.6	0.9
Si	$K_{\alpha1,2}$	1739.6	1.0
Zr	L_α	2042.4	1.7
Ag	L_α	2984.4	2.6
Ti	K_α	4510.9	2.0
Cr	K_α	5417.0	2.1

Table 2.3.1 X-ray tube sources for XPS from ref([79])
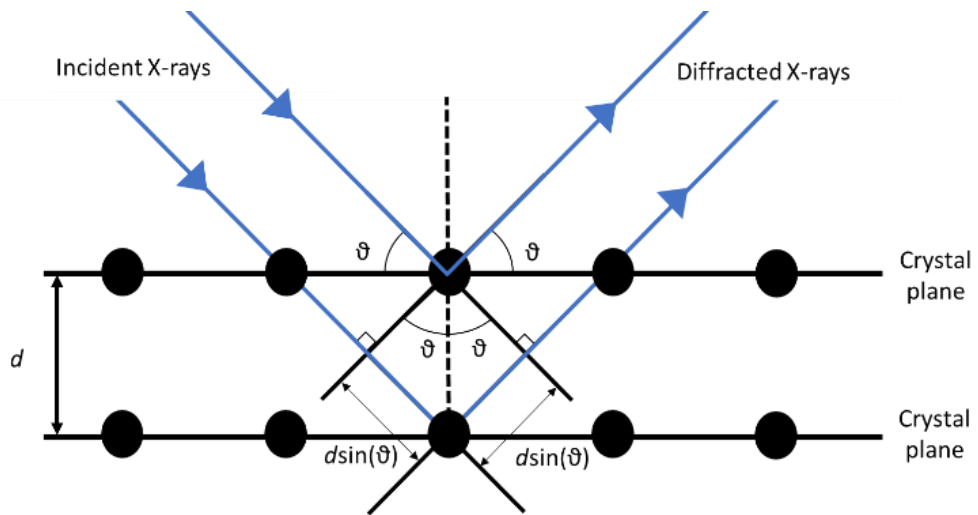
Figure 2.3.8 Diagram showing the geometry of X-rays diffracting crystal lattice planes.

Before the X-rays are incident to the sample, the X-rays produced by the anode pass through a monochromator. The monochromator uses a crystal lattice to diffract X-rays (Figure 2.3.8). X-rays are incident to the crystal, with crystal plane spacing d, at an angle, ϑ, and are reflected by the same angle. When the path length difference, $2d\sin(\vartheta)$ between the reflected beams is a multiple, n, of the wavelength of the X-rays, λ, the reflected beams constructively interfere. From this principle, we can arrive at the Bragg equation.

$$n\lambda = 2d\sin(\vartheta)$$

Equation 9

Quartz ($10\overline{1}0$) is generally used with modern spectrometers, as the angles for diffracting Al K_α photons are convenient.[79] However, other crystal materials for monochromators have been used. In addition to the convenient diffraction angle for Al K_α, the popular choice of quartz arises also from its UHV compatibility, chemical inertness, and that it can be bent to the correct shape to focus the diffracted beam.
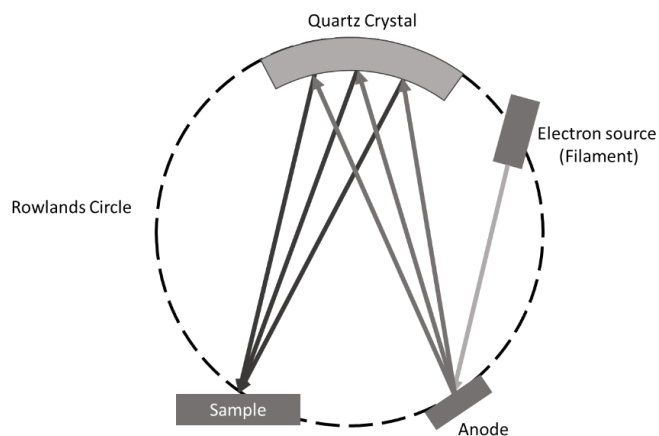
Figure 2.3.9 Rowlands circle shows how X-ray monochrome focused on the sample.

An example of an Ag 3p emission line obtained with and without a monochromator (Figure 2.3.10) shows (i) a considerably higher background, (ii) larger FWHM, and (iii) the presence of features due to X-ray satellites from the non-monochromated X-rays source.
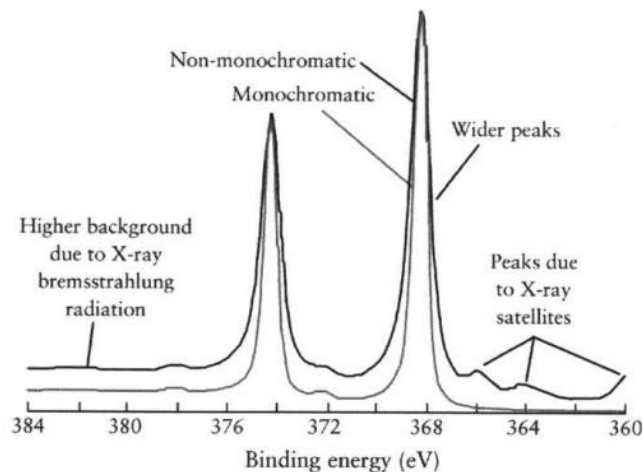
Figure 2.3.10 Ag 3d photoemission peak with and without a monochrome X-ray source.[79]

2.3.10.2 Electrostatic Kinetic Energy Analyser

The photoelectrons go through an electrostatic lensing system (Figure 2.3.11). The kinetic energy of the electrons is often too high for the hemisphere voltages to produce high-resolution spectra. The electrons are, therefore retarded to a defined energy and the hemisphere potentials

are left constant. This defined energy is the kinetic energy window the electrons have available to pass through the hemispherical analyzer - the pass energy.
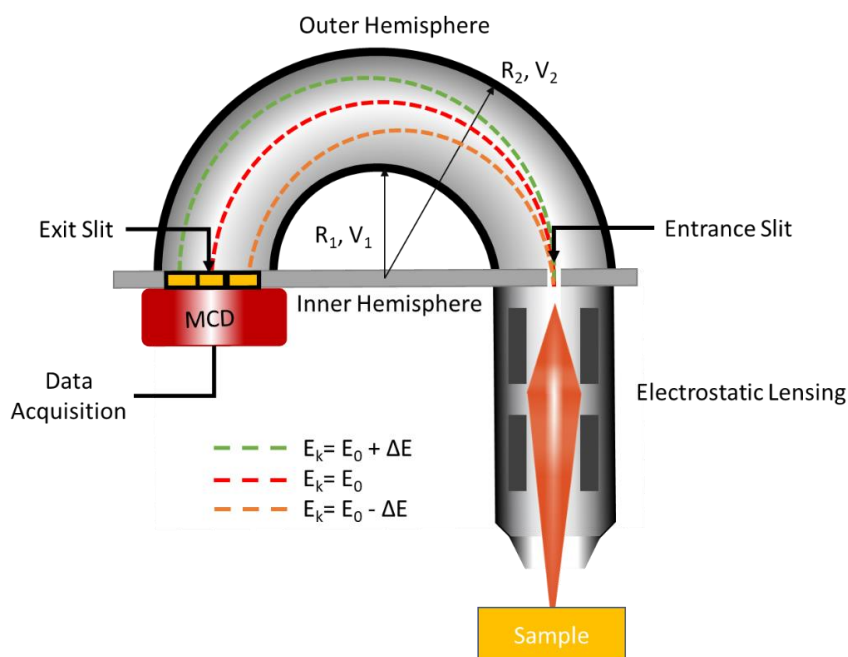
Figure 2.3.11 Schematic diagram of a concentric hemisphere analyzer (CHA) shows electrons' trajectory with varying kinetic energy.

The pass energy affects the resolution and the signal-to-noise ratio of the photoelectrons. Lower pass energy increases the resolution, producing shaper photoemission peaks, while the transmission of the electrons is reduced with low counts. However, with a high pass energy, the transmission is high with intense peaks with lower resolution producing peaks with larger FWHM. The pass energy remains constant throughout the energy range; thus, the resolution is constant across the full range of the spectrum. When measuring the user, select a high pass energy to measure the survey scan and a smaller pass energy to a high-resolution core-level spectrum. This is because the survey scans are usually used for quantification and do not require high resolution, while the high-resolution core-level spectrums are fitted to obtain chemical shifts requiring high resolution.

Concentric hemisphere analyzer (CHA), also referred to as hemisphere sector analyzer (HSA) or spherical sector analyzer (SSA), are two charge concentric hemispherical electrodes with a gap in-between for the electron trajectories to pass (Figure 2.3.11). The charge of the outer hemisphere, V_2, is negative relative to the inner hemisphere, V_1, i.e., $V_2 < V_1$ and the potential difference between the hemispheres is $\Delta V = V_2 - V_1$. After the electron's energy is reduced and passed through the lens system, the electrons are inserted into the CHA through an entrance slit. The photoelectrons take a radial trajectory equal to the mean radius only if the photoelectron meets the following criteria:

$$E = e\Delta V \left(\frac{R_1 R_2}{R_1^2 - R_2^2} \right)$$

Equation 10

Where e is the charge of an electron, E is the kinetic energy of the electrons, and R_1 and R_2 are the radius of the inner and out hemispheres, respectively, as in Figure 2.3.11. This can be simplified as R_1 and R_2 are constant for a given analyzer.

$$E = e\Delta V k$$

Equation 11

k is known as the analyzer constant. The CHA also acts as a lens, so electrons not entering the analyzer tangential to the mean radius may still pass through. Photoelectrons with greater energy than E will take a larger radial trajectory, and photoelectrons with energy smaller than E will have a smaller radial trajectory (Figure 2.3.11). The photoelectrons' energy that does not differ greatly from E also reaches the output plane. Though the energy of the

photoelectrons that reach the output plane varies across that plane, the spectrometer's sensitivity can be increased by binning the signals to separate channels. Multi-channel detectors (MCD) are commercially available. For some instruments, up to 112 channels. However, each channel's width is very small and does not imply that the sensitivity is 112 times greater.

The most common ways to operate a CHA are fixed analyzer transmission (FAT) or constant retard ratio (CRR). Operating in FAT is simple and is how all the data in successive chapters are obtained. However, measuring under FAT V_1 and V_2 vary linearly, as shown in Figure 2.3.12.
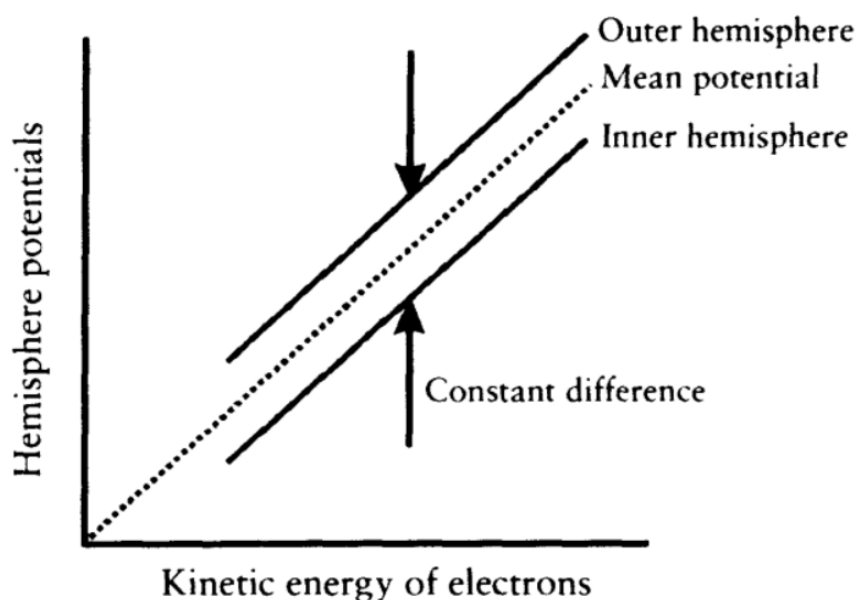
Figure 2.3.12 Inner and Outer hemisphere potential as a fuction of kinetic energy of electrons measured. From ref [79]

2.3.10.3 Charge Compensation

As the photoelectrons are emitted from the surface of a sample, if the sample is insulating, there is a deficiency in electrons, causing a positive surface charge. This results in the photoemission peak shifting to higher binding energy as the surface charge retards the photoelectrons and a deformed photoemission peak. To neutralize the positive charge, a charge

compensator is required to counter this effect, such as flood guns that board the sample with low-energy electrons. The flood gun provides the sample with low-energy electrons in the 1 - 5 eV range, much less than the kinetic energy of any photoelectrons. In addition, the flood gun should deliver a uniform electron distribution across the analysis area to prevent the broadening of the photoemission peaks.

Further, the electrons (current) supplied by the flood gun must be sufficient to neutralize the charge effect. However, the photoemission peaks are still expected to be calibrated to the correct position during data processing. The technique minimizes differential or non-uniform charging.

2.3.11 Depth Profiling by Argon Sputtering

XPS is surface sensitive and does not produce chemical information below ~10nm. A method of investigating beyond 10 nm below is erosion with noble gas ions. Bombarding the surface with Ar^+. Figure 2.3.13 shows the experimental procedure followed to obtain a depth profile. The sample is initialized by measuring the surface with XPS. The samples then undergo sputtering, where Ar^+ ions are accelerated to energies in the order of a few hundred to a few thousand eV for some time interval. The sample is measured again, and the process is repeated. This process is repeated until the depth is desired reached.
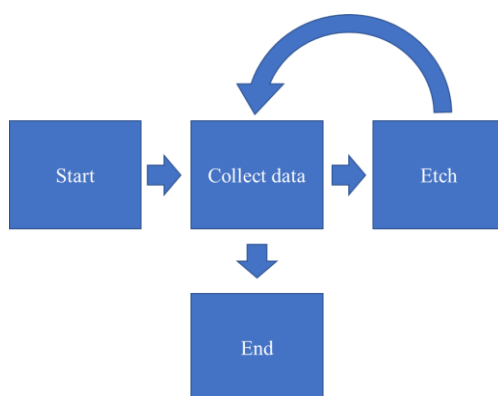
Figure 2.3.13 Flow diagram of the experimental proceedure for depth profiing with XPS.

2.4   X-ray Absorption Spectroscopy (XAS)

The theory of X-ray absorption spectroscopy (XAS) and its potential to be used as an analytical technique has been well-established since the 1920s.[80,81] However, since the technique requires a large spectrum of X-ray energies and high flux, it was not readily used until the 1970s, when synchrotron radiation became more available.[82–84] XAS is an element-specific technique that provides chemical and structural information from the absorbing atom, such as oxidation and coordination number of up to 5 Å.[85,86]

X-ray photons in the energy range of 500 eV to 500 keV are attenuated by matter due to the photoelectric effect. This process involves a tightly bound core electron absorbing the ejected photon into the continuum. This assumes the binding energy of the core electron is less than the incident photon's energy. This simple principle is used to study the local structure of the matter.

The absorption coefficient, $\mu(E)$, can describe the absorption of X-rays. This describes the linear attenuation of the X-rays through a sample in accordance with Beer's Law:

$$I = I_o e^{-\mu(E)x}$$

Equation 12

Where I_0 is the intensity of the incident X-ray beam, I is the transmitted X-ray, and x is the distance of the path taken through the material (Figure 2.4.1).
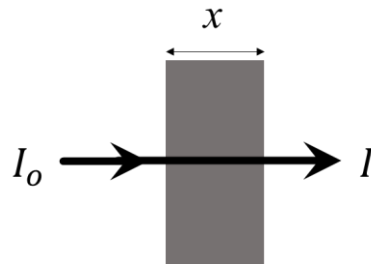
Figure 2.4.1 Incident monochromatic X-rays beam of intensity I_0 passes through a sample of thickness x, resulting in a transmitted beam with intensity I. The absorption coefficient μ is given by the Beer-Lambert law (Equation 12).

For the energy range of the X-rays, the $\mu(E)$ is a smooth function and can be approximated by:

$$\mu \approx \frac{\rho Z^4}{A E^3}$$

Equation 13

Where ρ is the density of the material, Z is the atomic number, A is the atomic mass number, and E is the energy of the incident X-ray.
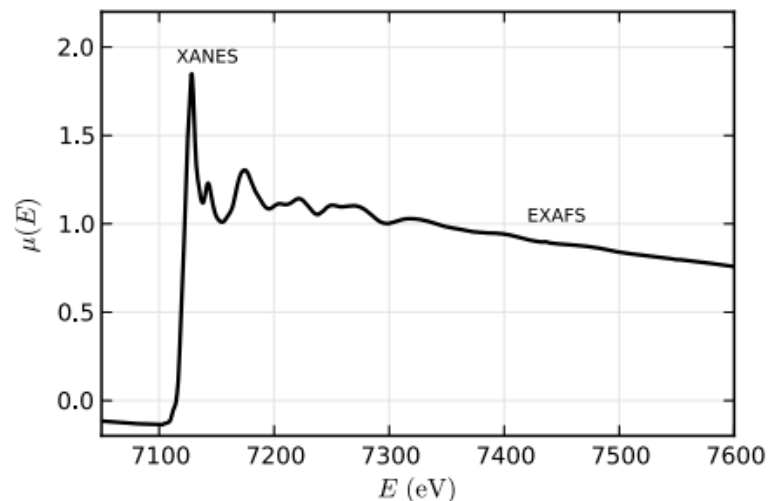
Figure 2.4.2 A plot of a normalized absorption coefficient spectrum of FeO labelling the regions of XANES and EXAFS. The oscillations after the edges are known as XAFS.[80]

When the binding energy is equal to the energy of the incident photons, there is a sharp rise in the absorption coefficient – called the absorption edge (Figure 2.4.2). X-ray Absorption Near

44

Edge Spectroscopy (XANES) and X-ray Absorption Fine Structure (XAFS) can be observed through the absorption coefficient spectrum as a function of energy. All atoms have well-defined quantum states and, therefore, well-defined binding energies. The edge of an element can be investigated by tuning the energy of the incident X-rays.

2.4.1 XAS Measurements

2.4.1.1 Transmission

The accurate measurement of the absorption coefficient, $\mu(E)$, is crucial. The interpretation of a noisy spectrum could lead to misleading information, so it is imperative to repeat measurements to obtain good statistics. As Figure 2.4.3 demonstrates the basic experimental set-up for transmission XAS, the difficulty in the experiment is obtaining tuneable X-ray sources along with high-quality detectors which can handle the high X-ray flux. Bremsstrahlung radiation is used in a synchrotron, as it has an extensive continuum of wavelengths in the X-ray region, which is monochromated by a silicon crystal via Bragg diffraction. The crucial aspects of the monochromator to consider are its energy resolution, reproducibility and stability. Energy resolutions of ~1 eV at 10 keV could easily be achieved by silicon and is sufficient for XAS.[80] Simple ion chambers are often used to measure the intensity of the X-ray beam incidence on the sample and transmission through the samples.
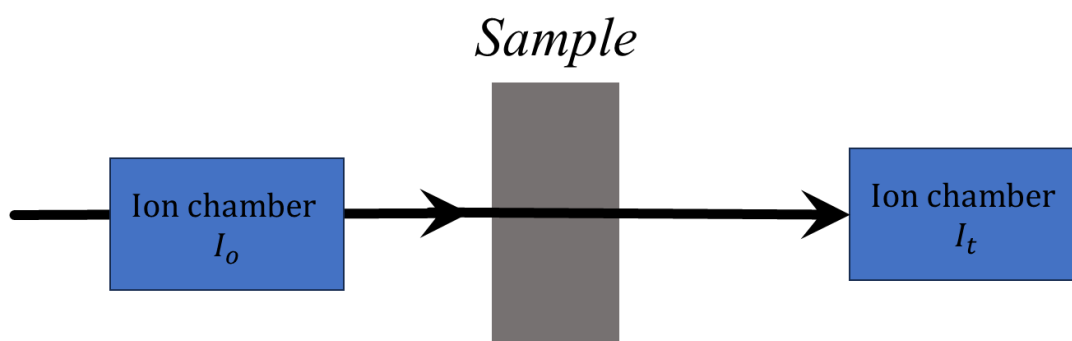
Figure 2.4.3 Experimental set up for a XAS measurement via transmission. Monochromatic X-rays are passed through an ion chamber that measures the I_0, then passes through the sample and finally measured by another ion chamber to measure the transmitted X-rays I_t.

Concentrated samples should be measured in transmission mode. For transmission mode, there is required to be enough transmission through the sample to obtain a decent signal for I_t. It is desirable that the thickness, $\mu t \approx 2.5$, above the edge. For iron, t =7 μm, whist for many other metal oxides, t is often an order of magnitude larger.[80] In the dilute case, the sample thickness could be in the order of millimetres.

Furthermore, obtaining a homogenous sample free from pin holes is highly desirable. For powders, this may become more difficult as it is also required that the grain sizes are not larger than an absorption length. Measurements using the transmission method is appropriate with samples with a concentration greater than 10 %.

2.4.1.2   *Fluorescence Yield (FY)*

For thick and lower concentration samples, fluorescence yield is often the detection mode of choice for recording XAS. In this mode of XAS measurement, the X-rays that emanate from the sample include the emission line of interest, fluorescent lines from other elements within the sample, and both elastic and inelastically scattered X-rays. Usually, the prominent X-rays in the fluorescence spectra are the fluorescence lines and the elastically scattered X-rays. The two criteria for obtaining good fluorescence spectra are the solid angle and the energy resolution.[80,87]

Since fluorescent emission is isotropic, obtaining as much of the signal as possible is desirable. Scattering X-rays, however, are not isotropic due to the polarized (in the plane with the synchrotron) nature of the synchrotron source.[80,87] Due to this fact, the scattered X-rays normal to the incident beam are heavily suppressed. Energy discriminating detectors are an important component for the set-up as they allow suppression of scatter peaks and insignificant fluorescent lines, consequentially increasing the signal-to-noise ratio.

Energy discrimination can be done physically or analytically, which is to say, actively filtering out unwanted emissions before or electronically after detecting the photons. A popular method of achieving energy discrimination is using silicon or germanium-based solid-state detectors. Such detects are able to achieve resolutions of ~200 eV or greater. Due to large portions of the

spectra being neglected, these detectors can be used for samples with concentrations as low as ppm levels. These detectors have great advantages though there are some disadvantages, such as dead time and its complicated nature. Dead time arises due to the finite time required to process the signal. Typically, detectors are limited to a total count rate of ~105 Hz. [80] If this is exceeded, the detector is unable to count more and is deemed 'dead' for a fraction of the time. Maintaining and setting up such detectors can also cause complications compared to ion chambers. The detector's temperature, for example, must be kept in the liquid nitrogen range.[80]

A limitation of fluorescent measurements s in XAS is self-absorption for optically dense (concentrated) samples. Fluorescent photons have to travel back through the samples before reaching the detector. The fluorescent photons are attenuated and consequently the damping post-edge features. When the sample is at 45° to both the incident beam and the detector, the measured fluoresce intensity is given by the following:[80]

$$I_f = I_o \frac{\varepsilon \Delta \Omega}{4\pi} \frac{\mu_\chi(E)}{\mu_{tot}(E) + \mu_{tot}(E_f)} \left[1 - e^{-(\mu_{tot}+\mu_{tot}(E_f))t} \right]$$

Equation 14

Where ε is the fluorescent efficiency, $\Delta\Omega$ is the solid angle of the detector, E_f is the energy of the florescent X-ray, $\mu_\chi(E)$ is the absorption of the atom of interest, and lastly, the $\mu_{tot}(E)$ the total absorption of the sample at energy E. For very concentrated samples $\mu_{tot}(E) \approx \mu_\chi(E)$, it would be expected that the post-edge oscillations are lost. For highly concentrated samples, it should be preferred that transmission measurement be performed.

2.4.2   XANES

XANES is typically considered to be the energy range within 30 eV above an X-ray absorption edge.[80] The XANES section of the spectrum provides information such as the absorbing atom's oxidation state and coordination environment. Other spectral features, such as the energy and intensity of observed peaks, can be used to identify chemical and physical configurations qualitatively.[80,88]

The region prior to the absorption edge, the pre-edge, contains weak features as core level electrons to empty bound states (bound state transition).[88] Dipolar selection rules control the bound state transition probability. Pre-edge features are observed in first-row transition metals as their 3d orbital are not fully occupied. However, 1s $\rightarrow$ 3d transitions are not usually permitted by the dipole selection rule, as the first-row transition metals have 3d to 4s orbital mixing and direct quadrupolar coupling.[80,88]

The position of the edge increases as the oxidation state increases. This can be explained using a simple electrostatic model [88]As the oxidation state increases, the nucleus becomes less shielded and, therefore, more tightly bound to core electrons, requiring greater energy photons to excite.

The energy position and intensity of the observed peaks can be used to qualitatively identify chemical and physical configurations.[89] However, while a qualitative analysis can be done, a direct quantitative analysis from first principles is difficult. As a result, analysis of XANES is typically done by linear combination fitting (LCF) of known compounds.[89]

3   Aims and Objectives

The mechanism of non-aqueous Cu corrosion by lubricant additives is not widely understood. The research presented in this thesis aimed to investigate the mechanism of non-aqueous Cu corrosion by lubricant additives using X-ray spectroscopies. The secondary aim is to develop new methods to characterise tribological samples *in situ* or in *operando*.

To achieve these aims, the following objectives are outlined:

- Conduct comprehensive experimental investigations to gain an understanding of the mechanisms responsible for Cu corrosion within lubricant additive systems, with a specific focus on the corrosive actions of ZDDP and MoDTC. Controlled corrosive conditions can be done using the HTCBT method (or similar experimental approaches). Exploration of the individual contributions of ZDDP and MoDTC to corrosion through mono-blend lubricants.

- A parallel objective to the one above is to explore synergistic interactions of MoDTC and ZDDP to the corrosion of Cu in lubricant systems with polyblend lubricants.

- Identify chemical species formed on the samples during Cu corrosion in the presence of additives using analytical characterization techniques such as XPS and XAS.

- Develop innovative methods tailored to address the challenges involved in studying Cu corrosion within lubricant additive systems through in situ and operando characterization of tribological samples.

4 Combined XPS and XAS Studies of Copper Corrosion by Non-Aqueous Molybdenum Dithiocarbamate Solutions

4.1 Abstract

Copper (Cu) based alloys have become a popular choice to replace lead (Pb) alloys in combustion engine bearings, as Pb is being phased out due to growing concerns about its environmental impact. Molybdenum dithiocarbamate (MoDTC) is a popular friction-modifying additive used in lubricants. The chemistry of MoDTC on steel surfaces has been well studied using various characterization techniques, but little work has been done to understand its interaction with Cu. As MoDTC contains a large amount of sulphur (S), Cu is susceptible to corrosion by released sulphur compounds, which has a detrimental effect on engine lifetime. The interaction between MoDTC and Cu surfaces was investigated under the conditions of the high temperature corrosion bench test (HTCBT). X-ray photoelectron spectroscopy (XPS) and X-ray absorption spectroscopy (XAS) characterization shows the initial formation of a Cu_2O layer during the HTCBT, followed by the formation of Cu_2S via O^{-2}/S^{-2} ion exchange. The influence of temperature on the Cu/ MoDTC interaction was also investigated by XPS, confirming previous energy-dispersive X-ray (EDX) results and adding a better understanding of the associated interfacial chemistries.

4.2 Introduction

Engine bearings allow load transmission between the crankshaft and piston and convert reciprocating motion to circular motion. The bearings have low friction and resistance to wear and corrosion.[9] Materials with good conformability and resistance to wear require a compromise between hard and soft materials, such as copper (Cu). In addition, Cu has good embeddability when particles become entrained in the oil under boundary conditions.[3] Corrosion of the engine bearing reduces the engine's lifetime and may ultimately lead to engine failure. Lead (Pb) has also been used in bearing in the past but is being phased out by engine manufacturers due to environmental concerns about its contamination into the engine. The corrosion of Cu has consequently become a more critical issue.[14]

Molybdenum-containing additives were introduced in the 50s but were only introduced as friction modifiers in the 70s.[50,52,54,90–92] There have been many Mo-containing additives; however, molybdenum dithiocarbamate (MoDTC) has grown in popularity, showing the best friction reduction performance in modern engines. Friction reduction has been attributed to the formation of MoS_2. Weak intramolecular forces between MoS_2 sheets reduced the friction between sliding surfaces. The formation of MoS_2 has been studied using various characterization techniques[48,60,93–97] High-resolution transmission electron microscopy (HR-TEM) has indicated the presence of flake-like particles with approximately 10 nm diameter and a 1 nm thick MoS_2 structure.[98,99]

The proposed breakdown MoDTC is initiated by cleaving two Mo-S bonds, forming free radicals. Two radicals recombine to form thiuram disulphide, while the other decomposes to Mo_2S and MoO_2.[66] A more recent study of the degradation of MoDTC using high-performance liquid chromatography (HPLC), Fourier-transform infrared spectroscopy (FT-IR), and mass spectroscopy (MS)[57] suggested that non-stoichiometric particles were created (MoS_xO_y).[58] The process is initiated by isomerism and a reaction with oxygen, omitting two sulphur atoms from the structure. The product then decomposed, forming secondary amines CO_2 and MoS_xO_y particles.

Many studies of MoDTC have been done on ferric and ferrous surfaces under tribological conditions. In contrast, little has been done to investigate the fundamental interaction of MoDTCs with Cu surfaces. MoDTC is a popular and effective friction modifier used in lubricant formulations; however, as it contains sulphur (S), Cu is susceptible to corrosion, which is detrimental to the engine's lifetime. The high-temperature corrosion bench test (HTCBT) is an industrial test to screen for lubricant formulations' affinity to corrode soft metals commonly found in automotive diesel combustion engines such as Cu.[7,35] In this study, the molecular interaction of MoDTC on Cu surfaces under HTCBT conditions using XPS and XAS was investigated. In addition, the influence of the temperature on the MoDTC/Cu interaction was also conducted with XPS.

4.3   Experimental Methods

Cu substrates (approximately 1 cm x 1 cm x 0.9 mm coupons, 99.9%) were obtained from Infineum UK Ltd. They were polished using a series of abrasive paper (SiC, P400, and P250 grit) treatments and finished with (SiC, P1200) abrasive powder. The resulting surface was rinsed with cyclohexane, which was immediately mechanically removed from the surface by a stream of compressed air, which also evaporated any excess cyclohexane adhering to the remaining metal surfaces.

The 0.1wt% MoDTC model lubricant formulation was prepared by diluting concentrated MoDTC with DURASYN® 164 polyalphaolefins (group IV base oil, 100 % obtained from Collinda). The diluted solution was then stirred with a magnetic stirrer for a minimum of 2 hours to ensure dissolution into a homogeneous phase.
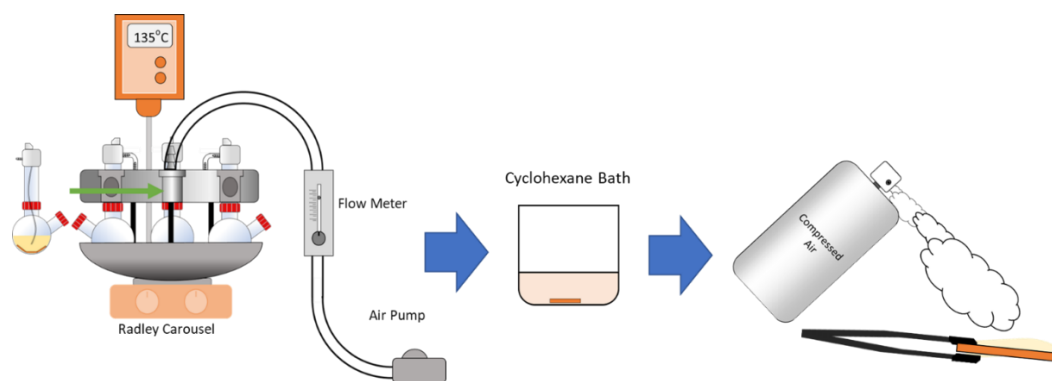
Figure 4.3.1 Schematic flow diagram of the experimental procedure of modified HTCBT.

A modified HTCBT test was performed in round bottom flasks containing Cu coupons and 150 ml lubricant solution. The round bottom flasks were placed on a Radley 6 Plus Reaction Station™ carousel heater platform, which also provides a gas manifold for controlling the gas atmosphere in the round bottom flasks through a continuous flow of the gas. The temperature of the lubricant was maintained at 135°C using a feedback thermocouple placed at the base of the Carousel. A stream of ambient air was bubbled through the solution in each flask using a diaphragm air pump with a rate of 5 dm^3 h^{-1} controlled by a mass flow meter (Figure 4.3.1).

To monitor the progress of corrosion by the lubricant/air treatment, a coupon was periodically removed from each round bottom flask. The coupons were rinsed with cyclohexane to remove excess oil and blown dry with compressed air. The coupons were stored in 10 ml clip-top glass vials until characterisation was performed.

Similar to the method described above, the reaction of Cu with base oil and 0.1 wt% MoDTC was investigated with no airflow through the solution at varying temperatures. As described above, the coupons were submerged in the solution for 10 min before rinsing with cyclohexane.

XP spectra were collected with a Specs FlexMod ultra-high vacuum (UHV) instrument equipped with a monochromatic Al K$_\alpha$ X-ray source (1486.71 eV) that operated with a power of 40 W. The kinetic energy of the photoelectrons was determined with a Phoibos 150

electrostatic hemispherical analyser with 1D delay line detectors, operating in a small-area mode with a source−analyser angle of 55°. The Cu coupons were mounted on standard Omicron sample holders using double-sided carbon adhesive tape. Spectra were collected at ambient temperature at a base pressure of 10^{-9} mbar. Survey spectra were collected as a single scan with a step size of 1 eV, a pass energy of 50 eV and a dwell time of 100 ms. High-resolution core-level spectra were collected with a step size of 0.1 eV, a dwell time of 100 ms per data point, and a pass energy of 30 eV. Under these conditions, the instrument achieves a resolution of approximately 0.7 eV, comparable to the natural line width of the photoemission lines.

The spectra were analysed quantitatively using CasaXPS.[76] The analyser transmission function of the XPS instrument was determined exactly as reported in a recent VAMAS round-robin study, which confirmed the accuracy of the instrument for quantitative analysis.[100] For the elemental analysis, the overall intensities of the strongest emission lines for all elements were determined and corrected using the relative sensitivity factors reported by Scofield 1973.[101] For the chemical state analysis from the high-resolution spectra, Shirley backgrounds and a GL (30) line shape (30% Lorentzian, 70% Gaussian) were used to model all components evident in the emission lines. For Cu $2p_{3/2}$, a Shirley background and a GL (80) line shape (80% Lorentzian, 20% Gaussian) were used for the fit. The C 1s spectra were used for calibration of the electron binding energy (BE) scale. The C 1s emission was modelled using GL (30) lines to identify components from unsubstituted aliphatic carbon and BE-shifted components associated with carbon bounds to electronegative heteroatoms. A second component at ~1.5 eV above the main unsubstituted aliphatic component was fitted with the same full width at half maximum (FWHM). This higher binding energy (BE) component is associated with carbon singly bonded to oxygen from alcohol (C-OH) and/or ether (C-O-C) functional groups. Higher BE components were fitted as appropriate (e.g. for carbonyl carbons, such as C=O, 2.8 -3.0 eV above the main aliphatic peak, and carboxylate/carboxylic acid groups, COO$^-$/COOH, at BEs that are 3.6–4.3 eV above the unsubstituted aliphatic peak). Calibration of the binding energy scale was then carried out by setting the centroid BE of the unsubstituted aliphatic component to 284.8 eV. Spectra were also carefully checked for

evidence of residual charging (especially differential charging) and the possibility that electrically insulating surface layers may be formed, for which the Fermi energy of the substrate may not be a representative reference point. This careful calibration protocol achieves a reproducibility and error of approximately $\pm$ 0.1 - 0.2 eV.[75,102]

In addition to XPS, select samples were also characterized using XAS. The setup for this is discussed in section **Error! Reference source not found.**.

4.4   Results

Three experiments were performed, HTCBT with 0.1 wt% MoDTC and a similar experiment to the HTCBT, which aims to investigate the temperature effect in the absence and presence of the additive. The latter two experiments would aid in understanding the chemical pathway occurring in the HTCBT leading to corrosion.

The presented results are XPS and XANES (collected via TEY) measurements of Cu coupons 1 cm x 1 cm x ~ 0.9 mm undergone HTCBT with MoDTC or Temperature Test with a base oil and MoDTC (outlined in the previous section). XPS and XANES measured by TEY are surface-sensitive techniques that provide chemical information at 1-10 nm and ~300 nm, respectively.[77,103–107]

4.4.1   HTCBT with 0.1 wt% MoDTC

Seven Cu samples were prepared using the HTCBT method (discussed above) with 0.1 wt% MoDTC with base oil. The Cu samples were emersed from the oil at times from 4 – 150 min into the HTCBT. Figure 4.4.1 shows images of the Cu coupon samples mounted on Omnicron sample holders prior to XPS measurements. Comparing their appearance indicates that the Cu surface tarnishing generally increases in severity as a function of time. However, the sample that emerged at 24 min does appear darker than the succeeding 30 min sample. This may be due to a thin tarnish film formed on the surface where birefringence occurs.
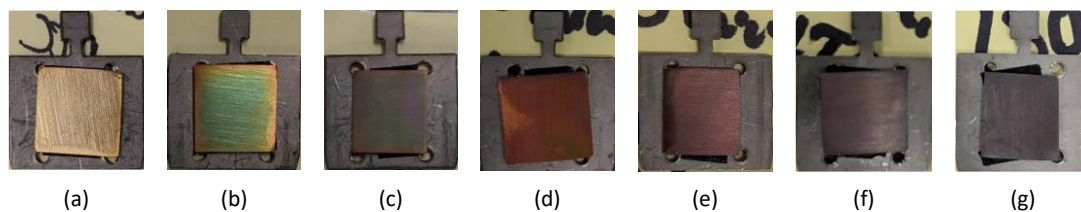
Figure 4.4.1 Images of Cu coupons immersed from HTCBT with 0.1 wt% MoDTC in Base oil after (a) 8 min, (b) 16 min, (c) 24min, (d) 30 min, (e) 90 min, (f) 120 min and (g) 150 min. The samples are mounted on Omnicron sample holders. The images are taken prior to XPS measurements.

HTCBT with 0.1 wt % MoDTC

Reaction Duration (min)	Atomic Percentages (%)				
	O 1s	C 1s	Mo 3d	S 2p	Cu 3s
8	18 ±1	45 ±1	2 ±1	8 ±1	26 ±1
16	18 ±1	52 ±1	2±1	6 ±1	26 ±1
24	21 ±1	49 ±1	2 ±1	7 ±1	20 ±1
30	11 ±1	48 ±1	2 ±1	14 ±1	25 ±1
90	13 ±1	43 ±1	2 ±1	14 ±1	29 ±1
120	8 ±1	44 ±1	2 ±1	16 ±1	31 ±1
150	8 ±1	45 ±1	2 ±1	15 ±1	29 ±1

Table 4.4.1 XPS survey results for elemental composition in atomic percentages for Cu coupons emersed from the oil phase after HTCBT for 8 – 150 min.

Ex situ samples of Cu coupons that underwent HTCBT with 0.1 wt % MoDTC for 8 - 150 min were characterized by XPS. Table 4.4.1 shows the survey results for the elemental composition in atomic percentages, and Figure 4.4.2 shows normalized, high-resolution, core-level spectra of the elements present on the surfaces.

The spectra shown in Figure 4.4.2a have three fitted components with binding energies positioned at 284.8 eV, 286.3 eV, and 288.2 eV (FWHM = 1.3 - 1.4 eV), attributed to C-C or C-H (aliphatic carbon), C-OH and C=O, respectively. The aliphatic carbon photoemission peak was 284.8 eV to calibrate the binding energy scale of the spectra.

Mo 3d spectra after $8 - 24$ min in the HTCBT were fitted with a $3d_{5/2}$ and $3d_{3/2}$ doublet (Figure 4.4.2b). The fitted Mo $3d_{5/2}$ has a binding energy of $231.6 - 231.7$ eV (FWHM = 1.1 -1.4 eV) attributed to MoO_2. After $30 - 150$ min, two sets of $3d_{5/2}$ and $3d_{3/2}$ doublets to the Mo spectra were evident, fitted with two $3d_{5/2}$ and $3d_{3/2}$ doublets corresponding to two Mo species. The positions of the Mo $3d_{5/3}$ are 231.5 - 231.6 eV (FWHM =1.1 -1.2 eV) and $232.4 - 232.6$eV (FWMH =1.7 eV) attributed to MoO_2 and MoO_3 respectively. The substantially different MoO_2:MoO_3 is attributed to the 3

After 8 -24 min HTCBT, the O 1s spectra can be fitted with two components (Figure 4.4.2c) with binding energy positions centred at 530.5- 530.6 eV and 531.4 eV (with FWHM = 1.6-1.7 eV). The peaks at $330.5 - 530.6$ eV are attributed to MoO_2/Cu_2O lattice species. Peaks were found at 531.6 eV, which can be attributed to Cu_2O defective oxide.[75,108] The 30 min O 1s spectra are also fitted with two components with binding energies 530.4 eV (FWHM = 1.5 eV) and 531.9 eV (FWHM = 1.7 eV) attributed to MoO_2 and MoO_3, respectively. After $90 - 150$ min HTCBT O 1s spectra are also fitted with two components with binding energies at 530.1 - 530.4 eV (FWHM = $1.3 - 1.5$) and 531.4-531.5 eV (FWHM = 1.6 - 1.7 eV), attributed to MoO_2 and MoO_3 respectively. Oxygen-containing absorbates are expected to be present on the samples. The binding energies of oxygen-containing absorbates overlap with the binding energies of the fitted peaks.[109,110] It is possible that these absorbates co-exist with the oxides assigned to the peaks.

Figure 4.4.2 Normalized, high-resolution core-level XPS spectra of (a) C 1s, (b) Mo 3d, (c) O 1s, (d) S 2p, (e) Cu 2p and (f) the high-resolution Auger spectra of Cu $L_3M_{4,5}M_{4,5}$ of ex-situ samples emerged from the HTCBT at 8 – 150 min, with 0.1 wt % MoDTC in base oil. The spectrometer has a resolution of 0.7 eV, and the energy calibration procedure introduces a 0.2 eV error to the position quoted to the fitted components.

S $2p_{3/2}$ and $2p_{1/2}$ doublet sets are fitted to the S 2p spectra Figure 4.4.2d. At 8 – 24 min, the fitted $2p_{3/2}$ has a binding energy of 161.9 eV (FWHM =1.2 eV) attributed to sulphides (S^{-2}). Similarly, at 30 – 150 min, the fitted $2p_{3/2}$ has a binding energy of 161.9 – 162.0 eV (FWHM =1.2 - 1.4 eV) are also attributed to sulfides, specifically Cu_2S. The assignment of Cu_2S is confirmed by the obtained XANES spectra (see Figure 4.4.4).

In addition, at 8 - 24 min, smaller, broader doublet peaks are fitted. The fitted $2p_{3/2}$ binding energy is 167.6 - 167.9 eV (FWHM = 2.6 eV), attributed to sulphones. A similar chemical environment is observed for 30 min. When fitted with a $2p_{3/2}$ and $2p_{1/2}$ doublet, the $2p_{3/2}$ binding energy is 168.5 eV (FWHM = 2.6 eV), attributed to sulphates.

At 8 – 24 min, two components are fitted to the Cu $2p_{3/2}$ (Figure 4.4.2e) with binding energies of 932.6 eV (FWHM = 1.4 eV) and 934.9 eV (FWHM = 2.6 eV) attributed to Cu_2O and $Cu(OH)_2$ respectively. Finally, only one component is fitted at 30 - 150 min with a binding energy of 932.5 eV (FWHM= 1.4 eV), attributed to Cu_2S.

A slight but quantifiable shift in the binding energy position of the Cu $L_3M_{4,5}M_{4,5}$ Auger peak is observed (Figure 4.4.2f). At 8-16 min, the position of the Cu $L_3M_{4,5}M_{4,5}$ is 916.7 eV, corresponding to Cu_2O. However, at 30 - 150 min, the Cu $L_3M_{4,5}M_{4,5}$ shifts to 917.2 eV, corresponding to Cu_2S. In addition, there is a distinguishable Cu $L_3M_{4,5}M_{4,5}$ shoulder feature at ~ 920 eV, only observed at 30 - 150 min samples - this feature is characteristic of Cu_2S.

The XANES spectra of five copper standards (Cu metal, Cu_2S, CuS, Cu_2O, and CuO) were measured via transmission. The edge position for Cu metal (Cu^0) is 8979.11 eV. Slightly above the edge, a peak found at 8980.41 eV is attributed to the 1 s $\rightarrow$ 4p transition.[111–113] For Cu_2O, the edge position is 8980.30 eV, a sharp peak above the edge around 8981.64 eV is attributed to the 1 s $\rightarrow$ $4p_{xy}$ transition, followed by a peak around 8995.25 eV attributed to 1s $\rightarrow$ $4p_z$ due to the ligand field effect. In contrast, CuO shows a weak characteristic pre-edge peak caused by the electric quadruple allowed 1s $\rightarrow$ 3d transition at 8977.61 eV, followed by the edge at 8983.3 eV and then by the 1s $\rightarrow$ $4p_{xy}$ peak (8985.60 eV) and the 1s $\rightarrow$ $4p_z$ peak (8997.37 eV).

The $1s \rightarrow 4p_{xy}$ and $1s \rightarrow 4p_z$ transitions for CuO are much higher than those in Cu_2O spectra. [112–114] The edges for Cu_2S and CuS are positioned at 8980.19 eV and 8981.47 eV, respectively (Figure 4.4.3). Cu_2S shows slight shoulder features at 8981.45 eV and 8588.83 eV. In contrast, CuS have shoulder features at 8978.75 eV, 8983.12 eV, and a distinct peak at 8986.03 eV. The features found on the rising edge region (9980 -9000 eV) of Cu_2S and CuS are due to the dipole-allowed $1s \rightarrow 4p$ transition, charge transfer shakedown transitions from Cu-ligand covalent overlap, and long-range multiple scattering transitions. [113,115–117]
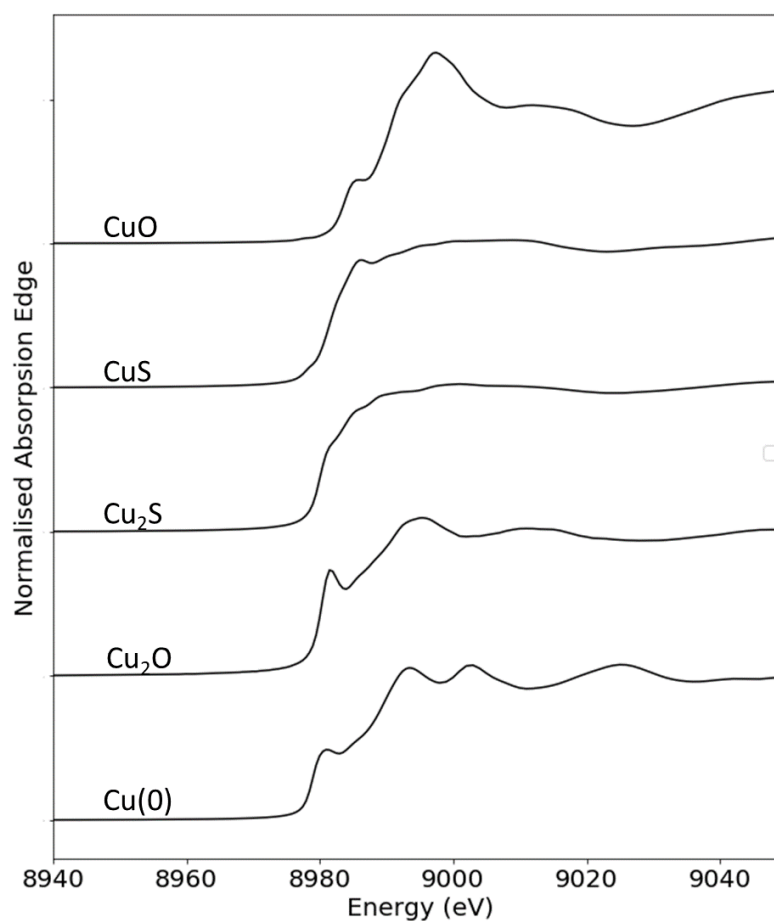
Figure 4.4.3 Normalized Cu K edge, XANES spectra of Cu metal, Cu_2O, Cu_2S, CuS and CuO.

Although a true understanding of all electronic factors affecting the rising-edge energy has yet to be achieved, it has been empirically observed that the energy of the rising-edge shifts to higher energy with an increase in oxidation state. [117,118]
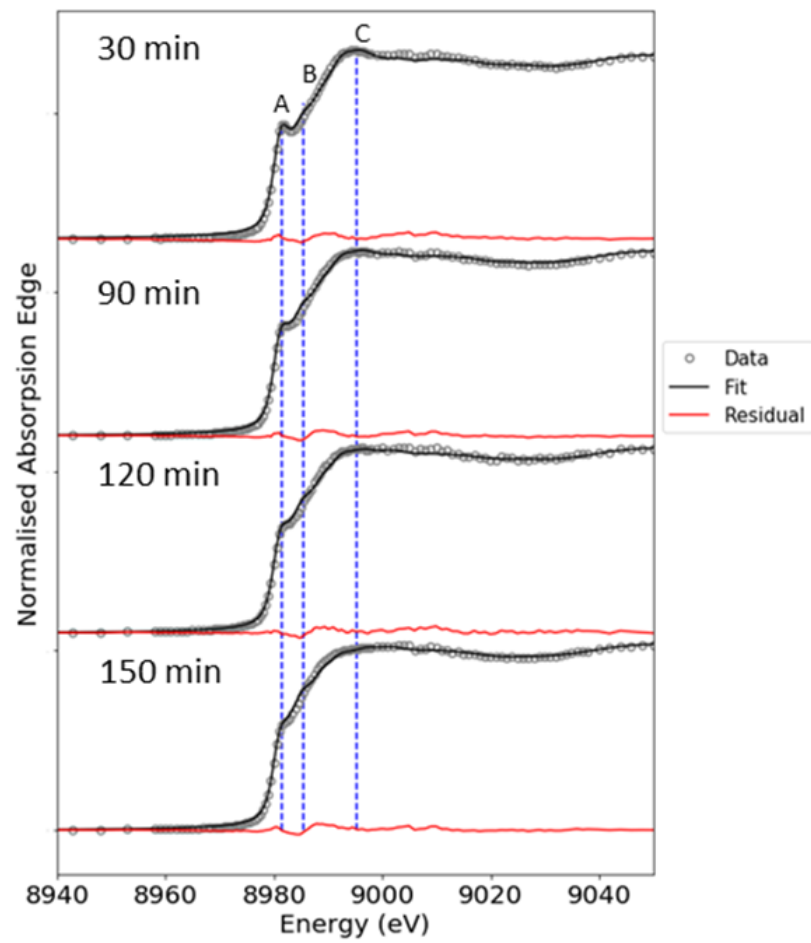
(a)
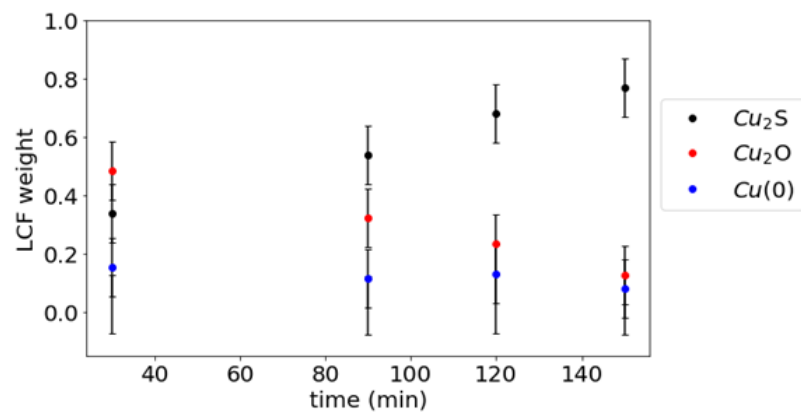
(b)

Figure 4.4.4 (a) Normalized Cu K edge, XANES spectra of ex situ samples undergone HTCBT for 30 – 150 min, with 0.1 wt % MoDTC, and (b) The composition results from LCF analysis plotted against time.

The same sample measured on XPS is also characterized by XANES measured via He-flow TEY. He-flow TEY provides near-surface chemical information up to 2810 Å at the Cu K edge.[103,119] All four spectra obtained from the coupons have the same edge position at 8980.22 eV, suggesting little or no CuS and CuO components. The 1 s $\rightarrow$ $4p_{xy}$ transition for Cu_2O and Cu_2S are found at 8981.16 eV and 8981.84 eV, respectively. Similar features are found on the spectra measured for the coupons immersed from the HTCBT with 0.1 wt% MoDTC at 30 – 150 min (Figure 4.4.4a). A distinct peak on the rising edge is present on the 30 min sample at 8981.58 eV and 8995.30 eV, labelled as A and C, similar to peaks found on the Cu_2O spectra. This peak becomes less distinct and more similar to the shoulder features observed at 8981.45 eV in the Cu_2S spectra.

Furthermore, at 150 min, another shoulder feature, labelled as B, is observed at 8985.5 eV, similar to the shoulder feature in the Cu_2S. This qualitative analysis points to a transition of Cu_2O to Cu_2S with succeeding samples. Linear combination fitting (LCF) was performed to analyze these spectra to quantify the chemical composition of the surface. These spectra are used in the LCF analysis in the range -30 eV $<$ E_0 $<$ 70 eV.

CuS is absent in all samples, and very little CuO is detected - less than the error associated with LCF analysis of 10%. The spectra obtained for the copper coupons contain Cu (0) of 8 – 15%. The Cu (0) component decreases as a function of the duration of the HTCBT. However, the variation of the Cu(0) component, measured across the samples, is within the error of LCF (>10%).

The LCF analysis shows a clear trend of the Cu_2S component increasing and the Cu_2O decreasing as a function of time spent in the HTCBT with 0.1 wt% MoDTC (Figure 4.4.4b). From XPS, only Cu_2S is detected in the Cu 2p spectra for the samples prepared in HTCBT with 0.1 wt% MoDTC at 30 – 150 min (Figure 4.4.2e). In the samples measured by XANES, Cu_2S is also detected as a component. However, Cu_2O and Cu(0) are also detected (Figure 4.4.4). The two characterization techniques provide different information depths, with XPS sensitive to 1-10nm and He-flow TEY at the Cu K-edge sensitive to 280 nm.[77,103–107] As Cu_2S is in the uppermost surface, detected by XPS and XANES. The near-surface (> 10 nm below

the surface) is a Cu_2O layer detected by XANES but not XPS. In addition, Cu(0) is also detected; this is due to the thickness of the overall tarnish layer $(Cu_2S + Cu_2O) < \sim 300\,nm$ (the information depth of He-flow TEY).

Self-absorption was discussed in section **Error! Reference source not found.** in the context of measurements of Cu foil using this cell. Fluorescent photons ionizing the contaminated He supply introduced self-absorption effects in the measured TEY signal (Figure 6.4.7). However, self-absorption is apparent in the spectra measured here. However, it must be noted that the major component of tarnish is Cu_2S, where the spectra have no pre-edge features and weak oscillations in post-edge. With these characteristics, it is difficult to assess whether the spectra contain self-absorption effects.

In any case, although the spectra may have self-absorption effects, assuming that the air-contamination level in the He supply, the degree of self-absorption contained in the spectra is constant. Therefore, the trends observed in Figure 4.4.4b are valid.

4.4.2   Temperature effects – Base Oil
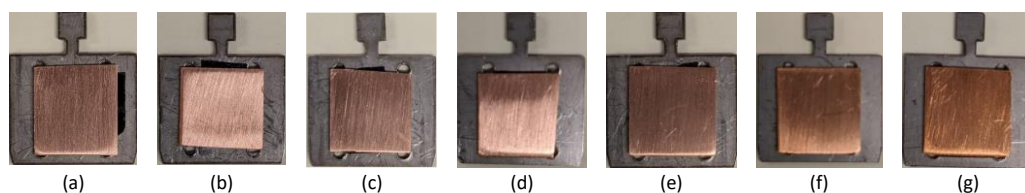
Figure 4.4.5 Images of Cu coupons samples submerged in a base oil for 10 min at temperatures (a) 55 ^{o}C, (b) 65 ^{o}C min, (c) 75 ^{o}C, (d) 85 ^{o}C, (e) 95°C, (f) 105 ^{o}C and (g) 115°C. The samples are mounted on Omicron sample holders. The images are taken prior to XPS measurements.

Seven Cu samples are prepared using the temperature effect experimental method (discussed above) with base oil. The Cu samples were submerged in base oil for 10 min at 55 -115°C. Figure 4.4.5 shows images of the Cu coupon samples mounted on Omnicron sample holders prior to XPS measurements. Comparing the samples' appearance shows that the samples submerged at 55 – 95°C appear to remain untarnished, while the samples submerged at 105 – 115°C have a darker appearance.

Base oil

Atomic Percent (%)

Temperature (°C)

	C 1s	O 1s	Cu 3s
55	42 ±1	17 ±1	40 ±1
65	37 ±1	19 ±1	44 ±1
75	42 ±1	20 ±1	38 ±1
85	48 ±1	21 ±1	31 ±1
95	38 ±1	23 ±1	39 ±1
105	47 ±1	21 ±1	32 ±1
115	45 ±1	26 ±1	29 ±1

Table 4.4.2 XPS survey results for the elemental composition in atomic % for Cu coupons submerged in based oil.
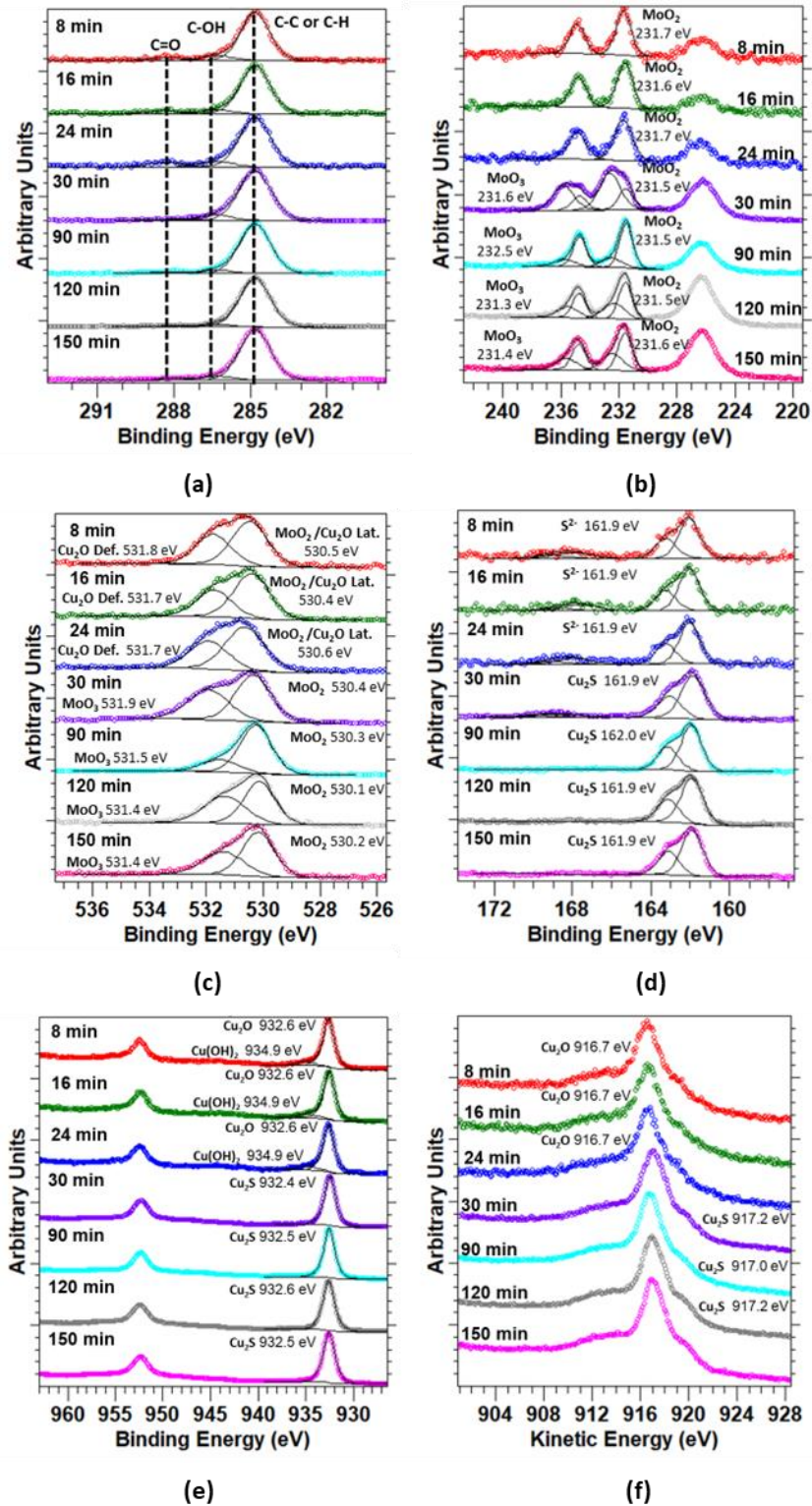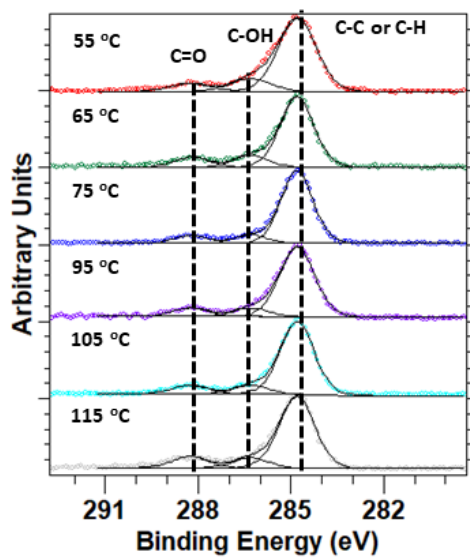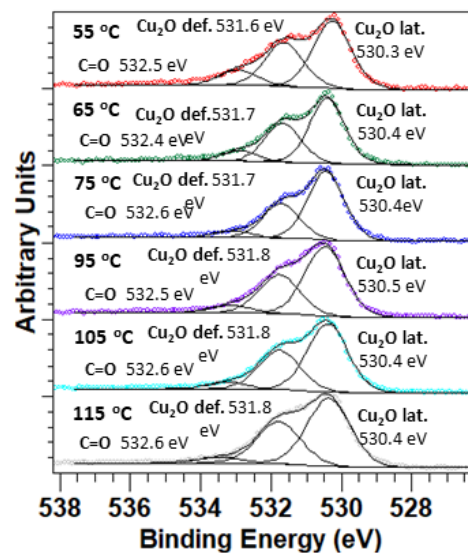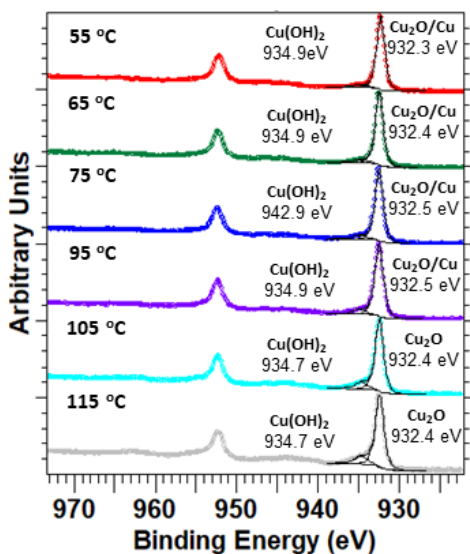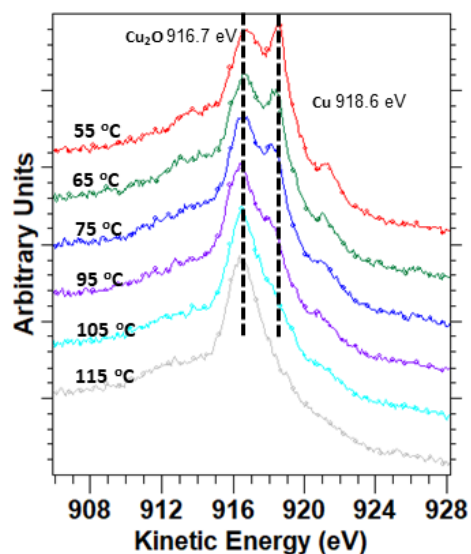
Figure 4.4.6 High-resolution core-level XPS spectra of (a) C 1s, (b) O 1s, (c) Cu 2p, and (d) the high-resolution Auger spectra of Cu $L_3M_{4,5}M_{4,5}$ of samples submerged in base oil for 10 min at temperatures 55 - 115°C. The spectrometer has a resolution of 0.7 eV, and the energy calibration procedure introduces a 0.2 eV error to the position quoted to the fitted components.

Ex situ samples of Cu coupons submerged in base oil for 10 min at various temperatures between 55-115°C characterized by XPS. Table 4.4.2 shows the survey results in atomic percentage, and Figure 4.4.6 shows normalized, high-resolution, core-level spectra of the elements on the surfaces.

The C 1s spectra (Figure 4.4.6a) are fitted with three components positioned at 284.8 eV, 286.3 eV, and 288.3 eV attributed to C-C or C-H (aliphatic carbon), C-OH, and C=O, respectively, with an FWHM, = 1.2 - 1.3 eV. The aliphatic carbon photoemission peak at 284.8 eV energy calibrates each spectrum.

Three components are fitted on the O 1s spectra (Figure 4.4.6b), positioned at 530.2 - 530.5 eV (FWHM = 1.1-1.4 eV), 531.6 -531.8 eV (FWHM = 1.1 – 1.4 eV) and 532.4 - 532.6 eV (FWHM = 2 eV). These peaks are attributed to Cu_2O lattice, Cu_2O defective, and C=O (carbonyl), respectively.

The Cu $2p_{3/2}$ is fitted with two components (Figure 4.4.6c) at positions 932.3-932.5 eV (FWHM = 1.1-1.2 eV) and 934.6-934.9 eV (FWHM = 1.8 eV) attributed to Cu_2O/Cu metal and $Cu(OH)_2$ respectively. With qualitative analysis, it is immediately observed that the area attributed to $Cu(OH)_2$ increases with increasing temperature. Performing quantitative analysis becomes more difficult with an increasing portion of $Cu(OH)_2$, which produces a strong satellite feature. A reliable background is more challenging to attain with an increasing satellite feature. Challenges in establishing a background would also explain the variations in the binding energy positions.
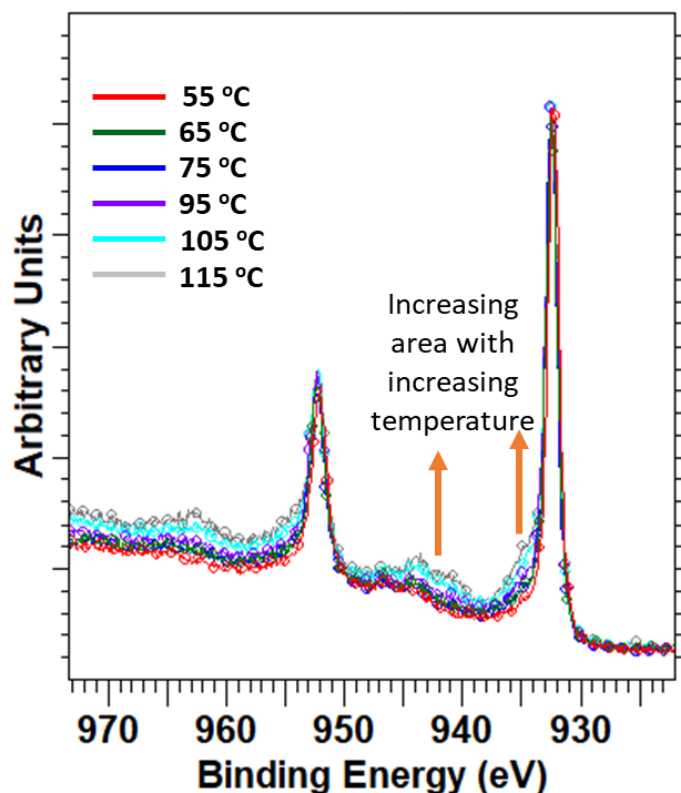
Figure 4.4.7 Overlayed plot of Figure 4.4.6c. High-resolution core-level XPS spectra of Cu 2p samples submerged in 0.1 wt % MoDTC for 10 min at 55 - 125°C. The spectrometer has a resolution of 0.7 eV, and the energy calibration procedure introduces a 0.2 eV error to the position quoted to the fitted components.

Two peaks are present in the Cu $L_3M_{4,5}M_{4,5}$ Auger spectra (Figure 4.4.6d) at 916.7 eV and 918.6 eV (kinetic energy scale) attributed to Cu_2O and Cu metal, respectively (an Auger peak is not observed for $Cu(OH)_2$. The Cu $L_3M_{4,5}M_{4,5}$ have higher kinetic energy than the Cu 2p and it, therefore, less surface sensitive.) At 55 °C the surface of the coupon has a high Cu metal content. At increasing temperatures, the Auger peak at 918.6 eV reduces relative intensity while the peak at 916.7 eV increases.

4.4.3   Temperature effects – MoDTC
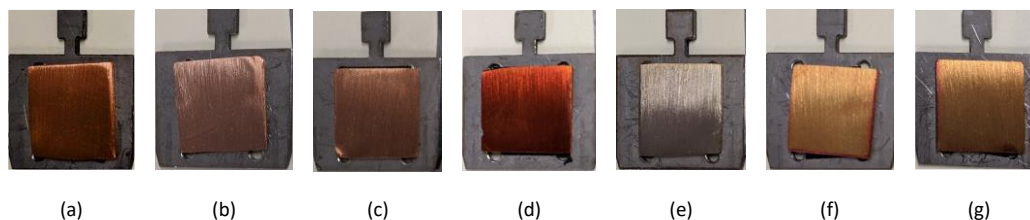
Figure 4.4.8 Images of Cu coupons samples submerged in 0.1 wt% MoDTC blend for 10 min at temperatures (a) 55°C, (b) 65°C min, (c) 85°C, (d) 95°C (e) 105°C, (f) 115°C and (g) 125°C. The samples are mounted on Omnicron sample holders. The images are taken prior to XPS measurements.

Seven Cu samples are prepared using the Temperature effect experimental method (discussed above) with 0.1 wt% MoDTC in base oil. The Cu samples were submerged in base oil for 10 min at 55 -125°C. Figure 4.4.8 shows images of the Cu coupon samples mounted on Omicron sample holders prior to XPS measurements. The appearance of the samples shows no trend. In the initial stage of tarnish formation, birefringence may occur. The appearance of the sample is related to the thickness of the film.

Atomic Percent (%)

Temperature (°C)	O 1s	C 1s	Mo 3d	S 2p	Cu 3s
55	16 ±1	38 ±1	0 ±1	0 ±1	46 ±1
65	14 ±1	45 ±1	0 ±1	0 ±1	41 ±1
85	11 ±1	51 ±1	1 ±1	7 ±1	30 ±1
95	15 ±1	45 ±1	2 ±1	11 ±1	28 ±1
105	12 ±1	42 ±1	1 ±1	9 ±1	35 ±1
115	14 ±1	39 ±1	2 ±1	14 ±1	30 ±1
125	13 ±1	37 ±1	2 ±1	11 ±1	38 ±1

Table 4.4.3 XPS survey results in atomic Percent of Cu coupons submerged in 0.1 wt % MoDTC for 10 min at temperatures 55 – 125° C.
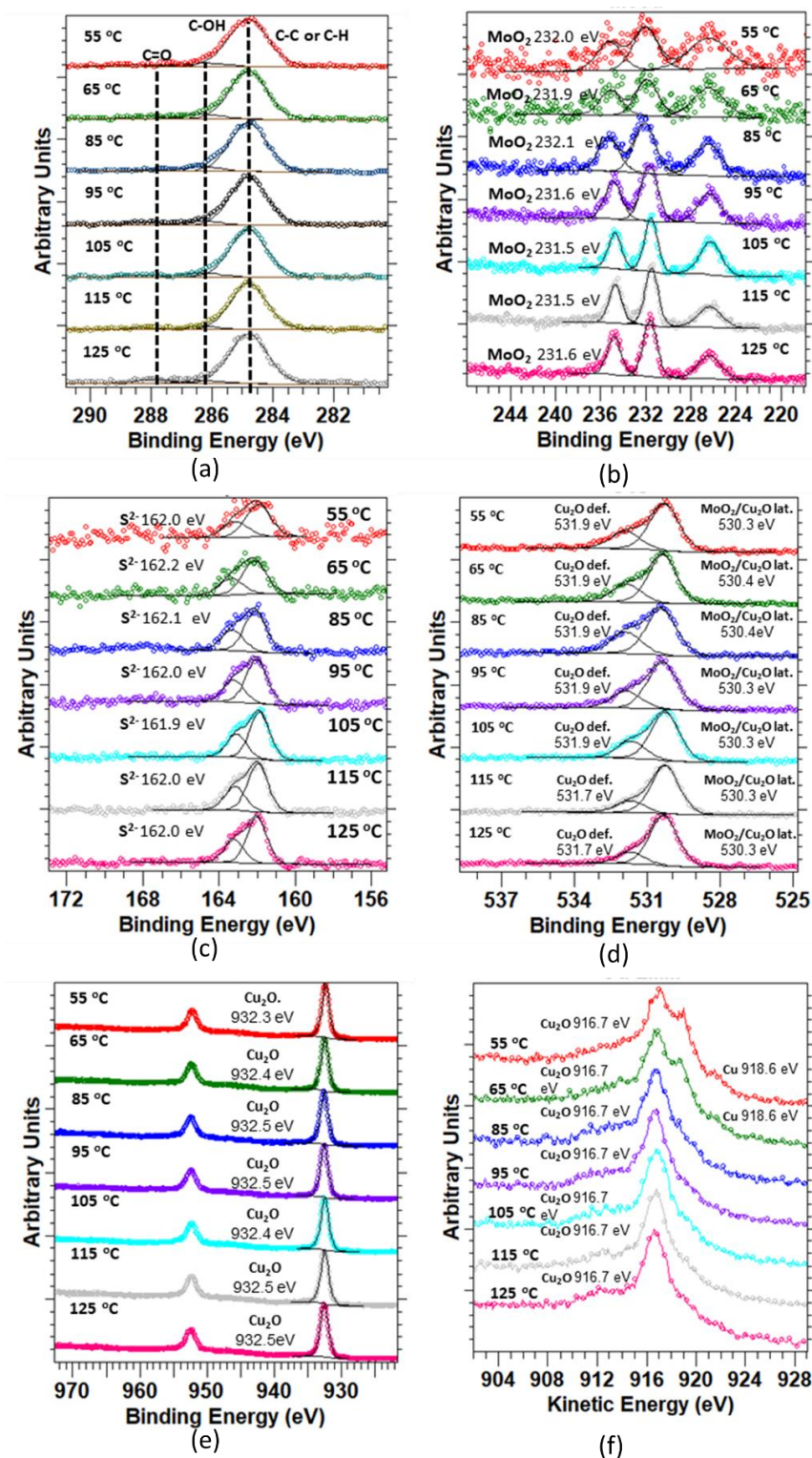
Figure 4.4.9 High-resolution core-level XPS spectra of (a) C 1s, (b) Mo 3d, (c) S 2p, (d) O 1s, (e) Cu 2p, and (f) the high-resolution Auger spectra of Cu $L_3M_{4,5}M_{4,5}$ of samples submerged in 0.1 wt % MoDTC for 10 min at temperatures 55 - 125°C. The spectrometer has a resolution of 0.7 eV, and the energy calibration procedure introduces a 0.2 eV error to the position quoted to the fitted components.

Ex situ samples of Cu coupons submerged in 0.1 wt % MoDTC for 10 min at various temperatures between 55-125°C were characterized by XPS. Tab.2 shows the survey results in atomic percentage, with Figure 4.4.9 showing normalized, high-resolution, core-level spectra of the elements on the surfaces.

The C 1s spectra (Figure 4.4.9a) are fitted with three components positioned at 284.8 eV, 286.3 eV, and 288.3 eV attributed to C-C or C-H (aliphatic carbon), C-OH, and C=O, respectively, with an FWHM, = 1.4 - 1.5 eV. The aliphatic carbon photoemission peak at 284.8 eV is used to energy calibrate every spectrum.

Each spectrum shows a broad peak at ~226.5 eV corresponding to S 2s (Figure 4.4.9b). A set of doublet peaks is fitted to the Mo 3d. The binding energy position of the Mo $3d_{5/2}$ is 231.5 - 232.1 eV attributed to MoO_2. At 55 - 85°C, the Mo $3d_{5/2}$ peak has higher binding energy positions than at 95-125°C. This is ascribed to errors associated with fittings. The figure plots normalized spectra. However, the signal-to-noise ratio is minimal at 55°C and 65°C, with very large FWHM at 2.6 eV and 2.2 eV, respectively. At half maxima, the fitted component of the Mo $3d_{5/2}$ is still within the noise level. At 85 °C the FWHM is still very large at 2.2 eV. The poor signal-to-noise ratio and large FWHM lead to varying binding energy positions when fitted with components. At temperatures 85°C and above, the signal-to-noise ratio is much higher, with sharper peaks.

The S 2p spectra are fitted with doublet peaks (Figure 4.4.9c) set with the $2p_{3/2}$ binding energy position at 161.9-162.2 eV (FWHM = 1.2-1.5 eV). These are attributed to S^{2-} (sulphides). At temperatures 55 - 85°C, the S $2p_{3/2}$ peak has higher binding energy positions when compared to the binding energies At temperatures 95-125°C. This is ascribed to errors associated with fitting. Similar to Mo 3d, the S 2p signal-to-noise ratio is very low at 55 – 85°C, with large FWHM at 1.4 -1.5 eV. The poor signal-to-noise ratio and large FWHM lead to varying binding energy positions when fitted with components. At temperatures 85°C and above, the signal-to-noise ratio is much higher, with sharper peaks.

The O 1s spectra are fitted (Figure 4.4.9d) with two components with binding energy positions 530.3 eV (FWHM = 1.3-1.4 eV) and 531.8 eV (FWHM = 1.3 - 1.4 eV) attributed to Cu_2O/MoO_2 and defective Cu_2O.

The Cu 2p spectra are fitted with a single component (Figure 4.4.9e) with binding energy position a 932.3-932.5 eV (FWHM of 1.2 - 1.4 eV) attributed to $Cu_2O/$ C metal. The $55^{\circ C}$ and $65\,^{\circ}C$ Cu $L_3M_{4,5}M_{4,5}$ spectra (Figure 4.4.9f) show two Auger peaks at the lower temperatures at $55\,^{\circ}C$ and $65\,^{\circ}C$, at 916.7 and 918.6 eV (kinetic energy scale), corresponding to Cu_2O/Cu metal respectively. At $85\,^{\circ}C$ and above, the Cu $L_3M_{4,5}M_{4,5}$ has one Auger peak at 916.7 eV corresponding to Cu_2O.

4.5 Discussion

The non-aqueous chemistry of MoDTC on Cu surfaces was studied under oxidative conditions. Analysis by XPS and XANES via TEY was possible. However, studying chemical reactions leading to corrosion in a fully formulated lubricant is a complex analytical problem.[120,121] The experiments described in this work have the advantage of using a homogeneous and well-characterized sample as a starting point.

A mechanism for MoDTC decomposition has been proposed by Grossiord et al. based on results obtained from XPS analysis.[66] The proposed mechanism outlines two stages for the decomposition of MoDTC; (i) the thiocarbamate groups dissociate from the MoDTC molecule via the Mo–S bond, leaving the $Mo_2S_2O_2$ radical core and two thiocarbamate radicals. (ii) The two thiocarbamate groups combine via the S–S bond, forming thiuram disulphide, while the $Mo_2S_2O_2$ core decomposes to form MoS_2 and MoO_2. Then, MoO_2 is further oxidized to form MoO_3.

During tribological testing of MoDTC, friction reduction is observed following an initial induction phase.[58,67,98,122] It was proposed that the induction phase is due to the adsorption of thiuram disulphide on the surface.[58,59,120] In sliding conditions, the adsorbed molecules mechanically shear off these molecules, exposing the metal's surface.

4.5.1 HTCBT with 0.1 wt% MoDTC

As the Cu coupons were prepared in ambient air, it is expected that a native oxide layer on the surface would form prior to the HTCBT.[29] The chemical evolution of the Cu surface through the HTCBT shows a transition from the native oxide state to Cu_2O and finally to Cu_2S, as observed by XPS (Figure 4.4.2e and Figure 4.4.2f) and XANES (measured via TEY) (Figure 4.4.4). Cu_2S is the expected end product of S-driven Cu corrosion in lubrication formulation[123,124].

The HTCBT does not incorporate a sliding contact; the surface is expected to continue to adsorb thiuram disulphide until saturation, which would have a significant N 1s signal. The N 1s overlaps with Mo $3p_{3/2}$ and therefore requires peak fitting to quantify the amount of nitrogen on the surface. However, a significant N 1s signal was not observed on the survey spectra (Table 1). Also, two chemical environments are expected for adsorbed thiuram disulphide (Cu-S-C and S=C). However, only one environment is measured on the S 2p spectra (Figure 4.4.2c). The nature of these sulphides measured at 8-24 min is unclear, and a previous study has also reported the measurement of sulphides using NEXAFS (concluding that the sulphides measured are different from the MoS_2).[60] The sulphides measured 30-150 min are Cu_2S confirmed using XANES.

In agreement with previous studies, MoO_2 and MoO_3 are detected on the surface of the Cu coupons (Figure 4.4.2b).[58–60,120,125] This signifies the breakdown of MoDTC, although a mechanism cannot be inferred directly from this study alone.

4.5.2 Temperature effects – Base Oil

The oxidation of base oil follows a free radical chain reaction. The reactions that initiate the free radical chains are thermally activated (and can be further aided with metal catalysis).[42] As the chain reaction occurs, peroxy radical adsorbs on the surface of the Cu, where two electrons are donated to the radical by Cu. The adsorbed radical then cleaves via the O-O bond leaving behind an oxygen (Figure 4.5.1a). This mechanism occurs on the surface of the coupon. Where the uppermost surface is saturated with a layered oxide, electrons diffusing

through the oxide are donated to the radical. The oxygen diffuses into the bulk via grain boundary diffusion (also aided by the increased temperature), increasing the thickness of the oxide layer (Figure 4.5.1b).[42,126]
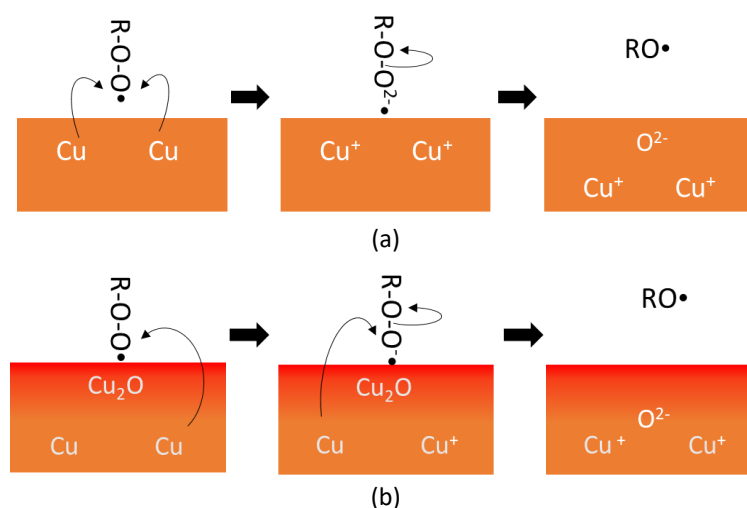
Figure 4.5.1 Schematic diagram for the proposed oxidation mechanism of (a) Cu metal surfaces and (b) further oxidation of Cu2O in the base oil.

This mechanism could explain the increasing Cu_2O with temperature. As the temperature increases, the production of peroxy radicals increases, converting the Cu metal to Cu_2O. As the base oil oxidizes, creating peroxides, Fenton-like chemistry could also occur where a self-catalyzing process can produce $Cu(OH)_2$. As the production of peroxides is also thermally activated, this would explain the increasing $Cu(OH)_2$ with temperature.[42,127]

4.5.3   Temperature effects – MoDTC

Adding MoDTC to the oil inhibits the production of $Cu(OH)_2$ (Figure 4.4.9e). The sulphides produced from additive decomposition act as antioxidants – reacting with peroxide and preventing reactions with Cu.[128] It is, however, still observed from the Cu $L_3M_{4,5}M_{4,5}$ that Cuconverts to Cu_2O (Figure 4.4.9f).

The temperature effects of submerging Cu coupons in 0.1 wt% MoDTC produce expected products on the surface, such as sulphides and MoO_2 (Figure 4.4.9b and Figure 4.4.9c), that

74

have been previously reported.[61,66,122,129,130] There are no changes in the chemical nature of S and Mo on the surface of the coupon. It is, however, observed that as the temperature increases, more Mo and S are measured on the surface (tab.2) – this trend was previously observed using EDX studies.[120] The chemical nature of the Mo and S remains the same across 55 - 115℃, inferring that the chemical breakdown of MoDTC occurs in the liquid phase with the resulting decomposition products reacting with the coupon's surface.

4.5.4 Proposed Corrosion Mechanism

In the decomposition mechanism proposed by De Feo et al. (2015) it was posited that MoDTC breaks down in two stages. (1) At high temperatures, the MoDTC molecule loses two S atoms from the structure by reacting with oxygen. (2) The molecules decompose to form secondary amines, CO_2, and MoO_xSy particles. [67]

The lost S atoms from MoDTC react with the radicals in oil, forming stable sulphide, which deposits on the surface of the coupon. These could also explain the sulphides detected by Kasrai et al. (1998).[61] Such sulphide could be responsible for the S 2p detected in the HTCBT experiments from 8-24 min (Figure 4.4.2d) and again when submerging Cu coupon in 0.1 wt % MoDTC from 55-105℃ (Figure 4.4.9c).

As peroxy radicals in the oil react with the coupon's surface to produce Cu_2O, followed by an interaction with MoO_xS_y on the surface. Ion exchange between S^{2-} from the MoO_xS_y particles and the O^{2-} on the surface of the coupon produces Cu_2S and MoO_2 (Figure 4.5.2). As Cu_2S grows in thickness, the exchange of S^{-2} and O^{2-} occurs via grain boundary diffusion, aided by the high temperature of the HTCBT.[126]
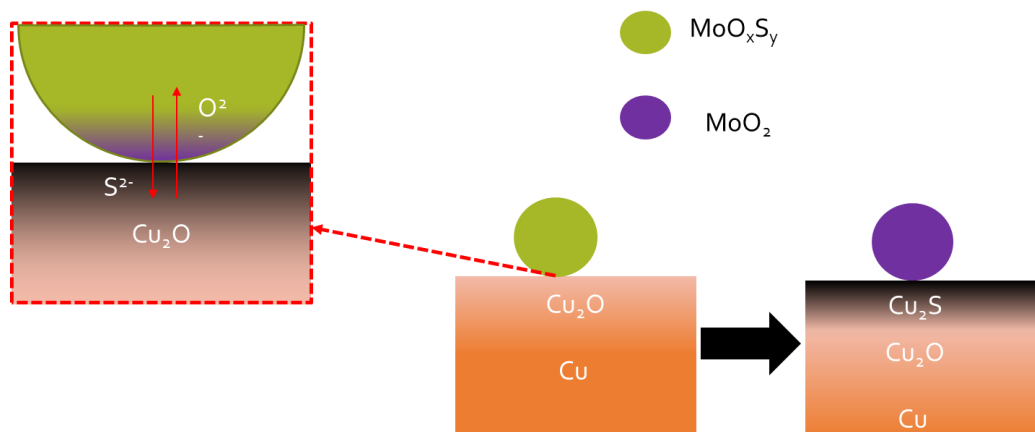
Figure 4.5.2 Schematic diagram of the ion exchange between O^{2-} (on the Cu surface) and S^{2-} (from the MoO_xS_y) forming Cu_2S as the corrosion product.

4.6 Conclusions

This study has investigated the interaction of MoDTC and Cu and the chemical transformation leading to corrosion. The interaction was investigated in the HTCBT conditions. Separate experiments were also conducted to understand further the effects of temperature on Cu's interaction in the solution.

The fundamental investigation of the interaction of the Cu surface with base oil showed that at the same time interval, the produced Cu oxide layer increases as the temperature increases. Furthermore, $Cu(OH)_2$ becomes more abundant on the surface with increasing temperatures. This indicates that increasing temperature increases peroxide production, allowing Fenton-like chemistry. However, with the addition of 0.1 wt % MoDTC, $Cu(OH)_2$ is no longer observed. This is attributed to the production of sulphide acting as antioxidants inhibiting reactions leading to the formation of $Cu(OH)_2$.

The Cu coupon's chemical composition on the surface was characterized using XPS and XAS via TEY. The TEY results show that during the HTCBT, the Cu coupon forms an oxide layer which is then replaced by a sulphide layer. This is also observed with the XPS data. Based on

XPS and XAS results obtained in this study, a corrosion mechanism of Cu by MoDTC has been proposed.

5 Corrosion of Copper by ZDDP under Non-Aqueous Conditions of the High-Temperature Corrosion Bench Test

5.1 Abstract

In combustion engines, copper (Cu) based alloys are replacing lead (Pb) alloys in bearings because of growing concerns about the environmental impact of Pb. Zinc dialkyl dithiophosphates (ZDDPs) are widely used antiwear additives in lubricant formulations. The chemistry of ZDDPs on steel surfaces has been studied extensively and with a wide range of characterisation techniques, but little research has been done to understand their interaction with Cu. As ZDDPs contain sulphur (S) moieties, Cu is susceptible to corrosion by sulfidation, which has a detrimental effect on bearing and engine life span. The interaction of ZDDP Cu was therefore investigated under the conditions of the high-temperature corrosion bench test (HTCBT). X-ray photoelectron spectroscopy (XPS) was applied to monitor the surface composition. The results indicate the initial formation of a thiophosphate thermal film. The composition of this thermal film is dependent on the concentration of ZDDP in the oil. With 1.0 wt%, the thermal film forms a thick layer, visible by the eye, a thiophosphate layer. In this thiophosphate layer, Cu^{2+} appears to be included in the thermal film - replacing Zn^{2+}. The removal of this overlayer exposes the Cu surface in the vicinity of the surface deposits formed by ZDDP, facilitating the reaction of thiols with Cu to form Cu_2S. In contrast, smaller concentrations of 0.1 wt% produce a thermal film containing Zn and Cu oxides as well as Zn and Cu thiophosphate. A similar reaction then takes place where Zn^{2+} is replaced by Cu^{2+}. However, the final tarnish layer formed on the surface is due to a hydrocarbon overlayer, not Cu_2S, unlike HTCBT with 1.0 wt% ZDDP. Finally, using Ar^+ etching, the structure of the thermal film is studied. The depth profiling measurements are in good agreement with the chemical profile reported in the literature.

5.2 Introduction

Engine bearings allow load transmission between the crankshaft and piston and convert reciprocating motion to circular motion. The bearing movement must be associated with low friction and high resistance to wear and corrosion.[14] Achieving this requires materials combining sufficient hardness and elastic deformability, such as copper (Cu). Cu has good embeddability for particles that may become entrained in the oil under the extreme conditions in reciprocating boundary layers.[3] Corrosion of engine bearings reduces engine lifetime and may ultimately lead to engine failure. Lead (Pb) has been widely used in bearing in the past but is being phased out by engine manufacturers due to the environmental concerns arising from its emission from the engine. Understanding the corrosion and wear of Cu in contact with lubricants has consequently become of interest to engine and lubricant manufacturers.

Zinc dialkyl dithiophosphates (ZDDPs) are arguably among the most widely used lubricant additives in the commercial sector. The earliest report of ZDDP use dates back to the 1940s. With patents filed by Lubrizol, Union Oil and American Cyanamid.[6] In modern lubrication formulations ZDDPs are still used as antiwear additives. Its antiwear action arises from the formation of glassy phosphate tribofilms under shear in the boundary layer between the moving steel surfaces[58,99,131] and due to thermal film formation.[132] The thermal film forms pad-like structures with thicknesses of ~100 nm. This provides corrosion protection as thermal film acts as a passivating layer on the metal surface. [121,133,134]

Chemical pathways for the degradation of ZDDPs were proposed as early as 1981.[49] Insoluble zinc thiophosphates were observed as white precipitates. When transported in the engine exhaust, precipitates are known to deactivate catalytic converters downstream of the engine[135] due to thiophosphate ligand exchange with other metal ions. The relative order of preference thiophosphate binding is[6,136]

$$Pd^{2+} > Au^{3+} > Cu^{+} > Cu^{2+} > Fe^{3+} > Pb^{2+} > Zn^{2+}$$

ZDDP has also been considered an antioxidant additive since the 1940s. This characteristic is mainly due to its ability to react with hydroperoxides and peroxy-radicals,[137–140] quenching free radical chain reactions.[42]

An extensive body of tribology research on ZDDPs in steel and iron contacts has led to a detailed understanding of the ZDDP surface chemistry on these materials.[58,99,134,141–143] Comparatively little attention has been paid to the interaction of ZDDPs with Cu surfaces. For Cu and other soft metals (such as Pb), it is of particular interest that ZDDPs, while widely used and effective antiwear additives in commercial lubricant formulations, contain sulphur (S) moieties that may form thermodynamically stable sulfidic phases with these metals. Corrosion by sulphide film formation is detrimental to the lifetime of soft metal parts, ultimately impacting on engine performance and lifetime if not controlled or mitigated against.

The ASTM D6594, more commonly referred to as the high-temperature corrosion bench test (HTCBT), is one of the most widely used industrial laboratory tests for determining whether lubricant formulations corrode metals used in automotive combustion engines.[7] In an HTCBT, the extent of metal corrosion by a lubricant formulation is qualitatively determined by exposing the metal to an aerated lubricant formulation at a temperature of 135°C. The extent of corrosion is monitored by visual evaluation of the degree of metal tarnishing. No chemical analysis of the metal surfaces and the corrosion films is prescribed in the specification of the HTCBT test.[7] Any rational design of lubricant formulations with wear and corrosion protection performance would benefit from an additional identification of the chemical phases formed at the lubricant/metal interface. Here it will be shown how chemical and mechanistic insight into the ZDDP-induced surface phases on Cu metal can be obtained by accompanying HTCBTs with X-ray photoelectron spectroscopy (XPS) analysis of the metal surfaces. XPS is the most widely used chemical surface analysis technique. Time-dependent XPS determination of the chemical state of the Cu surfaces will provide insight into the evolution of surface phases as a result of prolonged exposure of Cu surfaces to ZDDP model formulations under HTCBT conditions.

5.3 Experimental

Cu substrates (approx. 1 cm x 1 cm x 0.9 mm coupons, 99.9%) were obtained from Infineum UK ltd. They were polished using a series of abrasive paper (SiC, P400, and P250 grit) treatments and finished with (SiC, P1200) abrasive powder. The resulting surface was rinsed with cyclohexane, which was immediately mechanically removed from the surface by a stream of compressed air, which also evaporated any excess of cyclohexane adhering to the metal. The 1.0 wt% ZDDP model lubricant formulation was prepared by diluting concentrated ZDDP (Zinc bis[O-(6-methylheptyl)] bis[O-(sec-butyl)] bis(dithiophosphate), $\geq 70\%$ - $<90\%$) with DURASYN® 164 polyalphaolefins (group IV base oil, 100 % obtained from Collinda). The diluted solution was then stirred with a magnetic stirrer for a minimum of 2 hours to ensure dissolution into a homogeneous phase.
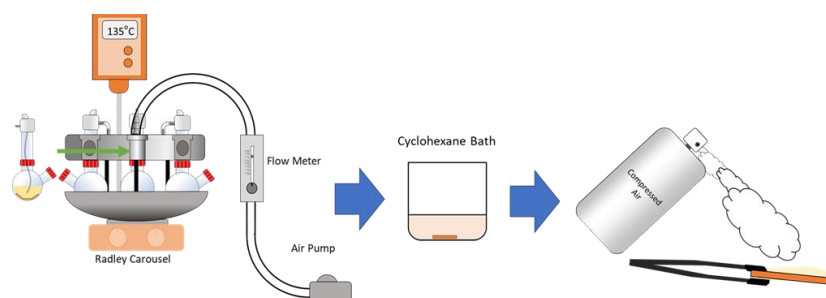
(a)
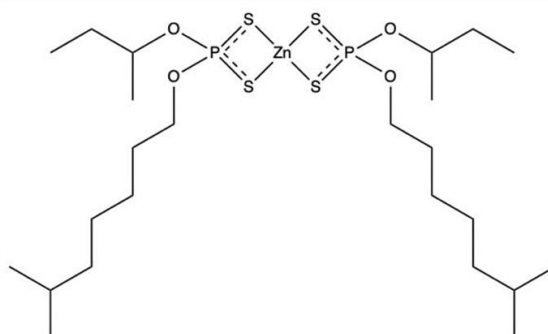
(b)

Figure 5.3.1 (a) Schematic flow diagram of the experimental procedure of a modified HTCBT and (b) the chemical structure of ZDDP used in these experiments.

A modified HTCBT test was performed in round bottom flasks containing Cu coupons and 150 ml lubricant solution. The round bottom flasks were placed in a Radley 6 Plus Reaction Station™ carousel heater platform, which also provides a gas manifold for controlling the gas atmosphere in the round bottom flasks through a continuous flow of the gas. The temperature of the lubricant was maintained at 135°C using a feedback thermocouple placed at the base of the Carousel. A stream of ambient air was bubbled through the solution in each flask using a diaphragm air pump, with a rate of 5 L h^{-1} controlled by a mass flow meter (Figure 5.3.1).

To monitor the progress of corrosion by the lubricant/air treatment, a coupon were periodically removed from each round bottom flask. The coupons were rinsed with cyclohexane to remove excess oil and blown dry with compressed air. The coupons were stored in 10 ml clip-top glass vials until characterisation was performed.

XPS spectra were collected with a Specs FlexMod ultra-high vacuum (UHV) instrument equipped with a monochromatic Al K$_\alpha$ X-ray source (1486.71 eV) that operated with a power of 40 W. The kinetic energy of the photoelectrons was determined with a Phoibos 150 electrostatic hemispherical analyser with 1D delay line detectors, operating in a small-area mode with a source–analyser angle of 55°. The Cu coupons were mounted on standard Omicron sample holders using double-sided carbon adhesive tape. Spectra were collected at ambient temperature at a base pressure of 10^{-9} mbar. Survey spectra were collected as a single scan with a step size of 1 eV, a pass energy of 50 eV and a dwell time of 100 ms. High-resolution core-level spectra were collected with a step size of 0.1 eV, a dwell time of 100 ms per data point, and a pass energy of 30 eV. Under these conditions, the instrument achieves a resolution of approximately 0.7 eV, comparable to the natural line width of the photoemission lines.

The spectra were analysed quantitatively using CasaXPS.[76] The analyser transmission function of the XPS instrument was determined exactly as reported in a recent VAMAS round-robin study, which confirmed the accuracy of the instrument for quantitative analysis.[100] For the elemental analysis, the overall intensities of the strongest emission lines for all elements were determined and corrected using the relative sensitivity factors reported by Scofield 1973.[101]

For the chemical state analysis from the high-resolution spectra, Shirley backgrounds and a GL (30) line shape (30% Lorentzian, 70% Gaussian) were used to model all components evident in the emission lines. For Cu $2p_{3/2,}$ a Shirley background and a GL (80) line shape (80% Lorentzian, 20% Gaussian) were used for the fit. The C 1s spectra were used for calibration of the electron binding energy (BE) scale. The C 1s emission was modelled using GL (30) lines to identify components from unsubstituted aliphatic carbon and BE-shifted components associated with carbon bounds to electronegative heteroatoms. A second component at ~1.5 eV above the main unsubstituted aliphatic component was fitted with the same full width at half maximum (FWHM). This higher binding energy (BE) component is associated with carbon singly bonded to oxygen from alcohol (C-OH) and/or ether (C-O-C) functional groups. Higher BE components were fitted as appropriate (e.g. for carbonyl carbons, such as C=O, 2.8 -3.0 eV above the main aliphatic peak, and carboxylate/carboxylic acid groups, COO⁻/COOH, at BEs that are 3.6–4.3 eV above the unsubstituted aliphatic peak). Calibration of the binding energy scale was then carried out by setting the centroid BE of the unsubstituted aliphatic component to 284.8 eV. Spectra were also carefully checked for evidence of residual charging (especially differential charging) and the possibility that electrically insulating surface layers may be formed, for which the Fermi energy of the substrate may not be a representative reference point. This careful calibration protocol achieves a reproducibility and error of approximately ± 0.1 - 0.2 eV.[75,102]

5.4 Results

5.4.1 Modified HTCBT with 1.0 wt% ZDDP

Cu samples prepared using the modified HTCBT method with 1.0 wt% ZDDP in base oil were emersed from the solutions at 15, 24, 40, 48, 63 and 168 h. Photographic images of the samples taken right after emersion from the solution are displayed in Figure 5.4.1. The overall trend becoming apparent from these images is that initially, a homogeneous brown tarnish layer is formed, which, after 15 h, is thick enough to obscure the striations on the Cu surface caused by the SiC grit in the polishing process. The brown tarnish layer covers the whole surface homogeneously. After 24 h, this tarnish layer is not evident anymore. It has given way to a Cu

surface that looks metallic, with the scratches from polishing visible again. Then a second phase of tarnishing sets in, which continuously increases in severity as time progresses. Up to 48 h, tarnishing is not so strong as to obscure the surface roughness created by the SiC grit in the preparation of the samples. Moreover, tarnishing at the edges appears to be stronger than in the centre of the samples, likely due to the high density of surface defects near the edges. At 48 h, the formation of a more intense, dark brown tarnish layer spreading over the surface from the top and bottom edges becomes apparent; by 63 h, the whole surface is covered in the dark brown layer, and even more severe, almost black tarnish regions of the surface become apparent (in this case on the right side of the sample). The tarnish layer is thick enough to obscure the scratches on the sample. At 163 h, the entire Cu surface has been severely tarnished with the very dark material, and the tarnish layer flakes off from the edges, re-exposing some of the underlying metallic substrate.
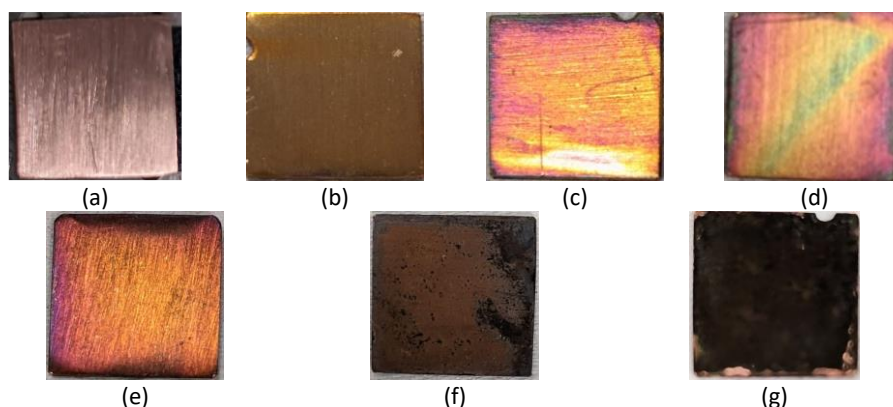
Figure 5.4.1 Images of Cu emerged from HTCBT with 1.0 wt% ZDDP at (a) 0 h (before inserting into the HTCBT vessel), (b) 15 h, (c) 24 h, (d) 40 h, (e) 48 h, (f) 63 h and (g) 165 h.

The HTCBT thus indicates three phases in the Cu corrosion by ZDDP and air. In the first phase, an initial corrosion layer is formed that grows quickly in thickness and covers the whole surface homogeneously by 15 h. In phase two, which appears to be completed by approximately 24 h, this layer is removed, either by dissolution or reaction, re-exposing the metallic Cu. The third phase is the progressive tarnishing of this metallic Cu surface, which

continues until a macroscopically thick black phase has been formed that has sufficient cohesion to delaminate from the edges of the sample. From 63 – 165 h, black particulate was also found in the oil.

5.4.1.1   XPS Elemental Analysis

Table 5.4.1 Elemental analysis (at %) results obtained from quantification of XPS survey spectra of samples exposed to the HTCBT with 1.0 wt% ZDDP for 0 h - 165 h.

Time (h)	Zn $2p_{3/2}$	Cu $2p_{3/2}$	O 1s	C 1s	S 2p	P 2p
0	-	19 ± 1	14 ± 1	67 ± 1	-	-
15	6 ± 1	2 ± 1	20 ± 1	47 ± 1	16 ± 1	11 ± 1
24	4 ± 1	2 ± 1	25 ± 1	42 ± 1	15 ± 1	13 ± 1
40	2 ± 1	2 ± 1	22 ± 1	43 ± 1	16 ± 1	13 ± 1
48	3 ± 1	4 ± 1	33 ± 1	37 ± 1	8 ± 1	16 ± 1
63	0 ± 1	2 ± 1	9 ± 1	84 ± 1	3 ± 1	2 ± 1
165	1 ± 1	2 ± 1	10 ± 1	80 ± 1	3 ± 1	4 ± 1

To determine the surface chemistry associated with phases 1-3 of the tarnishing process, Cu coupons that underwent the modified HTCBT with 1.0 wt% ZDDP for 15 – 165 h were characterised by XPS at the time points corresponding to the photographic images in Figure 5.4.1. The elemental analysis results based on the survey spectra are summarised in Table 5.4.1.
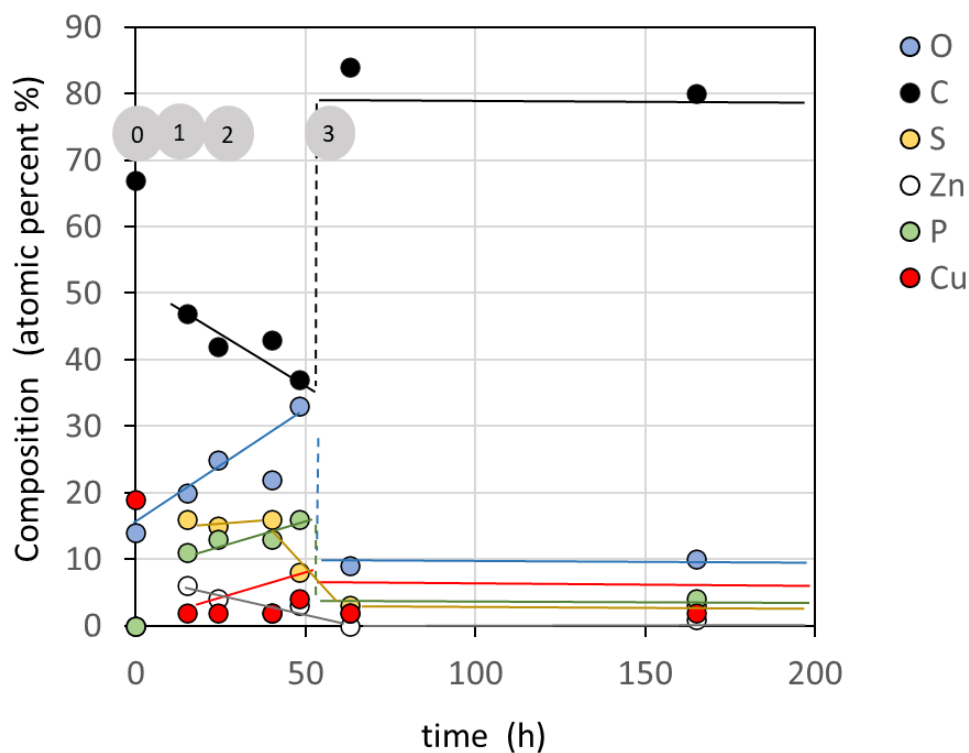
Figure 5.4.2 Quantified elements from Table 5.4.1 plotted against time spent in the HTCBT with 1.0 wt% ZDDP in base oil. The grey circles indicate the phase of corrosion.

Phase 0 – Polished Cu; the surface of Cu is contaminated by C, and O is adsorbed by its exposure to ambient air. The uppermost surface is likely also to have oxidised by exposure to air, contributing to the O 1s signal measured (Figure 5.4.2). In phase 1, an overlayer on the surface of Cu begins to grow, which attenuates the signal arising from the Cu, observed by the sharp drop in Cu 2p signal from phase 0 to phase 1. The Cu signal increases from Cu during phases 1 and 2, which indicates that i) the overlayer decreases in thickness or ii) Cu intercalates into the overlayer formed. Both S and P increase in phases 1 and 2 while Zn decreases. However, there is a noticeable sharp drop in S at the end of phase 2. By phase 3, the elements present from 63 - 168 h are similar, indicating that the corrosion process has finished.

5.4.1.2   XPS Chemical State Analysis: Phase 0
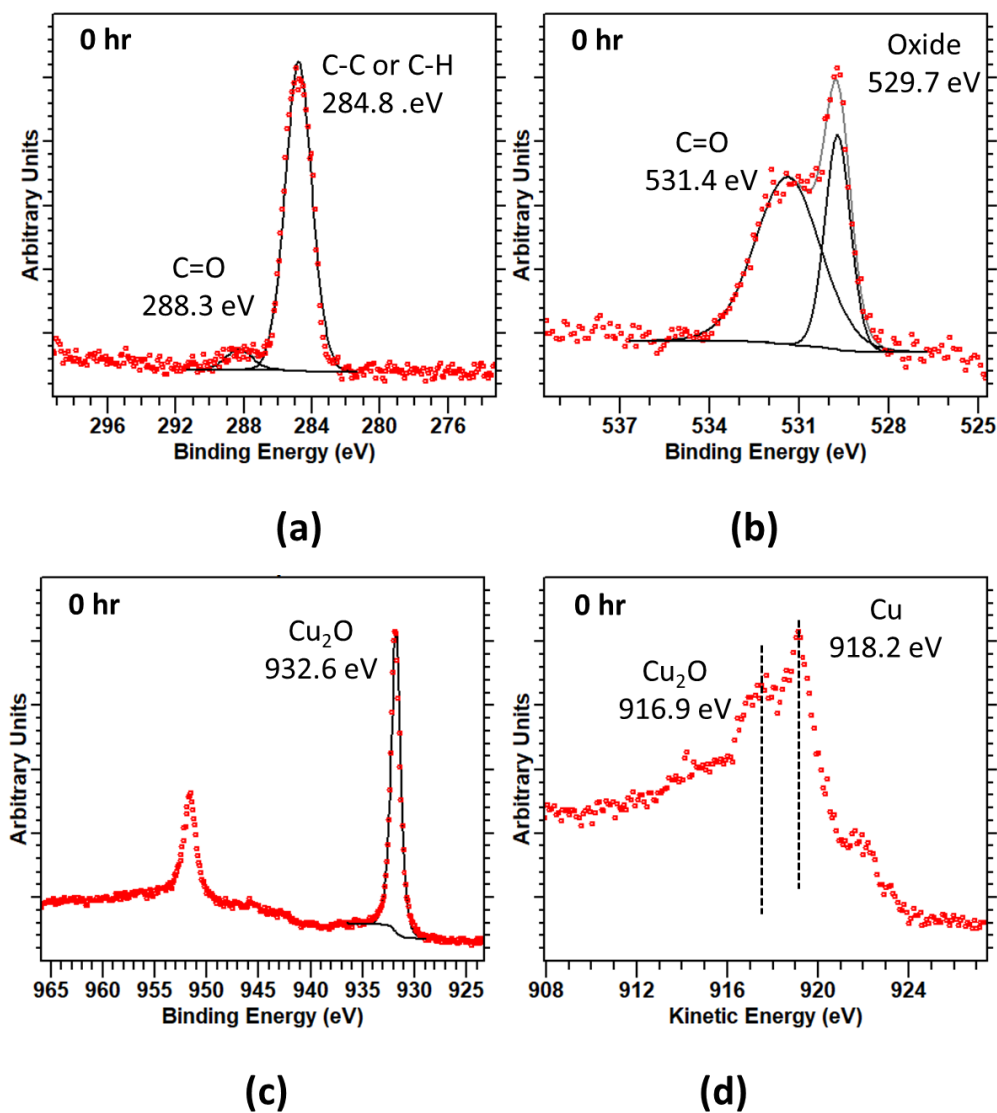
Figure 5.4.3 High-resolution core-level XPS spectra of (a) C 1s, (b) O 1s, (c) Cu 2p, (d) Cu $L_3M_{4,5}M_{4,5}$ of polished Cu (0 h)

The C 1s spectra for polished Cu (Figure 5.4.3a) have two fitted components at binding energies positioned at 284.8 eV and 288.3 eV with FWHM of 1.8 eV. They can be attributed to adventitious carbon from airborne contaminants, aliphatic carbon units (CH_3, CH_2, CH), or ether groups (C=O), respectively. The unsubstituted aliphatic carbon component at 284.8 eV was used to calibrate the binding energy scale of the high-resolution spectra for this sample.

The O 1s spectrum is fitted with two components (Figure 5.4.3b) with binding energy positions centred at 529.7 eV and 531.4 eV with FWHMs 1.1 eV and 2.0 eV, respectively. These chemical environments are attributed to Cu oxide and C=O, respectively.

A single component is fitted for the Cu $2p_{3/2}$ (Figure 5.4.3c) positioned at 932.6 eV with an FWHM of 1.0 eV attributed to Cu metal. The spectrum of Cu $L_3M_{4,5}M_{4,5}$ obtained for polished Cu shows two peaks at 918.2 eV and 916.9 eV corresponding to Cu metal and Cu_2O, respectively. The Cu $L_3M_{4,5}M_{4,5}$ have greater kinetic energy than Cu 2p, and it, therefore, has a greater information depth, being able to probe past the Cu metal and into Cu_2O also. [144,145]

5.4.1.3   *XPS Chemical State Analysis: Phases 1 and 2.*

Table 5.4.2 Elemental analysis (at %) results obtained from quantification of XPS survey spectra of samples exposed to the HTCBT with 1.0 wt% ZDDP for 0 h - 165 h.

Time (h)	Zn $2p_{3/2}$	Cu $2p_{3/2}$	S 2p	P 2p
0	0	100	0	0
15	32	11	84	58
24	21	11	79	68
40	11	11	84	68
48	16	21	42	84
63	0	11	16	11
165	5	11	16	21

The thermal film formed by the ZDDP is expected to form pad-like structures with thicknesses in the order of hundreds of nanometers. [121,133,134] Evidence of a thick thermal film is more apparent when the C 1s and O 1s are excluded from the quantification (Table 5.4.2). A sharp decrease of Cu was measured on the surface at 0 h to 15 h from 100 % to 11% where Cu photoelectrons are attenuated by the overlayers composed of Zn, P and S.

The C 1s spectra (Figure 5.4.4a) have three fitted components at binding energies at 284.8 eV, 286.3 eV, and 287.3 eV, with comparable FWHMs of 1.4–1.5 eV. They can be attributed to carbon chemical states in unsubstituted aliphatic carbon units (CH_3, CH_2, CH), in alcoholic (C-OH) and in ketonic or aldehydic carbonyl units (C=O), respectively. The unsubstituted aliphatic carbon component at 284.8 eV was used to calibrate the binding energy scale of the high-resolution spectra for each sample.

Figure 5.4.4 Normalised, high-resolution core-level XPS spectra of (a) C 1s, (b) Zn 2p, (c) Cu 2p, (d) O 1s, (e) S 2p and (f) C 2s, P 2p and Zn 3s emersed from the HTCBT at 15 h to 48 h, with 1.0 wt % ZDDP in the base oil.

A component is fitted to the Zn $2p_{3/2}$ spectra (Figure 5.4.4b) with binding energies of 1022.3 eV (FWHM = 1.5 -1.6 eV) attributed to Zn thiophosphate found for samples 15 - 48 h. In addition, a second component is fitted for the 48 h sample at 1024.7 eV. This is attributed to Zn thiophosphates that are differentially charged.

The Cu photoelectric peaks detected here are not of the substrate, as the expected thickness of the thermal film is greater than the probing depth of XPS. The Cu detected here must be Cu intercalating into the thermal film. For samples, $15 - 48$ h, a component is fitted to the Cu $2p_{3/2}$ spectra (Figure 5.4.4c) with binding energies of $932.7 - 932.8$ eV (FWHM = 1.4 eV) attributed to Cu thiophosphate.

15 - 48 h O 1s spectra are fitted with two components (Figure 5.4.4d) with binding energy position centred at 531.4- 531.6 eV and 533.0- 533.3 eV with FWHM = 1.6 – 1.8 eV. These chemical environments are attributed to bridging and non-bridging oxygen (BO and NBO), respectively. These are similar to the binding energy reported in similar studies of ZDDP tribofilms.[146] This component corresponds to the differentially charged zinc thiophosphate precipitate. A third component for the 48 h samples is fitted with position 535.2 eV with FWHM = 1.8 eV. This peak has a similar binding energy position to adsorbed water reported in the literature.[147]

S $2p_{3/2}$ and $2p_{1/2}$ doublet sets are fitted to the S 2p spectra e. At $15 - 48$ h, the fitted $2p_{3/2}$ has a binding energy of 162.4 -162.6 eV (FWHM =1.4 – 1.6 eV) attributed to thiophosphate.

P $2p_{3/2}$ and $2p_{1/2}$ doublet sets are fitted to the P 2p spectra Figure 5.4.4 f. At $15 - 48$ h, the fitted $2p_{3/2}$ has a binding energy of 133.4 -133.7 eV (FWHM = 1.4 – 1.7 eV) attributed to thiophosphates. In addition, a second doublet was fitted for the 48 h sample with a P $2p_{3/2}$ positioned at 136.5 eV. This is attributed to Zn thiophosphates that are differentially charged.

It is worth noting that the differentially charged thiophosphate components for Zn 2p and P 2p have similar binding energy shifts. This is expected with differential charging as the photoelectrons experience the same Coulomb force from the charged region.

Figure 5.4.5 Normalised, high-resolution core-level XPS spectra of (a) C 1s, (b) Cu 2p, (c) P 2p and Cu 3s, (d) Zn 2p, (e) S 2p and (f) Cu $L_3M_{4,5}M_{4,5}$ emersed from the HTCBT at 63 h and 165 h, with 1.0 wt % ZDDP in the base oil.

The spectra shown in Figure 5.4.5a have three fitted components with binding energy positioned at 284.8 eV and 286.3 eV (FWHM = 1.2 eV), attributed to C-C or C-H (aliphatic carbon) and C-OH, respectively. In the same fashion as before, the aliphatic carbon photoemission peak at 284.8 eV energy calibrates each spectrum.

A component is fitted to the Zn $2p_{3/2}$ spectra (Figure 5.4.5d) with binding energies of 1023.4 - 1023.9 eV (FWHM = 2.5 eV) attributed to differentially charged Zn thiophosphate.

Two P $2p_{3/2}$ and $2p_{1/2}$ doublets are fitted to the P 2p spectra Figure 5.4.5c. The doublet with P $2p_{3/2}$ binding energy of 133.3 -133.5 eV (FWHM =1.3-1.7 eV) is attributed to Zn thiophosphates corresponding to the Zn 2p peaks observed in Figure 5.4.5 d. A second doublet component is fitted with P $2p_{3/2}$ centred at 135.0 eV (FWHM =1.3) and 135.5 eV (FWHM = 1.7 eV) for the 135 h sample and 165 h sample, respectively. These peaks are attributed to P_2O_5. However, the P_2O_5 on the 165 h sample exhibited differential charging.

Two components are fitted to the Cu 2p spectra Figure 5.4.5 b. A component is fitted to each Cu $2p_{3/2}$ spectra (Figure 5.4.5 b) with binding energies of 932.5 eV (FWHM = 1–4 - 1.5 eV) and 935–2 - 935.3 eV (FWHM = 1.8 – 2.0 eV) attributed to Cu_2S and $CuSO_4$.

Figure 5.4.5 f shows the Cu $L_3M_{4,5}M_{4,5}$ Auger spectra with a peak position at 917.4 - 917.5 eV attributed to Cu_2S.

S $2p_{3/2}$ and $2p_{1/2}$ doublets are fitted to the S 2p spectra Figure 5.4.5 e. The fitted $2p_{3/2}$ has a binding energy of 162.4 -162.6 eV (FWHM =1.2 eV) attributed to sulphides (S^{-2}) thiophosphate structure. A second doublet set is fitted at higher binding energy with the S $2p_{3/2}$ centred at 168.2 eV attributed to $CuSO_4$. These binding energies (and kinetic energy) are similar to previously reported values of $CuSO_4$.[75]

5.4.2 Modified HTCBT with 0.1 wt% ZDDP

Cu samples were prepared using the modified HTCBT method with 0.1 wt% ZDDP in base oil, similar to the experiments detailed previously, where Cu coupons were emersed from the solutions at 24 h, 48 h, 72 h, 138 h and 168 h. Images of the samples taken right after emersion

from the solution are shown in Figure 5.4.6. Samples immersed in the HTCBT from 24 – 72 h show no signs of tarnish, similar to the appearance of the polished Cu coupons shown in Figure 5.4.6a. At 138 h, a dark brown tarnish layer covers the surface with more severe tarnishing on the edges. On the central region of this sample, the tarnishing is not so strong as to obscure the surface roughness created by the SiC grit in the preparation of the coupons prior to the HTCBT. However, the tarnishing does obscure the surface roughness closer to the edges. Lastly, at 168 h, the tarnish covers the surface homogenously with notably darker tarnish than the one observed on the 138 h sample.
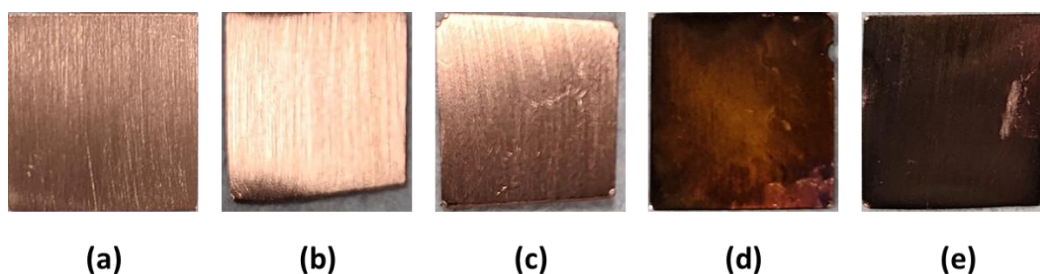
Figure 5.4.6 Images of Cu emerged from HTCBT with 0.1 wt% ZDDP at (a) 24 h, (b) 48 h, (c) 72 h, (d) 138 h and (e) 168 h.

The sample was characterised using XPS. Samples that were emersed from the HTBT with 0.1 wt% at 138 h and 168 h have a very high carbon and oxygen concentration on the surface, attenuating photoemission signals from other elements (Figure 5.4.7). Comparing the survey spectra of the two samples, the C 1s O 1s and C KLL peaks are present on the surface. However, for the 138 h sample, the O KLL peak is present, which is not present in the 168 h sample. The O KLL peak has less kinetic energy than the O 1s, thereby being more surface sensitive. The absence of the O KLL peak on the 168 h sample indicates that a pure carbon overlayer is formed on the surface, attenuating the O KLL signal below.
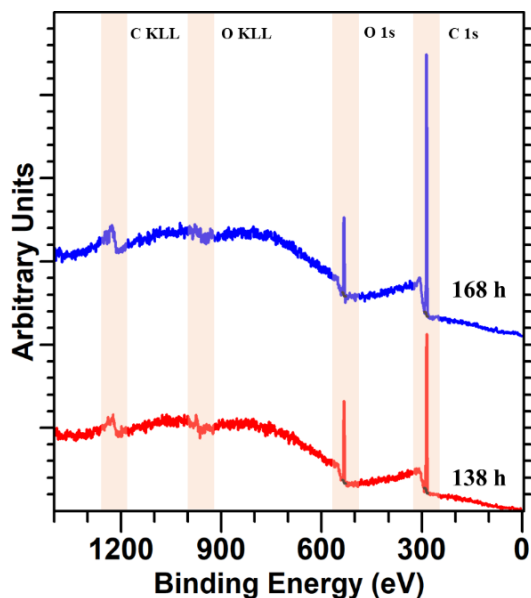
Figure 5.4.7 Survey spectra of the 135 h and 168 h samples highlighting the positions of the C KLL, O KLL, O 1s and C 1s.

These two samples were Ar^+ sputtered, with an emission current of 7 µA and accelerated by 1000 V until a Cu 2p signal was observed on the survey spectra to investigate the Cu/Tarnish interface. This required 2 min of sputtering for the 138 h samples and 4 min for the 168 h sample. The quantification of the survey spectra is displayed in Table 5.4.3.

Table 5.4.3 Elemental analysis (mol%) results obtained from quantification of XPS survey spectra of samples exposed to the HTCBT with 0.1 wt% ZDDP for 24 h - 168 h.

Time (h)	Zn $2p_{3/2}$	Cu $2p_{3/2}$	O 1s	C 1s	S 2p	P 2p
24	8 ± 1	5 ± 1	33 ± 1	47 ± 1	2 ± 1	5 ± 1
48	10 ± 1	4 ± 1	36 ± 1	40 ± 1	5 ± 1	4 ± 1
72	9 ± 1	2 ± 1	34 ± 1	40 ± 1	6 ± 1	9 ± 1
138	0 ± 1	2 ± 1	16 ± 1	80 ± 1	0 ± 1	2 ± 1
168	0 ± 1	0 ± 1	8 ± 1	91 ± 1	0 ± 1	0 ± 1
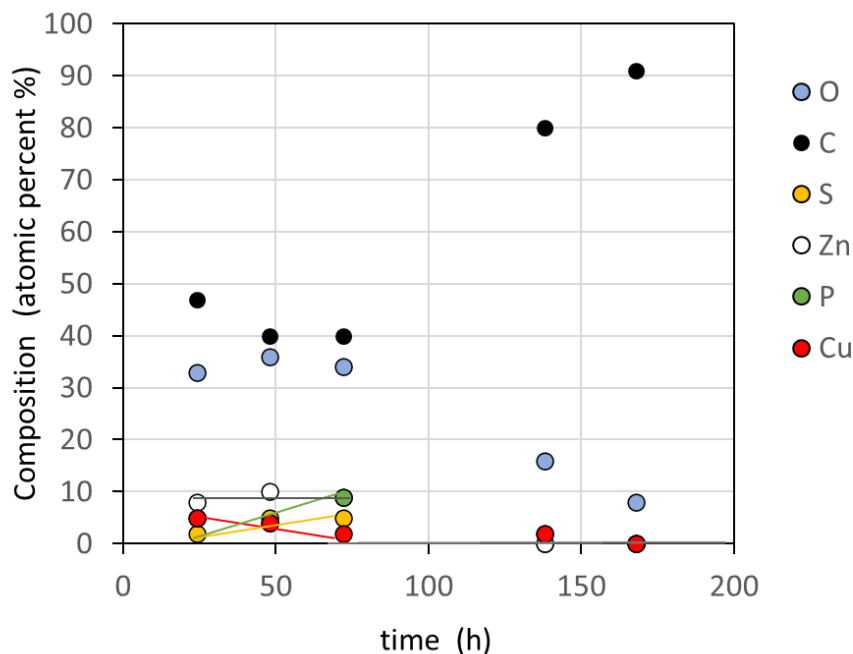
Figure 5.4.8 Quantified elements from Table 5.4.3 plotted against time spent in the HTCBT with 0.1 wt% ZDDP in base oil.

HTCBT with 1.0 wt% ZDDP shows an increase of S and P as a function of time from 15 – 48 h. Here, a similar trend is observed with S and P also increasing from 24 -72 h. However, unlike the HTCBT with 1.0 wt% ZDDP experiments, the level of Zn remains unchanged, and a decrease of Cu is observed as a function of time.

The surface of the samples emersed for 138 and 168 h were composed of C and O without photoemission signals from other elements (Figure 5.4.7) prior to sputtering. These samples were sputtered with Ar$^+$ until a Cu 2p signal was observed. The 168 samples required a longer etching time (4 min) to observe a Cu 2p signal than the 135 h sample (2 min). This implies that the hydrocarbon overlayer is much thicker for the 168 h sample. After sputtering, the surface shows an increase in C and a decrease in O and Cu from 135 h to 168 h. P is present on the 135 h sample but not in the 168 h sample.
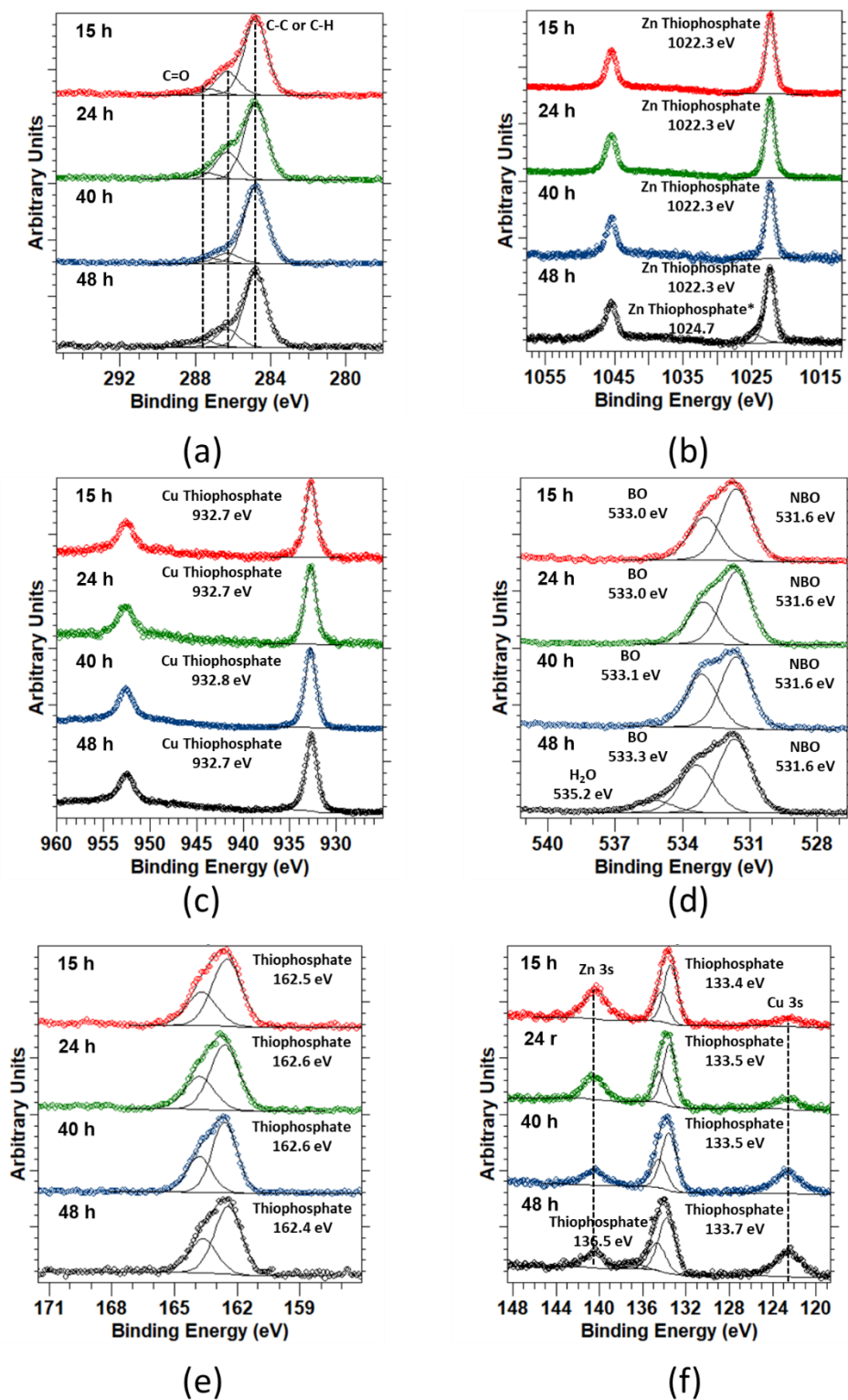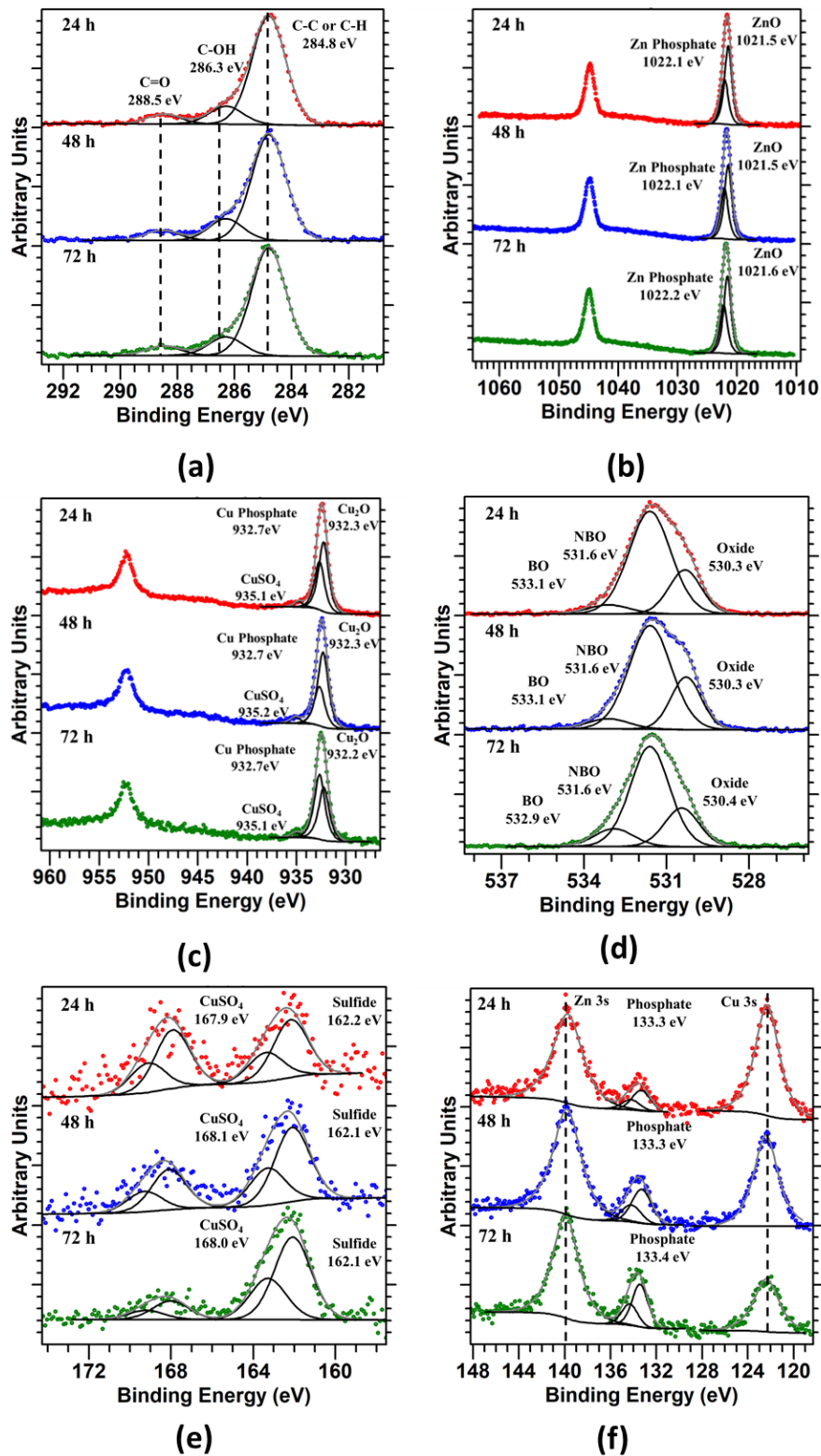
Figure 5.4.9 Normalised, high-resolution core-level XPS spectra of (a) C 1s, (b) Zn 2p, (c) Cu 2p, (d) O 1s, (e) S 2p and (f) Zn 3s, P 2p and Cu 3s, emersed from the HTCBT at 24 – 72 h, with 0.1 wt % ZDDP in the base oil.

Two components are fitted to the Zn $2p_{3/2}$ spectra (Figure 5.4.9b) with binding energies of 1021.5 -1021.6 eV (FWHM = 1.5) and 1022.1 -1022.2 eV (FWHM = 1.5) attributed to ZnO and Phosphate respectively found on samples 24 -72 h.

Similarly, for samples 24 – 72, three component is fitted to the Cu $2p_{3/2}$ spectra (Figure 5.4.9c) with binding energies of 932.2 - 932.3 eV(FWHM = 1.2 eV), 932.7 – 932.8 eV (FWHM = 1.1 – 1.2 eV) and 935.1 - 935.2 eV (FWHM = 1.2 eV) attributed to Cu_2O, Cu phosphate and $CuSO_4$.

The 24 - 72 h O 1s spectra are fitted with three components (Figure 5.4.9d) with binding energy position centred at 530.3 - 530.3 eV (FWHM = 1.3 – 1.5 eV), 531.6 eV and 532.9- 533.1 eV (FWHM = 1.7 – 1.8 eV). These chemical environments are attributed to oxides BO and NBO, respectively.

Two S $2p_{3/2}$ and $2p_{1/2}$ doublets are fitted to the S 2p spectra Figure 5.4.9 e. At 24 – 72 h, the fitted $2p_{3/2}$ has a binding energy of 162.2 -162.2 eV (FWHM =2.0 2.1 eV) and 167.0 -168.1 eV (FWHM =2.0 – 2.1 eV) attributed to sulphide (S^{-2}) in the phosphate structure and $CuSO_4$ respectively.

P $2p_{3/2}$ and $2p_{1/2}$ doublet sets are fitted to the P 2p spectra Figure 5.4.9f. At 24 – 72 h, the fitted $2p_{3/2}$ has a binding energy of 133.3 -133.4 eV (FWHM = 1.7 – 2.0 eV) attributed to phosphates.
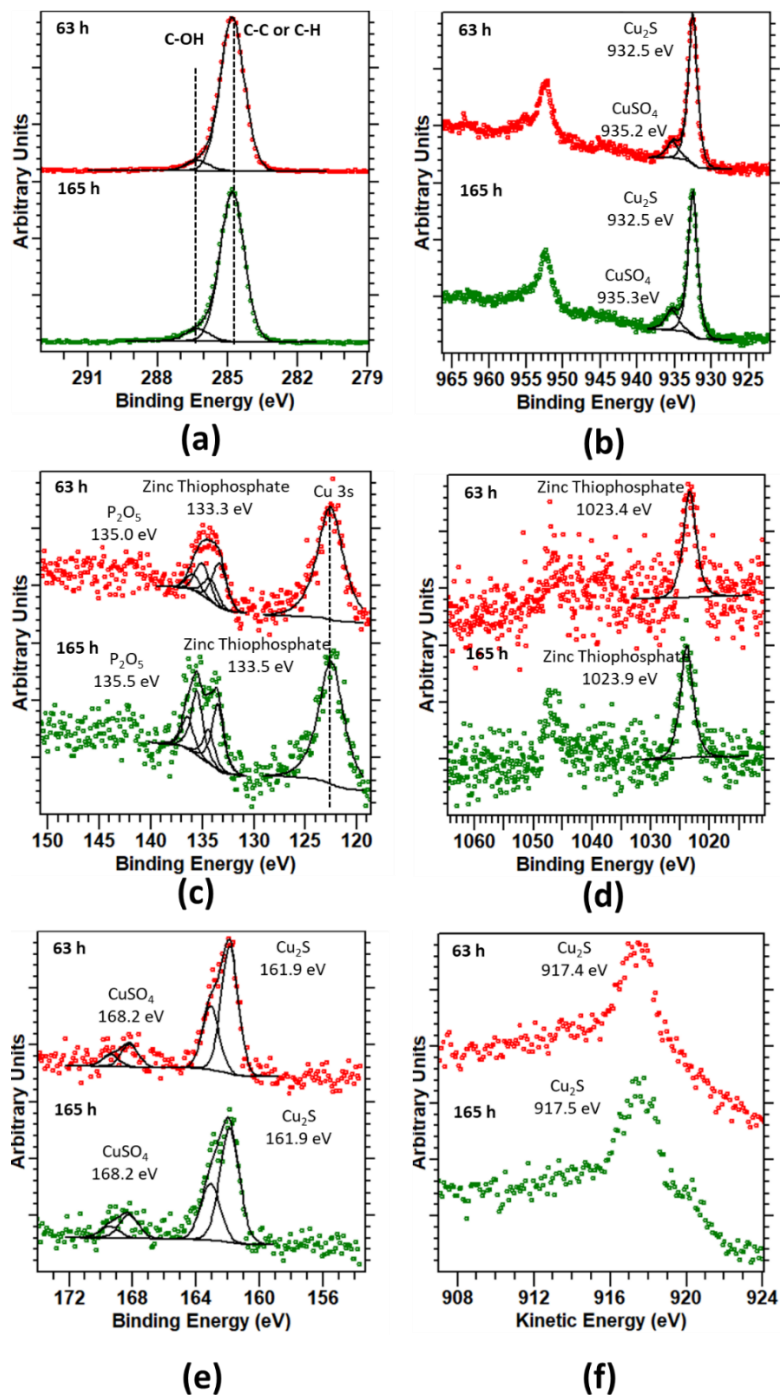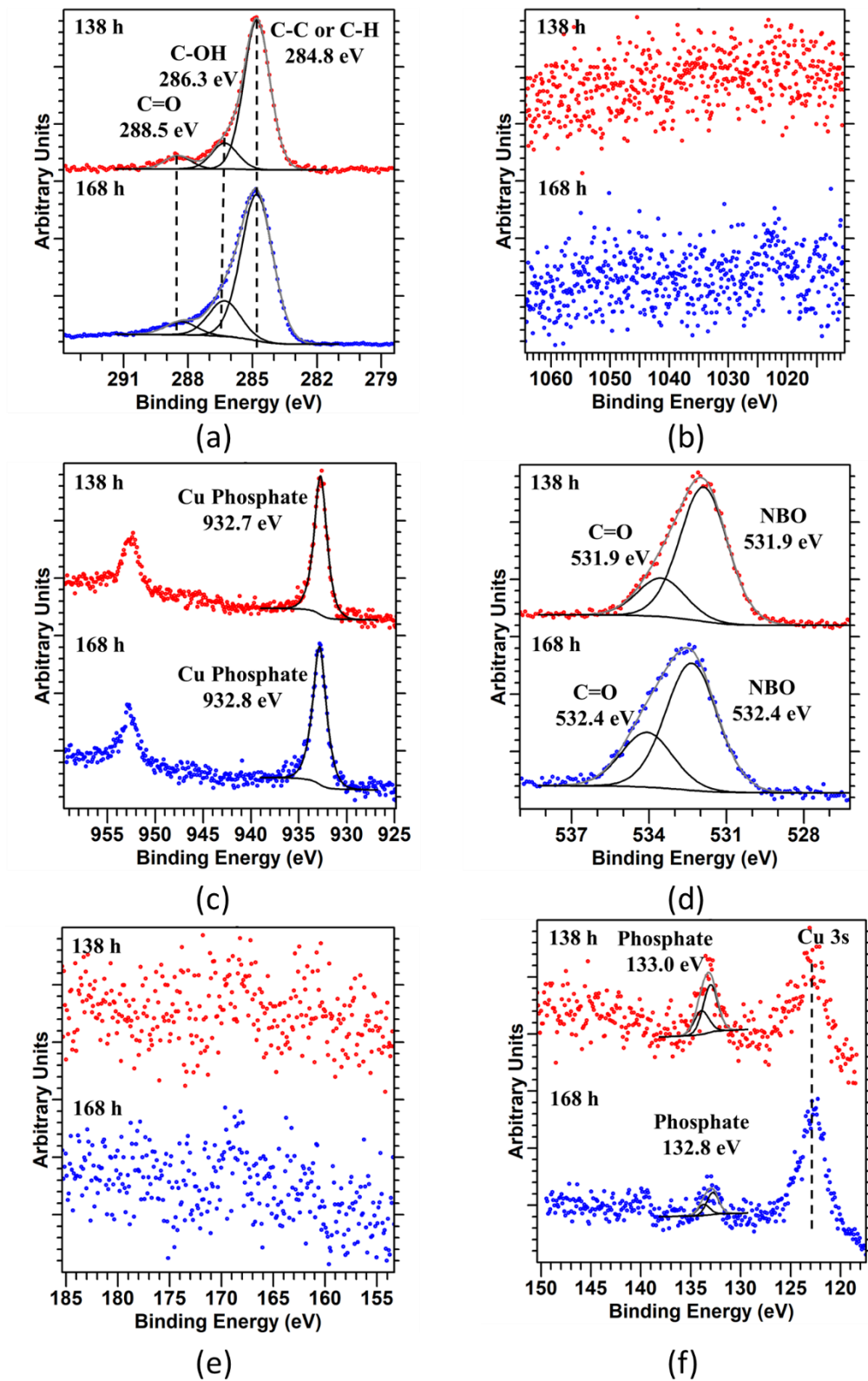
Figure 5.4.10 Normalised, high-resolution core-level XPS spectra of (a) C 1s, (b) Zn 2p, (c) Cu 2p, (d) O 1s, (e) S 2p and (f) Zn 3s, P2p and Cu 3s, emersed from the HTCBT at 138 – 168 h, with 0.1 wt % ZDDP in the base oil.

No Zn 2p and S 2p are detected on the 138 h and 168 h samples in b and d.

Similarly, for samples 138 – 168 h, a component is fitted to the Cu $2p_{3/2}$ spectra (Figure 5.4.10c) with binding energies of 932.7 – 932.8 eV (FWHM = 1.5 - 1.7 eV) attributed to Cu phosphate.

138 -168 h O 1s spectra are fitted with two components (Figure 5.4.10d) with binding energy position centred at 531.9- 532.4 eV and 533.0- 533.3 eV with FWHM = 1.6 – 1.8 eV. These chemical environments are attributed to NBO and C=O, respectively.

There were small quantifiable signals from the P 2p for the 138 h and 168 h samples. P $2p_{3/2}$ and $2p_{1/2}$ doublet are fitted to the P 2p spectra Figure 5.4.9f. At 135 – 168 h, the fitted $2p_{3/2}$ has a binding energy of 132.3 eV (FWHM = 1.7 eV) attributed to phosphates.

5.4.3 Depth profiling

Depth profiling measurements were done with samples emersed in the HTCBT with 0.1 wt% ZDDP for 72 h. Ar^+ sputtering was done with an acceleration potential of 750 V and 7 µA.

Table 5.4.4 Atomic percentage (at%) results obtained from quantification of XPS survey spectra of samples exposed to the HTCBT with 0.1 wt% ZDDP for 72 h etched by Ar^+ accelerated by 750 V and charge output of 7 µA.

Etch time, t_{etch} (min)	Zn $2p_{3/2}$	Cu $2p_{3/2}$	O 1s	C 1s	S 2p	P 2p
0	10 ± 1	3 ± 1	36 ± 1	41 ± 1	4 ± 1	8 ± 1
2	17 ± 1	6 ± 1	36 ± 1	21 ± 1	5 ± 1	14 ± 1
4	21 ± 1	9 ± 1	40 ± 1	16 ± 1	7 ± 1	8 ± 1
6	24 ± 1	11 ± 1	41 ± 1	12 ± 1	6 ± 1	4 ± 1
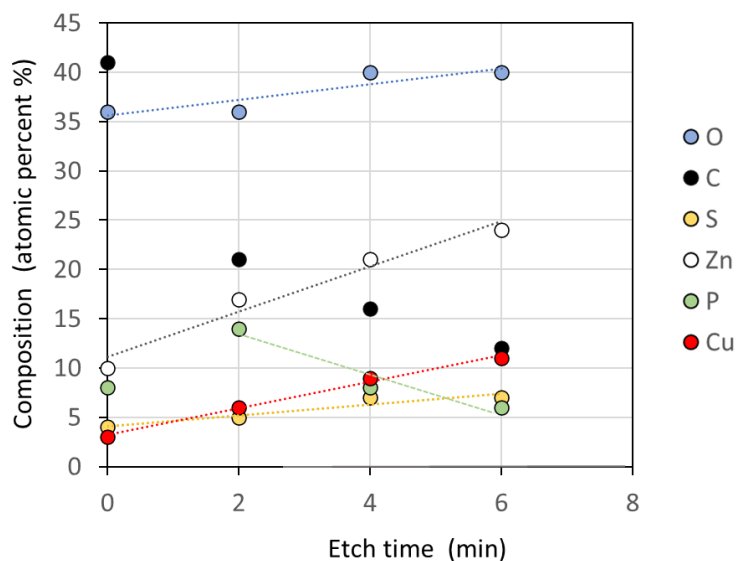
Figure 5.4.11 Quantified elements from Table 5.4.4 plotted against time spent in the HTCBT with 0.1 wt% ZDDP in base oil.

Etching removes material on the surface and creates an etch crater. The depth of the etch crater can not be defined without topographic measurements such as atomic force microscopy (AFM). The lack of this measurement limits our ability to determine the depth subsequent to etching. However, assuming that the etch time, t_{etch}, is proportional to the depth of the etching crater, it becomes possible to gain insight into the chemical depth profile of the thermal film.

As a function of t_{etch}, C decreases from $t_{etch}= 0$- 6 min with the largest decrease from $t_{etch} = 0$ to 2 min. An increase in O, Zn, Cu and S is observed. For P, there is an initial increase at $t_{etch}= 0$ to 2 min followed by a decrease at $t_{etch}= 2$ to 6 min.
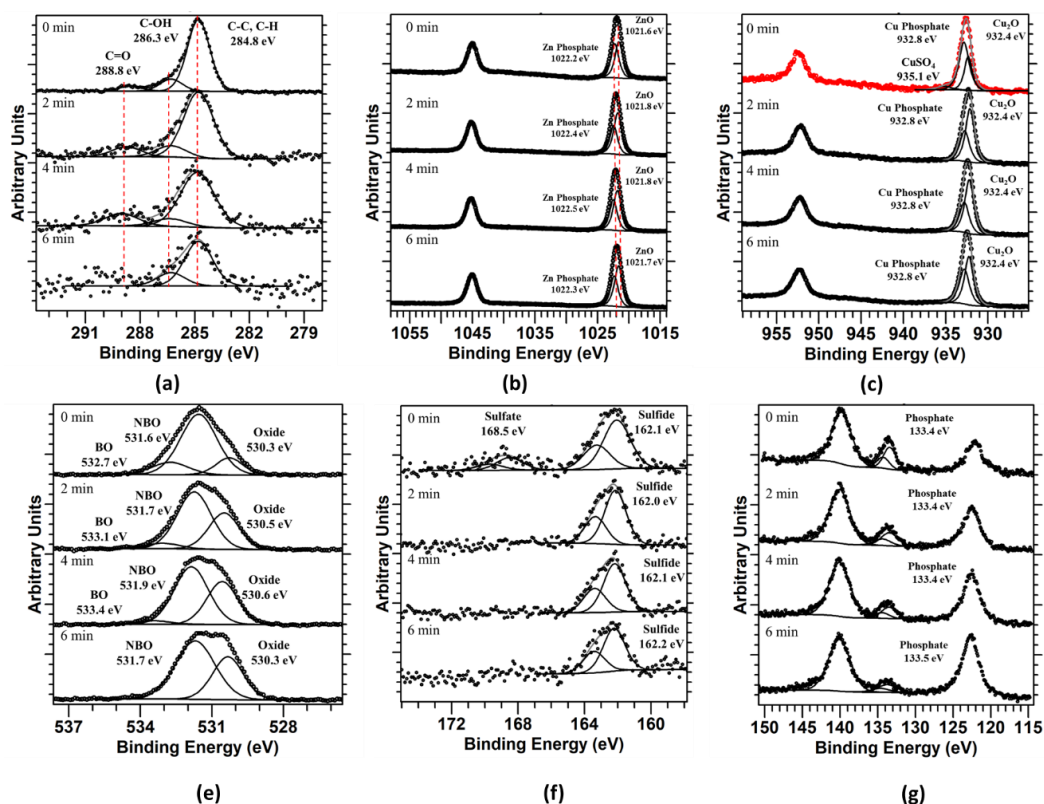
Figure 5.4.12 Normalised, high-resolution core-level XPS spectra of (a) C 1s, (b) Zn 2p, (c) Cu 2p, (d) O 1s, (e) S 2p and (f) Zn 3s, P2p and Cu 3s, emersed from the HTCBT at 72 h, with 0.1 wt % ZDDP in the base oil etched by an Ar$^+$ accelerated by at 750 V and 7μA output.

Two components are fitted to the Zn 2p$_{3/2}$ spectra (Figure 5.4.12b) with binding energies of 1021.6 -1021.7 eV (FWHM = 1.5) and 1022.2 -1022.4 eV (FWHM = 1.4 -1.5) attributed to ZnO and Phosphate.

Similarly, two components are fitted to the Cu 2p$_{3/2}$ spectra (Figure 5.4.12**c**) with binding energies of 932.2 - 932.3 eV(FWHM = 1.3 - 1.4 eV) and 932.7 – 932.8 eV (FWHM = 1.3 – 1.4 eV) and attributed to Cu$_2$O and Cu phosphate. A third component was fitted to the spectra prior to etching (t$_{etch}$ = 0 min) 935.2 eV with an FWHM = 2.0 eV.

The O 1s spectra are fitted with three components (Figure 5.4.12d) with binding energy position centred at 530.3 - 530.6 eV (FWHM = 1.6 – 1.9 eV), 531.6 eV and 532.7- 533.4 eV (FWHM = 1.7 – 1.8 eV). These chemical environments are attributed to oxides, BO and NBO, respectively.

A single S $2p_{3/2}$ and $2p_{1/2}$ doublet is fitted to the S 2p spectra Figure 5.4.12f. The fitted $2p_{3/2}$ component has a binding energy of 162.0 -162.2 eV (FWHM = 1.5 – 1.8 eV) attributed to sulphides (S^{-2}). A second doublet was fitted to the spectra prior to etching (t_{etch} = 0 min) with 168.5 eV (FWHM =2.0 – 2.1 eV) in the phosphate structure and $CuSO_4$, respectively.

P $2p_{3/2}$ and $2p_{1/2}$ doublet sets are fitted to the P 2p spectra Figure 5.4.12g. The fitted $2p_{3/2}$ component has a binding energy of 133.3 -133.5 eV (FWHM = 2.0 – 2.6 eV) attributed to phosphates.

5.5 Discussion

5.5.1 HTCBT with 1.0 wt%
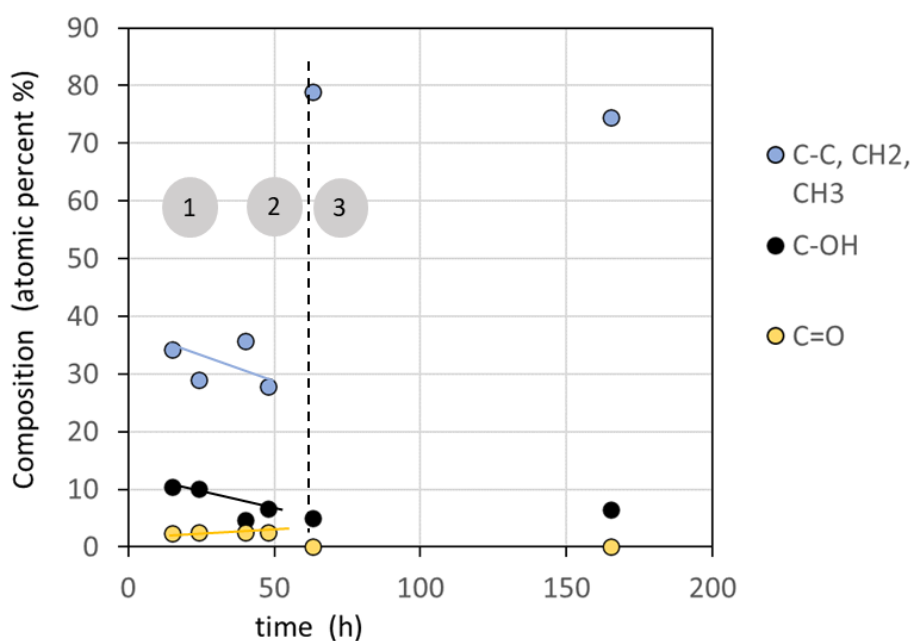
Figure 5.5.1 Intensities of the carbon environments shown in Figure 5.4.5a and Figure 5.4.6a plotted as a function of time.

In phase 1 and 2, aliphatic carbon (C-C, CH_2, CH_3) and the alcohol group (C-OH) decreases in overall intensity. (Figure 5.5.1). The carbonyl (C=O) environment, however, increases

gradually. This suggests that oil is becoming increasingly oxidised in the free radical chain. In phase 3, the carbonyl group is not detected, while the alcohol group remains the same.

Fundamental studies of zinc phosphates (and similar systems) using XPS have identified a protocol for calculating the phosphate chain length. The chain length can be calculated by fitting the O 1s spectra with bridging oxygen (BO) and non-binding bridging oxygen (NBO) components and using the BO/NBO ratio to calculate the thiophosphate chain length.[148–150] The O 1s (Figure 5.4.3d) spectra show BO: NBO ratios are constant from 15 h to 48 h, indicating the chain length remains constant. The thermal film ZDDP forms thiophosphates, where oxygen atoms in the phosphate groups are substituted with sulphur atoms (decreasing the NBO contribution). Therefore, the BO: NBO does not follow the expected stoichiometry and cannot determine the exact chain length directly.

Table 5.5.1 Calculated values for $(Cu^{2+} + Zn^{2+})$/P using quantification of Zn and Cu $2p_{3/2}$ and the corresponding thiophosphate chain present for samples emersed in the HTCBT with 1.0 wt% ZDDP at 24 – 48 h.

Time (h)	$(Cu^{2+} + Zn^{2+})$/P	Thiophosphate chain
15	0.7	Polythiophosphate
24	0.5	Metathiophosphate
40	0.5	Metathiophosphate
48	0.4	Metathiophosphate

Alternatively, it is possible to calculate the chain length using the Zn:P ratio directly. For zinc orthophosphates, the Zn/P = 3/2, zinc pyrophosphate Zn/P = 1, zinc metaphosphates are Zn/P = 0.5, and zinc polyphosphate Zn/P = 0.67. These ratios are equally valid for the thiophosphate analogue.[148] Zn/P decreases as the chain length increases. The Zn/P decreases as a function of time and can be directly observed in Figure 5.4.3f. However, in the thermal film formed by ZDDP, it has been reported that an ion exchange occurs in the tribofilm between Zn^{2+} and the metal ions from the substrate.[6] Dithiophosphate has been previously used as a metal extractor

and has a greater affinity to Cu^{2+} than Zn^{2+}.[6,136] Using this method, Cu^{2+} in the film must also be considered when identifying the chain length. The quantification shows that polythiophosphates are present at 15 h, metathiosphosphate at 24 h, 40 h and 48 h (Table 5.5.1).

The chain length is calculated using the Zn and Cu $2p_{3/2}$, which are more surface sensitive than the Zn and Cu 3s. Another trend is observed when the phosphate chain length is calculated using the quantified Zn and Cu 3s photoemission peaks. The quantification shows that thiophosphates are present at 15 h, metathiosphophate at 24 h, meta - and polythiophosphate mixture at 40 h and polythiophosphate at 48 h. The kinetic energy of the Zn and Cu 3s peaks are similar to that of the P 2p, producing a more accurate result.

Table 5.5.2 Calculated values for $(Cu^{2+} + Zn^{2+})$/P using quantification of Zn and Cu 3s and the corresponding thiophosphate chain present for samples emersed in the HTCBT with 1.0 wt% ZDDP at 24 – 48 h.

Time (h)	$(Cu^{2+} + Zn^{2+})$/P	Thiophosphate chain
15	0.72 ± 0.14	Polythiophosphate
24	0.46 ± 0.11	Metathiophosphate
40	0.61 ± 0.12	Meta - and polythiophosphate mixture
48	0.73 ± 0.11	Polythiophosphate

The thermal film is expected to form pad-like structures with thicknesses of ~100 nm, thereby the substrate is outside the probing depth of XPS. [121,133,134] The Cu/thermal film interface is, therefore, out of the information depth XPS. As the substrate is the only source of Cu in the system, a higher Cu concentration is expected closer to the substrate. A diagram of the proposed structure of the thermal film formed on the Cu surface is shown in Figure 5.5.2.
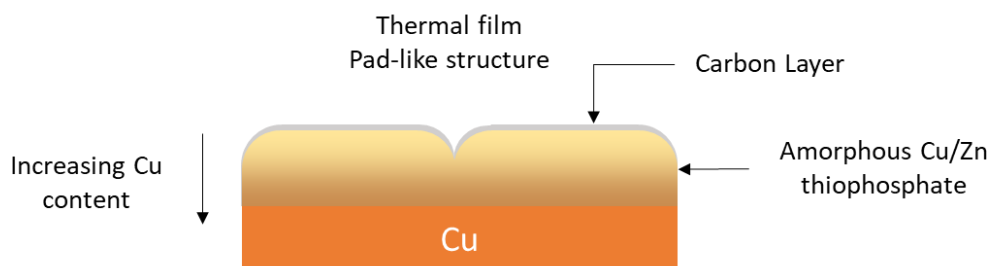
Figure 5.5.2 Schematic diagram of the thermal film formed on Cu by ZDDP.

No literature has been found addressing the characterisation of Cu thiophosphate by XPS (or otherwise), so comparing the binding energy positions is not possible. XPS has previously characterised various Cu compounds by Moretti 1995 and has since been reproduced by Biesinger.[70,75] Plotting the Cu $2p_{3/2}$ (the sharpest photoemission peak) binding energy position against the kinetic energy position of Cu $L_3M_{4,5}M_{4,5}$ (the sharpest Auger peak) results from these studies show two trends. First, Cu^{2+} compounds have binding energy larger than 933.0 eV and are found to follow a -1 gradient. For Cu^+, the binding energy is less than 932.6 eV and follows a gradient of -3.[75] No compounds reported in these studies have Cu $2p_{3/2}$ binding energy positions between 932.6 - 933.0 eV, where the Cu $2p_{3/2}$ Cu thiophosphate photoemission peaks are observed for this system (Figure 5.4.4c). It must be considered, however, that the study only considered powdered crystalline material. The binding energy could change for amorphous material due to the contribution of the Madelung potential and extra atomic relaxation energy. Furthermore, though there are acceptations, Cu^{2+} compounds have a strong satellite feature in the 2p spectra. These satellite features are sensitive to structure and may not appear for non-crystalline material, such as nanoparticles and amorphous material like the thermal film. [151]

Table 5.4.1 shows that the S:P remains relatively constant from 15 to 40 h at approximately 1:1. However, at 48 h, the amount of S quantified has significantly reduced, and the O has increased. This could signify a reaction of the thermal film with peroxides forming in the

solution. The oxidation of base oil follows a free radical chain reaction. The reactions that initiate the free radical chains are thermally activated (and can be further aided with a metal catalyst such as a multivalent Cu). [42] ZDDP can act as antioxidants which retards the oxidation process. Additionally, ZDDP has an affinity to Cu ions in the solution where ligan substitutions can occur, preventing these multivalent ions from catalysing the reducing free radical chain oxidation. [6,136] The free radical chain reaction accelerates as the additive depletes in the solution. The reaction of the thermal film with peroxyl radicals cleaves the P-S bond and produces P-O bonds. This is a similar reaction to the preparation of the ZDDP. [152] The change in the coordination structure would explain the binding energy shift observed in Figure 5.4.4f for the 48 h sample.

Additional peaks are observed on Zn 2p and P 2p spectra of the 48 h sample. The small peak in the P 2p with the P $2p_{3/2}$ positioned 136.7 eV (Figure 5.4.4f) is attributed to the zinc phosphate particulates that are differentially charged. The corresponding Zn $2p_{3/2}$ was also found at a binding energy position of 1024.5 eV (Figure 5.4.4b). The literature has reported that ZDDP forms 'ashes', zinc thiophosphate precipitating from the solution. [49] A carbon based (hydrocarbon) overlayer sits above the thermal film - electrically isolating the precipitate, leading to differential charging and, hence the change in the measured binding energy.

The measured spectra of the 63 h sample show a Cu_2S surface (Figure 5.4.5b). $CuSO_4$ is also found on the surface, likely from further oxidation of Cu_2S. Similar zinc phosphate and P_2O_5 precipitates are present on the surface that are differentially charging, similar to the observed precipitate in the 48h sample. The spectra obtained for the 165 samples also is very similar to the ones obtained for the 63 h sample, indicating that no other reactions are occurring.

5.5.2 Proposed Mechanism- 1.0 wt% ZDDP

The time-resolved XPS measurements show that a thermal film is formed on the surface of the Cu coupon. The thermal film is initially composed of zinc thiophosphate. However, Cu^{2+} ions are intercalating into the thermal film via an ion exchange with Zn^{2+}. The Cu^{2+} content of the thermal film increases as a function of time. Quantifying the phosphate chain length from the cation: phosphorus ($Zn^{2+} + Cu^{2+}$: P) ratio shows that the chain length initially decreased from

a polythiophosphate to a metathiophosphate (from 15h to 24 h) before increasing chain length again to the polyphosphates. The ion exchange observed here is the first instance of corrosion.

ZDDP quenches the oxidation of the oil via a radical chain reaction. The depletion of the ZDDP allows the chain reaction to go forward. A product of the free chain radical reaction is a peroxy radical. The reaction of peroxy radical with thiophosphate leads to the cleaving of the S-P bond, reducing the sulphur content and increasing the oxygen content. This is observed in the 48 h sample. It is reported that the adhesion of the thermal film to the substrate is through the S atoms.[6] The reduction of sulphur leads to the exfoliation of the thermal film from the surface. However, more evidence is required to support this hypothesis.

Thiols produced in the degradation of ZDDP in solution could readily react with the surface of the exposed Cu surface to produce Cu_2S - forming the final product of corrosion. The proposed mechanism is shown in Figure 5.5.3.
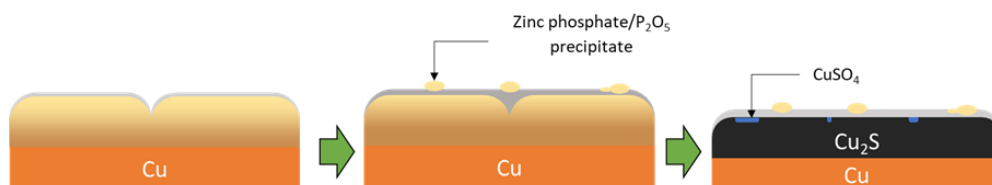
Figure 5.5.3 Diagram of proposed mechanisms leading to the corrosion of the Cu surface.

5.5.3 HTCBT with 0.1 wt%

Comparing images of the samples that were emersed from the HTCBT at 15 h - 48 h with 1.0 wt% ZDDP (Figure 5.4.1b, c and e respectively) versus samples emersed 24 h – 72 h 0.1 wt % ZDDP (Figure 5.4.6 a-c respectively), it can be deduced that the overlayers formed with a 1.0 wt % ZDDP are significantly thicker as the overlayer are not visible for the 0.1 wt% samples. The tarnish formed in the HTCBT with 0.1 wt % ZDDP is a carbon-based overlayer.

Directly below this carbon overlayer is Cu phosphate, with no photoemission signal detected for the Zn and S (Figure 5.4.10c and e).

Table 5.5.3 Elemental analysis (mol%) results obtained from quantification of XPS survey spectra of samples exposed to the HTCBT with 0.1 wt% ZDDP for 24 h - 168 h. Quantified using the Zn and Cu $2p_{3/2}$

Time (h)	O 1s	C 1s	S 2p	Zn 3s	P 2p	Cu 3s
24	26 ± 1	37 ± 1	1 ± 1	16 ± 1	4 ± 1	16 ± 1
48	29 ± 1	32 ± 1	4 ± 1	18 ± 1	3 ± 1	13 ± 1
72	29 ± 1	36 ± 1	5 ± 1	15 ± 1	8 ± 1	7 ± 1
138	16 ± 1	78 ± 1	0 ± 1	0 ± 1	2 ± 1	5 ± 1
168	8 ± 1	90 ± 1	0 ± 1	0 ± 1	0 ± 1	2 ± 1

A phosphate glass overlayer progressively forms on the surface of the coupons as a function of time from 24 h to 72 h. The increase of phosphorus is observed (quantified by the P 2p signal, Figure 5.4.8), as well as the decrease of the Cu 3s signal (Figure 5.4.9). As the phosphate overlayer increases in thickness, the photoelectrons from the Cu are progressively attenuated.

As discussed previously, the BO: NBO cannot directly determine the phosphate chain length in the thermal film. However, as the phosphates are linked via an oxygen bridge, it could be interpreted that the phosphate chain length increases as the BO intensity in the O 1s spectra (Figure 5.4.9d) increases.

Similar to the previous analysis method diccused in section 5.5.1, the $Cu^{2+} + Zn^{2+}/P$ indicates the thiophosphate chain length. When calculated, this provides stronger evidence for the increase in thiophosphate chain length (Table 5.5.3). The ratio produced unexpectedly large

values (figures significantly above expected values). The Zn and Cu 3s photoemission peaks have a higher kinetic energy, compared to the Zn and Cu 2p, and are able to probe deeper into the sample. As the thermal film is significantly thinner than the one observed with the 1.0 wt% concentration, other species, such as oxides, may lay under the thiophosphate layer and contribute to the 3s signal, arriving at large values for $Cu^{2+} + Zn^{2+}/P$. Instead, to calculate these values, the Zn and Cu $2p_{3/2}$ peaks are used (Table 5.5.3) and the component intensity (area) in Figure 5.4.9. The calculated ratios are summarised in Table 5.5.4. This shows that the thiophosphate chain is increasing in length.

Table 5.5.4 Calculated values for $(Cu^{2+} + Zn^{2+})/P$ and the corresponding thiophosphate chain present for samples that emerged in the HTCBT with 0.1 wt% ZDDP at 24 – 72 h.

Time (h)	$(Cu^{2+} + Zn^{2+})/P$	thiophosphate chain
24	1.5	Ortho-thiophosphate
48	1.3	Pyro – and Ortho – thiophosphate mixture
72	0.5	Meta-thiophosphate

The binding energies detected for the Zn and Cu phosphates component in the Cu and Zn $2p_{3/2}$ (Figure 5.4.9 b and c) are similar to those found in the samples that emerged with 1.0 wt% ZDDP (Figure 5.4.4 b and c). However, the binding energies for the P 2p attributed to phosphates (Figure 5.4.9f) are shifted by 0.1-0.4 eV towards lower binding energy relative to the binding energy observed for the samples emerged in the HTCBT with 1.0 wt% ZDDP (Figure 5.4.4f). Similarly, the sulphides measured in the samples that emerged from 0.1 wt% samples shifted binding energies by 0.5 - 0.3 eV towards the lower binding energy. The FWHM for the S and P measured from the samples that emerged from HTCBT with 0.1 wt% ZDDP are also larger by up to 0.4 - 0.7 eV. The larger FWHM could indicate a local molecular

disorder that would also contribute to the observed shift in the S 2p and P 2p spectra via a polarisation energy change.

Finally, the samples from the HTCBT with 0.1 wt% ZDDP from 24 -72 h also detected $CuSO_4$ on the surface (Figure 5.4.9e). The sulphate/sulphide photoemission ratios decrease as a function of time. The S p, however, increases 24 -72 h (Table 5.4.3). The absolute quantity of $CuSO_4$, therefore, remains constant.

From 138 -168 h, a hydrocarbon-based overlayer forms on the surface (Figure 5.4.7). The formation of this overlayer is due to the polymerisation of aliphatic carbon (termination reaction discussed in section 2.2.1). The free radical chain reaction may be catalysed locally on the Cu surface, accelerating termination reactions locally. Directly below this carbon-based layer, Cu phosphate is detected with no signal photoemission peaks detected for Zn and S (Figure 5.4.9). Similar to the discussion in 5.5.1, this is due to a ligand substitution between Zn^{2+} and Cu^{2+} in the phosphate glass overlayer. In this instance, the Zn^{2+} has been completely substituted by Cu^{2+}. A sharp reduction of S on the surface was observed in Figure 3.2 before the Cu surface formed a Cu_2S tarnish. The reduction of S from the surface could be due to reactions with alkyl peroxy radicals in the oil, similar to the discussion in section 5.5.2. however, the surface remains protected from thiols by the hydrocarbon overlayer, preventing the formation of Cu_2S.

5.5.4 Depth profiling

Etching was done to investigate the structure of the overlayer formed on the Cu surface. Etching was conducted by sputtering, where the sample's surface is bombarded with Ar^+ ions, removing some surface material and exposing the material underneath.[79]

The C 1s signal reduced from 41% to 12 % over $t_{etch} = 0 - 6$ min, with the first etch cycle removing the majority of the carbon. At $t_{etch} = 2$ min, there is a significant increase of other elements Zn, Cu, P, and S (Table 5.4.1). This indicates that the initial etch cycle removed a carbon-based overlayer, which attenuated the photoemission signal from the elements below itself.

Subsequent etching cycles (t_{etch} = 2 - 6 min) measure a P decrease (Table 5.4.4). As discussed, the BO: NBO cannot directly determine the phosphate chain length in the thermal film. However, as the phosphates are linked via an oxygen bridge, it could be deduced that the BO intensity in the O 1s spectra is closely linked to the degree of polymerisation. A reduction in the BO intensity is observed from t_{etch} = 2 - 6 min (Figure 5.4.12e), indicating that the phosphate chain length is decreasing.

Similar to the analysis performed in sections 5.5.1 and 5.5.3, the $Cu^{2+}+Zn^{2+}$/P ratio was calculated from each etch cycle shown in Table 5.5.5. The calculated ratios show that the phosphate chain length decreases as a function of t_{etch}. Assuming t_{etch} is proportional to depth, the phosphate chain length decreases as a function of depth.

Table 5.5.5 Calculated values for ($Cu^{2+} + Zn^{2+}$)/P and the corresponding thiophosphate chian present for the sample emerged in the HTCBT with 0.1 wt% ZDDP at 72 h etched from t_{etch} = 0 -6 min using at Ar^+ beam.

Etch time, t_{etch} (min)	($Cu^{2+} + Zn^{2+}$)/P	Thiophosphate chain
0	0.7	Polythiophosphate
2	0.6	Meta - and polythiophosphate mixture
4	1.5	Orthothiphoshate
6	2.7	-

In addition, the atomic per cent of Zn and Cu thiophosphate and oxide were calculated using the component areas shown in Figure 5.4.12 and the quantification of photoemission peaks summaries in Table 5.4.1. These values are shown in Table 5.5.6, along with the Zn/Cu present as thiophosphates and oxides. These calculated values show increases in Zn and Cu oxide and thiophosphate as a function of t_{etch}. The Zn/Cu values for the oxide show an increasingly larger portion of Cu oxide as a function of t_{etch}. In contrast, the ratio of Zn/Cu for thiophosphate

shows that the mixture of Zn^{2+} and Cu^{2+} in the thiophosphate thermal remains relatively constant. From section 5.5.2, it was discussed that the Cu^{2+} is intercalating into the thiophosphate thermal layer via a cation exchange with Zn^{2+}, thereby it is expected that there are greater Cu^{2+} closer to the substrate, i.e. a Zn/Cu phosphate of descending values as a function of t_{etch}. [135,136]

There are gradual increases in the oxide component observed in the O 1s spectra as a function of t_{etch}/depth (Figure 5.4.12e). This increase in this component suggests that there is an oxide layer that is positioned below the thiophosphate film. As the sample is etched, gradually removing the thiophosphate film, the oxide layer becomes less attenuated. Both decreases in the phosphate chain length and increases in the oxide components as a function of depth are aligned with the discussion in section 5.5.3, where the phosphate glass overlayer grows (increases in thickness) as a function of time and with the phosphate chain increasing in length.

Table 5.5.6 Quantified Zn and Cu thiophosphate and oxide in the thermal film per etch cycle, calculated form component area ratios shown in Figure 5.4.12 and quantified atomic ratio % shown in Table 5.4.4

Etch time, t_{etch} (min)	At%						Zn: Cu ratio	
	Thiophosphate			Oxide			Thiophosphate	Oxide
	Zn	Cu	Cu + Zn	Zn	Cu	Cu + Zn	Zn/Cu	Zn/Cu
0	4.3	1.8	6.1	5.7	1.2	6.9	2.4	4.6
2	6.6	2.3	8.9	10.4	3.7	14.1	2.9	2.8
4	8.8	3.3	12.1	12.2	5.7	17.9	2.6	2.2
6	13.1	5.0	18.1	10.9	6.0	16.9	2.6	1.8

There is a gradual increase in the amount of S found in the thermal film as a function of t_{etch}. The increase of S as a function of etch time is in agreement with thiophosphate glass film formed on Fe or steel surfaces.[6]
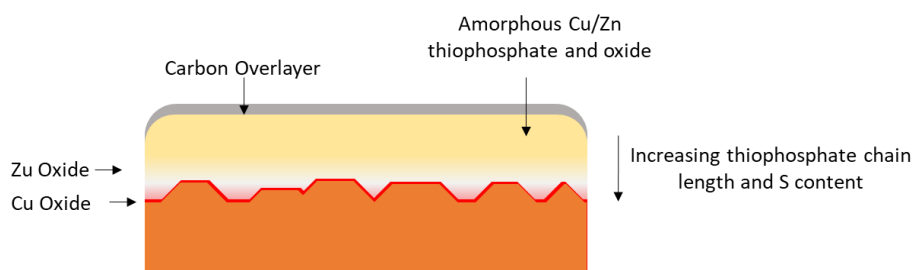
Figure 5.5.4 Diagram of the proposed profile of the thermal film as a result of depth profiling.

The trends observed from depth profiling are similar to those in the literature. An aliphatic carbon-based overlayer forms on the surface, a phosphate glass overlayer with decreasing phosphate chain length as a function of depth and an increase in sulphur content as a function of depth (Figure 5.5.4).[6] However, here we find Cu_2O and ZnO intercalated in the thermal film which is not reported in the literature.

5.6 Conclusions

This study has investigated the interaction of ZDDP and Cu and the chemical transformation leading to corrosion. Ex situ samples were prepared under HTCBT. The time-resolved ex situ measurements of Cu coupons treated with ZDDP provided insights into the interfacial reaction of Cu with ZDDP, leading to a better understanding of corrosion processes. XPS was employed to study the surface chemistry, and using a homogeneous sample as a starting point offered experimental advantages.

Experiments were conducted under HTCBT conditions with two concentrations, 1.0 wt% and 0.1 wt%. The resulting composition of the thermal film formed on the surface of the substrate differed depending on the concentration used. fu

At 1.0 wt%, the measurements show that the thermal film formed on the Cu surface consisted of Zn thiophosphate initially, but Cu^{2+} ions underwent an ion exchange with Zn^{2+} and became incorporated into the film over time. Quantifying the phosphate chain length based on the nctthiophosphate, followed by an increase in polyphosphates. This ion exchange process represented the initial instance of corrosion. The removal of the thiophosphate overlayer and consequent exposure of the Cu surface allows for the degradation products of ZDDP in the solution, such as thiols, to react, producing Cu_2S and contributing to the corrosion process. More investigations are required to determine how the thermal layer is removed from the surface of Cu.

For experiments conducted with 0.1 wt% ZDDP, it was observed that the thickness of the overlayers formed on the Cu surface was significantly reduced compared to experiments with 1.0 wt% ZDDP. The thermal film formed with this concentration contains Zn and Cu oxides. The phosphate chain length increases as a function of time. The dark tarnish layer on these samples is hydrocarbons. The formation of this tarnish is likely due to the polymerisation of aliphatic carbon from the termination reactions of the free radical chain.

Furthermore, using Ar^+ etching to depth profile the thermal film was conducted. These experiments showed that the thiophosphate chain length decreases as a function of depth. It was also found that there is an increase in S content as a function of depth.

This investigation gave valuable insights into the non-aqueous chemistry of ZDDP on Cu surfaces under HTCBT conditions. The results highlighted the interfacial reactions, ion exchange processes and corrosion mechanisms involved contributing to a better understanding of the behaviour of ZDDP on Cu surfaces.

6 Development of XAS devices for *In Situ* and *Operando* Studies

6.1 Abstract

X-ray absorption spectroscopy (XAS) by gas-flow total-electron-yield (TEY) is a surface sensitive technique (10-200 nm) for analysing the molecular structure and chemical composition of materials. Samples can remain in their native state without any additional preparation or modification allowing flexibility to investigate systems in their natural state. Here, we present the development of two He-flow TEY systems to investigate tribological samples in *operando* and *in situ.*

A novel cell design to investigate the surface chemistry of tribological samples using XAS *in situ*. The cell is designed to measure X-ray diffraction (XRD), fluorescent yield (FY), TEY, and transmission geometry. The TEY measurements provide chemical-sensitive information at the interface between the substrate and the tribofilm, which is critical in understanding the chemical reactions and mechanisms leading to corrosion. However, due to air-contaminated He source, distortion was observed in the TEY spectra obtained for Cu foil.

In addition, the design and integration of a He-flow TEY detector into a tribometer for *operando* and *in situ* studies is described, which enables exploring the more surface sensitive TEY mode of XAS. Fundamental studies of tribofilms formed on sliding surfaces are crucial for developing novel lubrication additives. *In situ* characterisation of tribofilms has previously been done by XAS via FY measurements.[99,141,153] Experiments using this detector, reveal distinct chemical species on the oil surface and in the bulk. This development work was performed in the context of a study examining a possible alternative ZDDP, namely V(IV) oxyacetylacetonate ($VO(acac)_2$). XAS *operando* characterisation of $VO(acac)_2$ enabled the correlation of the additive chemical phases with its tribological performance.

6.2 Introduction

X-ray absorption spectroscopy (XAS) by gas-flow total electron yield (TEY) detection is an affordable and versatile method for a detailed analysis of the molecular structure and chemical composition of materials with high surface sensitivity $(10 - 200$ nm).[103,119,154] As such, it is a powerful method for relating the molecular basis of materials performance across virtually all sectors of societally relevant research, including energy, electronics, environmental, chemical, biological and medical applications. Compared to the XAS transmission and fluorescence-yield (FY) configurations, TEY has the advantage of being suitable for optically dense sample measurements without such complications as thickness, pin-hole, or self-absorption effects. This allows for keeping the samples in their native state without additional preparation and modification, which is a great advantage. TEY also complements more commonly used surface analysis techniques, such as XPS, which are typically employed for studying tribological systems.[121].

The advancements in developing surface-sensitive *in situ* and *operando* techniques are presented in this chapter. The design and commissioning of an XAS *in situ* cell with an integrated TEY detection system specifically designed for multi-modal measurements is discussed. This cell is designed to subject metal samples to HTCBT conditions and characterise the surface properties of the metal in response to operating conditions using the integrated TEY detector.

In addition, a novel TEY detection system is designed and commissioned to facilitate the characterization of additive systems in *operando* conditions. This TEY device is designed to integrate into an existing tribometer, allowing for the real-time evaluation of additives during tribological testing.

6.3 Gas -flow TEY

6.3.1 Auger Signal Formation

An X-ray absorption event generates a photoelectron, leaving behind an excited atom with a core-hole in place of the ejected photoelectron. The excited atom is unstable and decays through a cascade of radiative (fluorescent) or radiationless (Auger decay) electronic transition, generating fluorescent photons and Auger electrons, respectively (Figure 2.3.3). The photoinduced core-hole vacancy passes through occupied atomic shells and multiplies until it reaches the valence band. A hole in the valence band can then be filled with electrons from external sources.[119]

Fluorescent photons and Auger electrons are secondary products of photoabsorption. The number of fluorescent photons or Auger electrons produced in the sample is proportional to the number of photoinduced primary core holes and therefore the X-ray absorption coefficient.[119] The detection of fluorescent photons or Auger electrons as a function of energy produces spectra related to the true X-ray absorption spectrum of the sample (Equation 15).

$$\mu(E) = \frac{I_{TEY}}{I_0}$$

Equation 15

Elastic and inelastic scattering, core vacancy multiplication and re-absorption of fluorescent photons are the main processes underlying the formation of the electron emission spectrum. The primary Auger electrons, emitted in the first step of the radiationless decay, are the most energetic. Auger electrons emitted due to the radiationless decay of the core-hole left behind by the primary Auger electron (and other Auger electrons emitted from subsequent decay) have energy orders of magnitude smaller than the primary Auger electron.[119,154] When probing a transition metal's K-edge, the KLL Auger electrons have the greatest kinetic energy, while LMM and MVV Augers have approximately kinetic energies with one (LMM) and two (MVV) magnitudes lower.[155] These electrons can be further divided into elastic and inelastically scattered contributions. Inelastically scattered Auger electrons collide with atoms and other

electrons prior to ejection from the surface. Inelastically scattered Auger electrons make up the majority of all Auger electrons emitted from the sample surface. Elastic contributions from the sample before loss of kinetic energy due to inelastic collisions. Only electrons emitted close to the surface of the sample contribute to signal.

Photoelectrons also contribute to the detected signal. Fluorescent photons emitted in the radiative decay of primary core holes can produce photoelectrons. As the photoelectrons are produced from weakly bound atomic levels, the energy of these photoelectrons are comparable to the primary Auger electrons. [119]

Virtually any gas can be used in gas-flow TEY.[119] However, some consideration must be taken for optically dense samples. For such samples, the FY signal would bare 'self-absorbtion' distortions. Self-absorption distortions enhance the pre-edge features and dampen post-edge oscillations. These distortions can be observed in the TEY spectra by when fluorescent photons excite secondary electrons in the sample (dicussed above) and the gas phase.[154] These distortions are identified after normalising the spectra to the edge height. To minimise the excitations of the gas phase by flourecent photons, helium (He) is used TEY measumrents, as the absorbtion cross-section is small.[154]

6.3.2 Detection of the Electrons with Gas Ionisation Chambers

An ionisation chamber with an internal photoemitting sample is a direct analogue to gas-flow electron-yield. Energetic Auger/photoelectron electrons from the sample collide with gas atoms/molecules, causing an impact ionisation event. Each ionisation collision between an energetic electron and a gas atom/molecule produces an additional electron and a positive ion. Under a sufficiently strong electric field, the electron-ion pair are accelerated in opposite directions, hindering recombination. This electric field can be provided by placing a counter electrode opposite the sample. The average energy required to create electron-ion pairs loosely depends on the incident electron energy and varies little between gas species. Typical values are approximately 30 ± 15 eV. For He, the energy lost by the incident electron to create an electron-ion pair is ~42 eV.[156,157]

Ion chambers can be operated in several regimes depending on the potential difference applied and the pressure of the filling gas. Where the applied potential difference is 50 - 200 V, so-called the current regime, the chamber has a linear response to the emitted electrons. This potential difference range is below the threshold at which additional charges due to field-induced pair formation are formed.[119] Operating in this potential difference range, the integrated electron/ion current formed can be measured i.e. measures the charge amplified TEY signal. The signal strength is independent of the detector voltage such that gas amplification of the TEY signal results from the excess kinetic energy carried by the electrons when they are emitted from the sample. [119]

Gas amplification weights the information in the TEY towards the more energetic contributions. Primary Auger electrons, produced in the initial step of the radiationless core-hole decay, also contain most of the kinetic energy emitted from the sample, are the most energetic and therefore dominate the measured signal. Secondary, tertiary and higher-order Auger contributions have kinetic energies which are, respectively, one, two and more orders of magnitude lower than that of the primary Auger contributions and are therefore much less amplified. Furthermore, most of the electrons that are emitted from the surface undergo inelastic scattering. It is specifically inelastic primary Auger electrons that dominate the current measured in gas-flow TEY. [119]

In gas-flow TEY cells a counter electrode is mounted ≥1 cm away from the sample. The counter electrode can be connected to a current preamplifier. The current associated with gas-flow TEY measurements are in the nanoamp range and so the amplifier must be capable of handling so the preamplifier must be capable of handling input current variations in the picoampere range. Similarly, the sample surface can also be connected to an amplifier where an equivalent current can also be collected. With a positively biased counter electrode attracting background electrons, measuring the current from the sample's surface produces spectra with lower noise. Figure 6.3.1 shows a gas-flow TEY experiment, where the current from both the counter electrode and the sample is measured. Measurement of the current from the sample and counter electrode simultaneously would produce an identical spectrum. Differences between the two spectra could help to identify instrumental problems.[119]

gas-filled cell with X-ray window

MCS channel 2

MCS channel 1

> ± 60 V

collector plate

e⁻/ion current ≈ 10^{-9} A

sample plate

X-rays
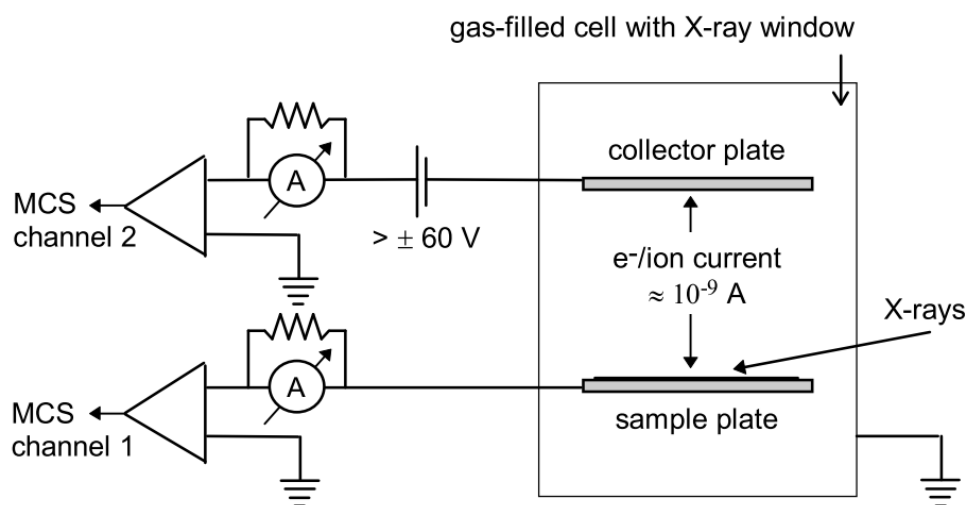
Figure 6.3.1 Schematic setup of a gas flow TEY experiment.[119]

6.4 XAS Cell for In Situ Studies of Metal Corrosion under Conditions of the ASTM High-Temperature Corrosion Bench Test

Engine bearings are crucial components in transmitting load between the crankshaft and the piston, converting reciprocating motion to circular motion. However, these bearings must exhibit low friction and have high resistance to wear and corrosion. This requires materials with sufficient hardness and elastic deformability, such as copper (Cu).[3] Failure to prevent corrosion of such engine bearings can reduce engine lifetime and lead to engine failure.

The ASTM D6594, commonly referred to as the high temperature corrosion bench test (HTCBT), is a commonly used laboratory test to determine the affinity of a lubricant formulation to corrode soft metals such as Cu.[7] In the HTCBT, Cu is exposed to an aerated lubricant formulation at a temperature of 135°C to qualitatively determine the extent of

120

corrosion. In addition, the degree of metal tarnishing is visually evaluated to monitor the extent of corrosion. However, the HTCBT specification does not proceed to perform a chemical analysis of the metal surfaces and the corrosion films. Identifying the chemical phases at the interface between the lubricant and metal would be advantageous for understanding the corrosion mechanism.

A corrosion cell was developed to investigate inhomogeneous corrosion on soft metal surfaces. The design follows the ASTM D6964 or high-temperature corrosion bench test (HTCBT) corrosion condition, with a Cu coupon submerged in oil at 135°C with 5 dm^3/hr airflow through the liquid phase. The cell design was made with the aim of achieving simultaneous XAS monitoring in transmission, FY, and TEY modes. Additionally, FY measurements of the liquid phase provide insight into the chemical transformation of the additive.

For this application, borosilicate (glass) was indicated as a suitable material due to its chemical inertness and high-temperature resistance. A 100 ml Duran glass bottle was modified by adding X-ray transparent (Kapton) windows. A 150° Kapton window can accommodate FY, transmission, and transmission XRD (Figure 6.4.1).

A Viton gasket was placed over the glass cut-outs to create a gas-tight seal, and Kapton windows were added directly over the gasket. Loctite SI5358 sealant was used to ensure that the cell was leak-tight. This sealant is chemically resistant and withstands temperatures up to 250°C.

Two 6 mm glass inlet/outlet was modified into the glass bottle to insert gasses and liquids. The inlets of the cell are attached to Viton soft tubing, connected to Swagelok bellow-sealed valves (**SS-6H-MM)** at the other end.

PTFE has been identified as a suitable material for this application due to its chemical stability at high temperatures of up to 250°C and chemical resistance. These properties make PTFE an ideal material for various cell components to ensure it does not interfere with the studied chemical reactions.
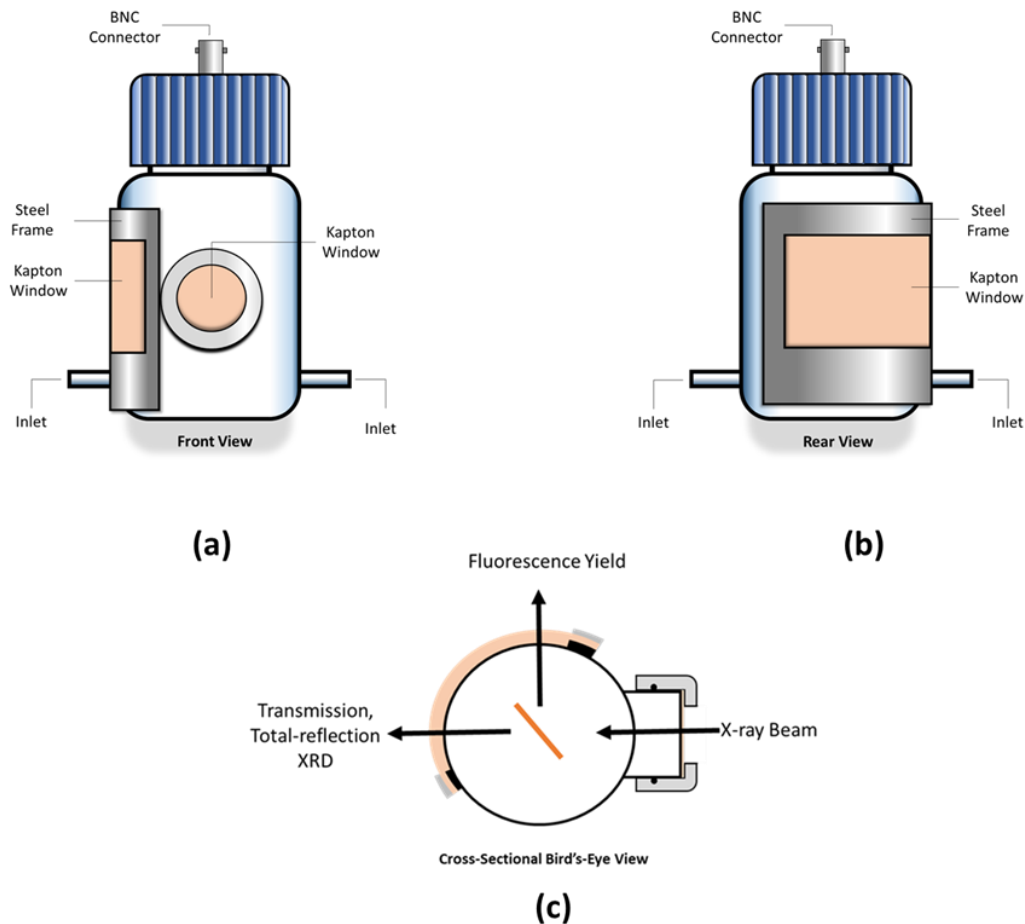
Figure 6.4.1 (a & b) illustrates the cell's exterior and (c) a cross-sectional bird's eye view of the cell demonstrating the X-ray geometry for the various detection modes.

This cell can characterise various types of samples, including coupons and foils. A custom holder was developed to characterise foils while maintaining their tensioning during the corrosion processes. Foil samples are placed between two PTFE frames, as shown in Figure 6.4.2a. The design of the frames includes a lowered edge to allow the foil surfaces to be flush with the frame, which is beneficial for detecting fluorescent photons with shallow exit angles. Two PTFE clamps on either side secure the frames together (Figure 6.4.2b.) The frame is then inserted into a PTFE chuck and is secured by a grub screw (Figure 6.4.2c). Coupons, on the other hand, can be directly inserted into the chuck.
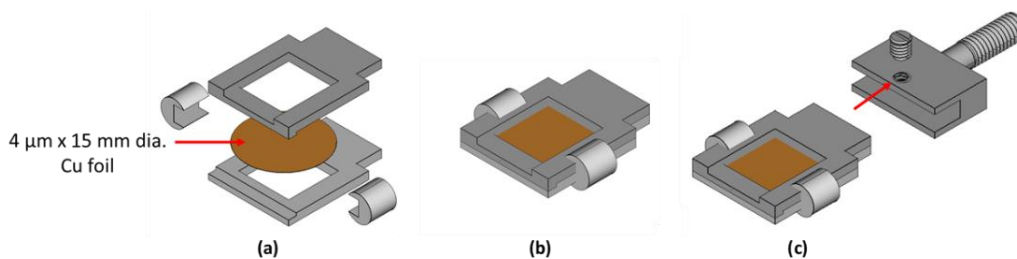
Figure 6.4.2 CAD renders of a Cu foil secured onto PTFE frames.

The sample chuck is securely fastened to the main adjustable PTFE support assembly inside the cell by an M4 PTFE hex nut, as shown in Figure 6.4.3. A stainless-steel plate (measuring 15 mm x 10 mm) is positioned at a few mm distance above the sample, acting as the counter-electrode for TEY measurements (Figure 6.4.3). Similar to the sample, the stainless-steel plate is secured to the internal PTFE sample support. The design of this support system allows for adjustment of the distance between the sample and the stainless-steel plate. In addition, the incident X-ray angle can be adjusted by rotating the chucks about their respective axes. The main sample support is suspended from the bottle cap, which also houses a gas outlet and two BNC connectors, as depicted in Figure 6.4.3. During the chemical treatment, the gas outlet remains open to prevent the cell from becoming over-pressurised while it is closed during the total-electron yield measurement.

The stainless steel TEY counter-electrode plate is connected to a female BNC connector via a Kapton-insulated coaxially shielded wire. The stainless-steel plate acts as the counter electrode in the TEY circuit, which collects gas phase charges induced by pair formation through energetic electrons emitted from the sample. The coaxial wire provides electromagnetic shielding to reduce noise on the signal. A second female BNC connector is electrically connected to the sample surface via a gold wire. Gold is a good conductor and chemically inert to the investigated chemistry.
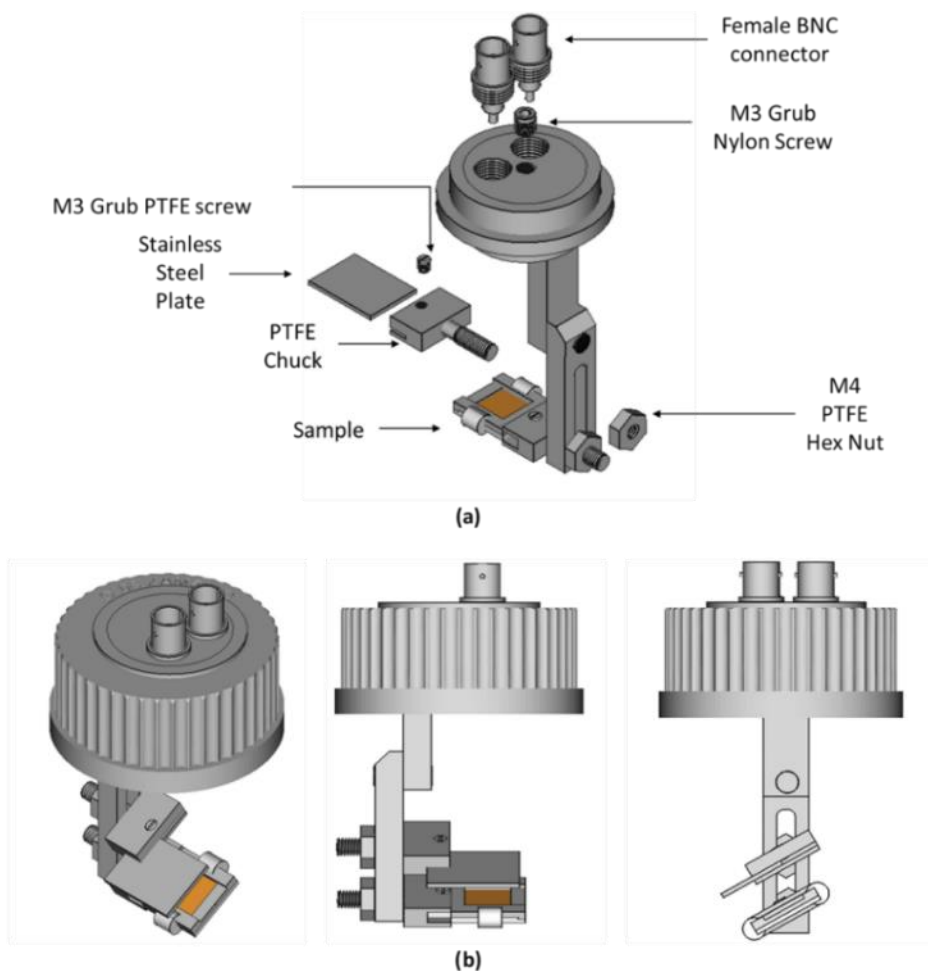
Figure 6.4.3 CAD renders of custom PTFE parts manufactured for this cell (b) shows various views of all the parts assembled.

The counter electrode is connected to the positive terminal of a direct current (DC) power supply via the BNC connector. The surface of the sample is connected to the signal amplifier. The signal amplifier grounds the sample by default. The amplifier also transfers the analogue signal to the beamlines data acquisition channel (Figure 6.4.4). The BNC cables attached to the cells' internal TEY circuitry are shielded with aluminium foil to minimise noise arising from vibrations. Loose wires vibrating in the Earth's magnetic field can produce significant noise on the data produced. The currents produced by vibrations can exceed the pico- to nano ampere currents produced in He-flow TEY.
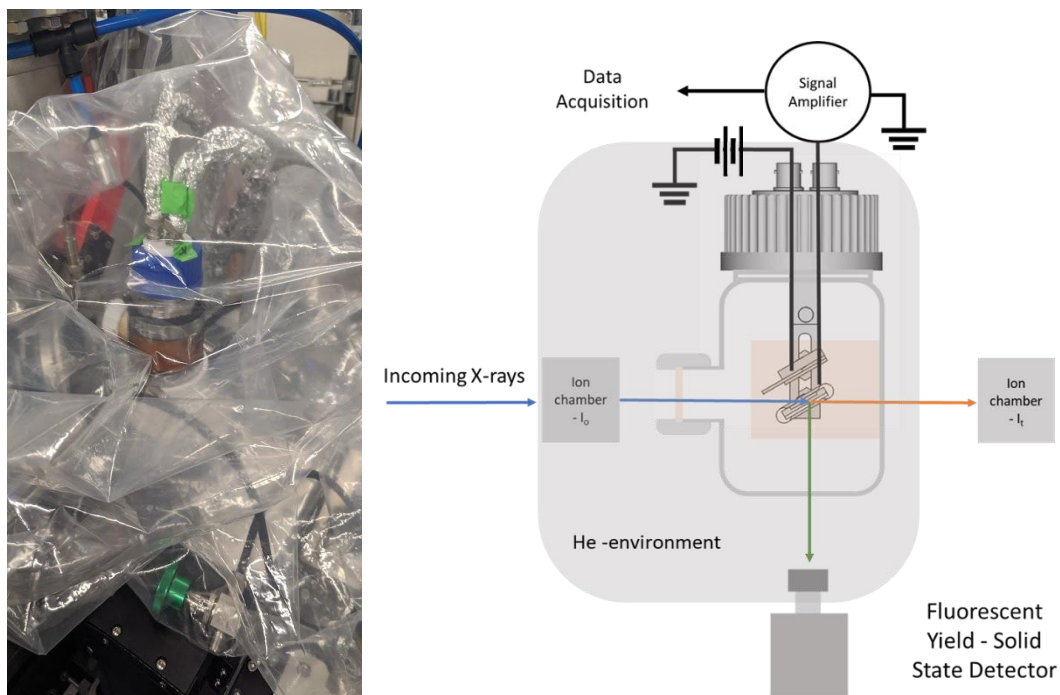
Figure 6.4.4 Experimental setup for XANEs measurements by TEY and transmission.

The design of the cell enables chemical treatment of the sample under similar conditions to HTCBT. The cell is transported between a wet chemistry laboratory and the beamline for *in situ* experiments. During the chemical treatment of the sample, the cell's grub screw (on the top of the bottle) is removed to prevent over-pressurisation. One bellows-sealed valve is used to introduce oil into the cell, along with the peristaltic pump. After submerging the sample, the valve is closed, and the cell is placed on a heating plate to heat the oil inside. Air is introduced into the cell through one bellows-sealed valve. After a period of time, air pumping into the cell is stopped by closing the valve, and the oil is removed using the peristaltic pump. Cyclohexane is then introduced into the cell through one of the valves. The sample is submerged for five minutes before being removed using the peristaltic pump. Cyclohexane will remove residual oil on the sample's surface, which would otherwise attenuate the Auger signal. Finally, the grub screw is reinserted, and the cell is taken to the beamline, inserted into the glove bag, and helium is introduced into the cell through the bellows-sealed valve.

6.4.1 Experiment

X-ray absorption spectroscopy (XAS) measurements were performed at the I18 beamline of the Diamond Light Source facility. The I18 beamline is designed to deliver monochromatic X-rays within the energy range of 2 to 20 keV and utilises a Si (111) monochromator. The beam was focused to $10\,\mu m$ x $10\,\mu m$ for the experiments. For TEY, the counter electrode was biased to $+135$ V.

The custom-designed cell measured the X-ray absorption near edge structure (XANES) of a copper foil in transmission and total electron yield (TEY) modes. The Cu foils with dimensions 15mm diameter disc x 4 µm were obtained from Goodfellows.

The Cu K-edge XANES spectra were collected in the 8830-9150 eV energy range. The experimental setup was mounted on a 3-axis stage to ensure precise sample alignment. The chucks are positioned such that the samples' normal is approximately 30° with the incident beam. At 30°, the X-ray beam path through the Cu foil is one absorption length.

The cell was encapsulated in a glove bag to maintain a stable helium atmosphere during the experiments. The glove bag was purged of air by inflating and deflating it three times with a flow of helium, and He-flow was continuously circulated through the glove bag and the cell during the measurements and was kept at positive pressure.

6.4.2 Results and Discussion

In situ experiments were attempted using the methods detailed in the previous. The experimental configuration for the chemical treatment conducted in a wet chemistry laboratory is shown in Figure 6.4.5. As a precautionary measure, heating of the cell was facilitated through a 2 L borosilicate beaker in case of a potential leak.

Figure 6.4.5 Experimental setup for in situ chemical treatment of the Cu foil.

During the early *in situ* studies, an unexpectedly small edge jump: background ratio of 1:2 was observed in the resulting TEY spectra (Figure 6.4.6) relative to the background. The edge jump: background ratio deviates from the anticipated circuitry behaviour. This would suggest that background electrons (low energy inelastically scattered from the sample) are dominating the signal. For gas-flow TEY it is desired the edge jump: background is $\gg$ 1 i.e. signal significantly above background. This observation raised the possibility of the recorded spectra data being influenced by electromagnetic disturbances, such as vibrations from loose or unshielded wires in the Earth's magnetic field, introducing noise into the signal. Despite the small edge jump and noise, the spectra contain features resembling Cu(0). The edge position for Cu metal is 8978.4 eV. Slightly above the edge, a peak at 8979.94 eV is attributed to the 1 s $\rightarrow$ 4p transition.[114] Features above 9000 eV are difficult to distinguish due to the noise.
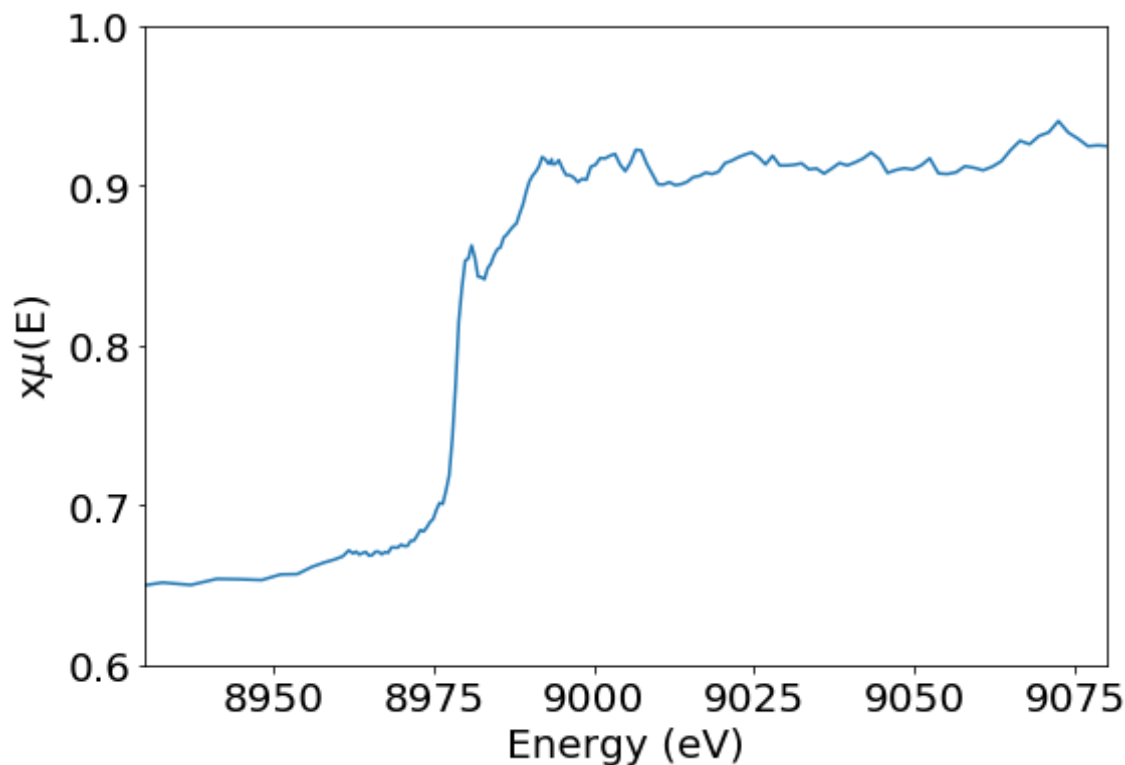
Figure 6.4.6 TEY measurement of Cu foil from *in situ* studies showing a small edge jump and a high background.

The underlying cause for the small edge jump was identified as the bias plate not being grounded effectively, resulting in the absence of bias applied to the sample. The TEY spectrum measured using this configuration is, therefore likely to arise from fluorescent photons incident on the gold wire inducing a current proportional to the I_{FY}. This would explain the damped oscillations above the edge characteristic of the self-absorption effects of concentrated samples.[119,154]

The circuitry was reconfigured to establish proper electrical grounding, ensuring a stable and reliable experimental setup. The XANES of a 4 µm foil was measured again in transmission and He-flow TEY. The immediate impact of the correctly grounded circuitry is evident through the substantial increase in the measured signal. Consequently, the gain on the amplifier required a reduction by one order of magnitude to ensure proper functionality and effectively accommodate the amplified signal. The normalised spectra from the measure transmission and TEY measurement are plotted in Figure 6.4.7.
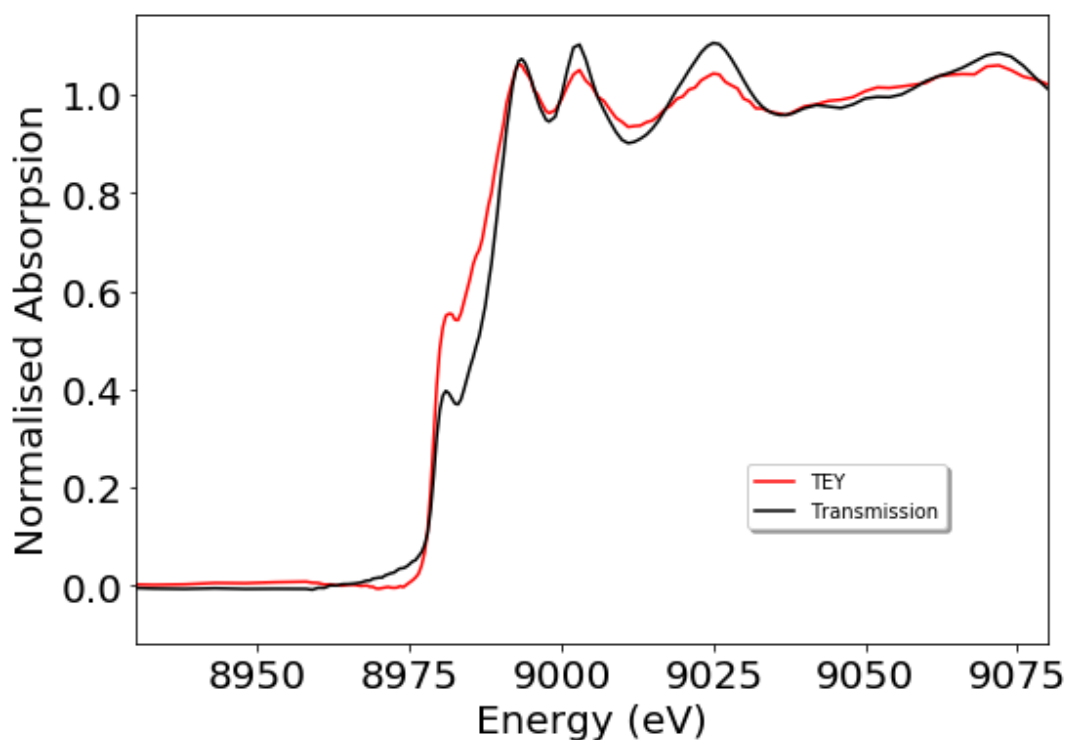
Figure 6.4.7 XANES spectra of Cu foil by TEY (red line) and transmission (black line).

The TEY spectra obtained for the Cu foil have a good signal-to-noise ratio with all the expected features from Cu metal spectra. However, comparing the TEY and transmission spectra shows self-absorbtion distortions, i.e. enhanced pre-edge features and damped post-edge features. This would indicate a small quantity of air inside the cell where florescent photons are generating photoelectrons. The purity of the He source may be compromised, or possibly the entry of air through the tubing connectors prior to entering the glove bag/cell.

6.5 Development of a Total Electron-Yield Detector for In Situ XAS Tribometer Studies

The development of the detector TEY for *operando* characterisation of tribofilm was to pursue the search for anti-wear additives to replace zinc dialkyl dithiophosphates (ZDDPs) in lubricant formulations. Since the 1940s, ZDDPs have continuously been used in automotive lubrication as an anti-wear additive.[6] However, the presence of sulphur (S) and phosphorus (P) in ZDDPs can lead to the formation of by-products that contaminate catalytic converters, reducing their efficiency in reducing exhaust emissions,[135] and are toxic to the environment. Among the promising alternatives, vanadium (V), molybdenum (Mo), and tungsten (W) based additives have shown potential. Developing such alternatives is currently prioritised from both commercial and environmental perspectives.

In collaborative research between the University of Leeds, the University of Bath, and Infineum UK Ltd, tribological testing of vanadium-based formulation has been performed, which revealed promising anti-wear properties of V(IV) oxyacetylacetonate ($VO(acac)_2$) complexes. *Operando* V K-edge (5465 eV) XAS by combined FY and TEY detection was conducted to gain deeper insights into the changes occurring within tribofilms under extreme conditions. The main objective was to investigate variations in oxidation states, composition, and local structure of the tribofilms when subjected to elevated temperatures, pressures, and shear forces.
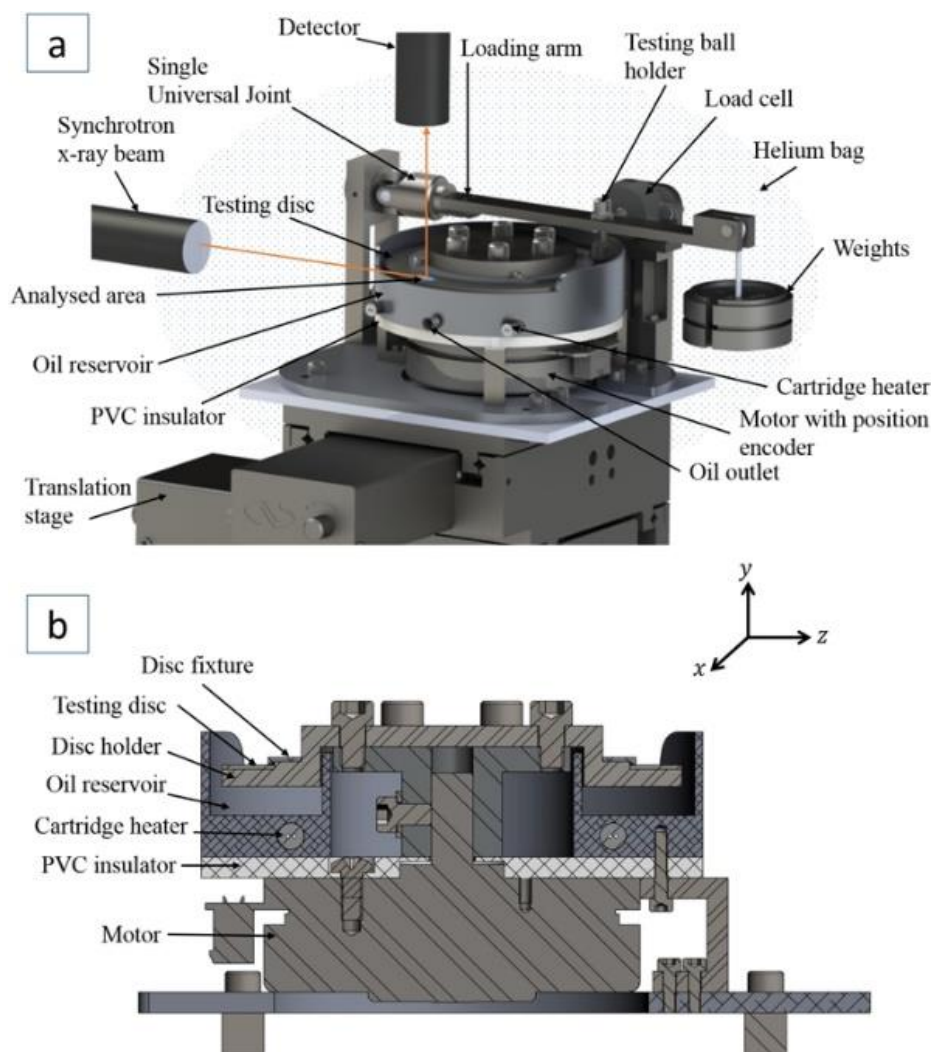
Figure 6.5.1 The configuration of the experimental setup for the *in situ* XAS investigations showcasing both the assembly (a) and a cross-sectional view (b) of the tribometer. The schematic highlights the detection geometry used in previous synchrotron experiments. The fluorescent-yield detector is at right angles to the incident X-ray beam and directly vertical to the tribological surface. [158]

A tribometer (Figure 6.5.1) for *in situ* and *operando* measurements was previously developed to characterise ZDDP tribofilms by fluorescent yield (FY) detection. [158] The design of the tribometer accommodates measurements of the tribofilm at the sulphur -edge and phosphorus K-edges (at approximately 2 keV and 2.4 keV, respectively). Air is extremely attenuating at the photon energies required for recording the XA spectra, so the measurements are performed in a helium environment using a helium-filled glove bag. The aim was to design an add-on TEY device for conducting He-flow TEY, which adds valuable surface-sensitive chemical information complementing the less surface-sensitive FY measurements that were previously obtained with this tribometer.
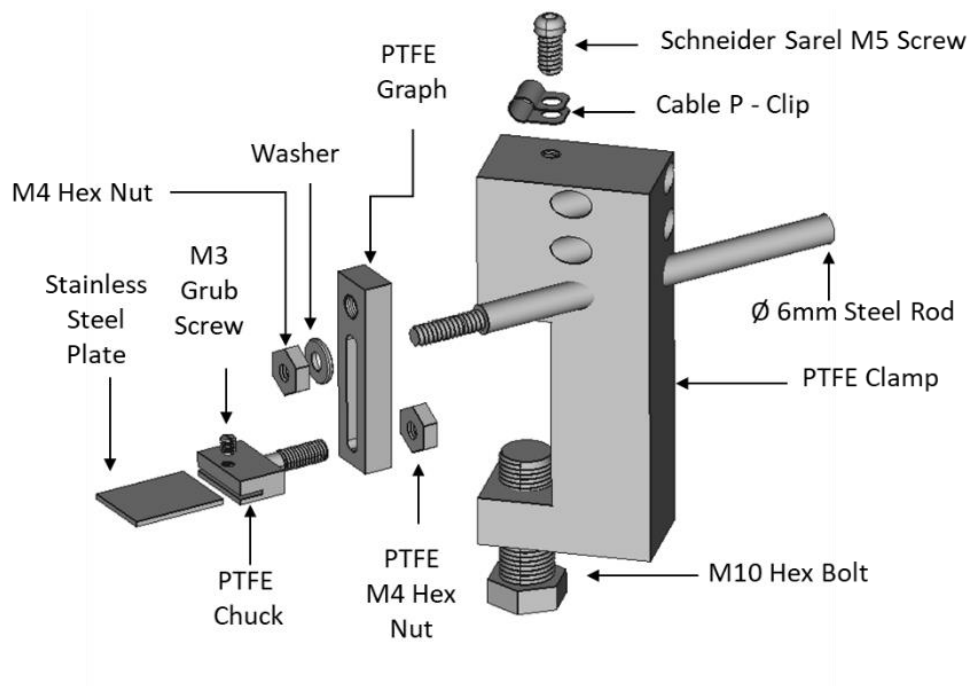
Figure 6.5.2 CAD drawings of the TEY detector.

A clamp-and-rod structure was designed to mount the TEY circuitry (Figure 6.5.2), seamlessly integrating into the tribometer. Polytetrafluoroethylene (PTFE) was chosen for the clamp fabrication as it is resistant to chemicals and can withstand the elevated temperatures required for the experiments (100ºC).

The TEY electron collector was mounted directly above the focal spot where the X-rays impinge on the sample. The three holes on the PTFE bracket allow variation in the vertical distance between the counter electrode/electron collector and analysis area. Additionally, lateral adjustment of the electron collector can be made by adjusting the position and the extent of protrusion of the rod.

The measured TEY spectrum corresponds to native signal currents in the pico- and nanoamps range so that significant noise can be introduced to the signal when cables conducting it move or vibrate in the earth's magnetic field. Several design features were employed to manage and minimise vibrations, such as:

- The clamp can be fastened securely using the M10 hex bolt.
- The steel rod fits snugly into the holes on the clamp's body. At high temperatures, thermal expansions would continue to secure the rod.
- The wires are secured on the top of the device to minimise vibration.

A photograph of the clamp assembly attached to the tribometer is shown in Figure 6.5.3.

Figure 6.5.3 Image of the clamp assembly fixed on the side of the tribometer.

6.5.1 Experiment

a

b
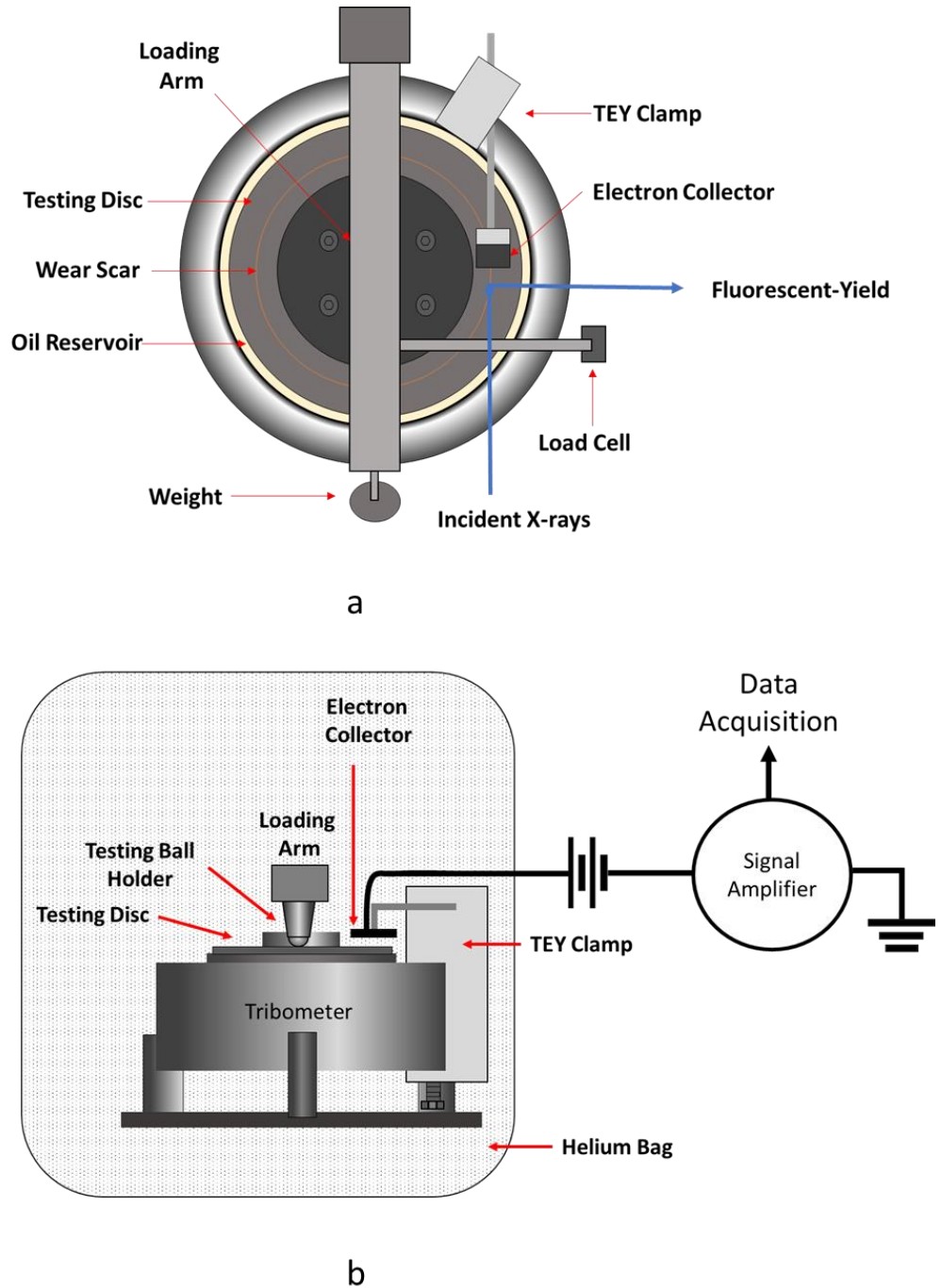
Figure 6.5.4 Schematic of the experimental setup for tribological investigations. (a) Birds-eye view of the tribometer illustrating the X-ray geometry used for TEY and FY measurements. (b) Side view of the experimental setup, including the TEY circuitry responsible for capturing and analysing electron yield data.

The experiments were conducted at PETRA III's P64. Beamline P64 is an X-ray Absorption Fine Structure (XAFS) beamline with an energy range of 4 to 44 keV, generating a photon flux of up to $\sim 10^{13}$ s^{-1}. The tribometer setup was secured on four axial motorised stages, allowing lateral position adjustment in the x, y, and z-axis and angular manipulation relative to the incident beam. These stages were similar to the ones depicted in Figure 6.5.1. A beam with dimensions of 150 µm x 100 µm was employed for this experiment. The tribometer was positioned at an angle of 2° relative to the incident beam during measurements.

The tribometer was set up with TEY apparatus, as shown in Figure 6.5.4. Measures were taken to ensure adequate electromagnetic shielding of the signal-carrying wires, minimising electromagnetic interference. Coaxially shielded wiring and cabling were utilised, providing electromagnetic shielding, and additional aluminium foil was wrapped around the coaxial wires to enhance shielding.

The setup was encapsulated in a glove bag (Figure 6.5.4b) to maintain a stable helium atmosphere during the experiments. The glove bag was purged of air by inflating and deflating it three times with a continuous flow of He to purge air inside the bag. Helium flow was continuously circulated through the glove bag during measurements and was kept at positive pressure to ensure the environment was not contaminated by ambient air.

6.5.2 Results and Discussion

The test oil in this study contained a concentration of 10 mmol of VO(acac)$_2$ dissolved in base oil (BO). Prior to *in situ* tribological testing, the vanadium complex in the base was characterised using FY and TEY simultaneously. These measurements were performed to establish the initial state and concentration of the vanadium complex, providing essential baseline data for subsequent tribological investigations. The FY, TEY measurement of the oil at room temperature (RT) and transmission measurement of a VO(acac)$_2$ pallet were measured for comparison. The spectra from these measurements are plotted in Figure 6.5.5.

A VO(acac)$_2$ reference pellet, measured in transmission, had an edge position of 5481.0 eV. Investigated in the tribometer was VO(acac)$_2$ in base oil, which was found to have an edge position of 5475.9 eV by FY XAS, and 5479.2 eV by TEY (Figure 6.5.5).
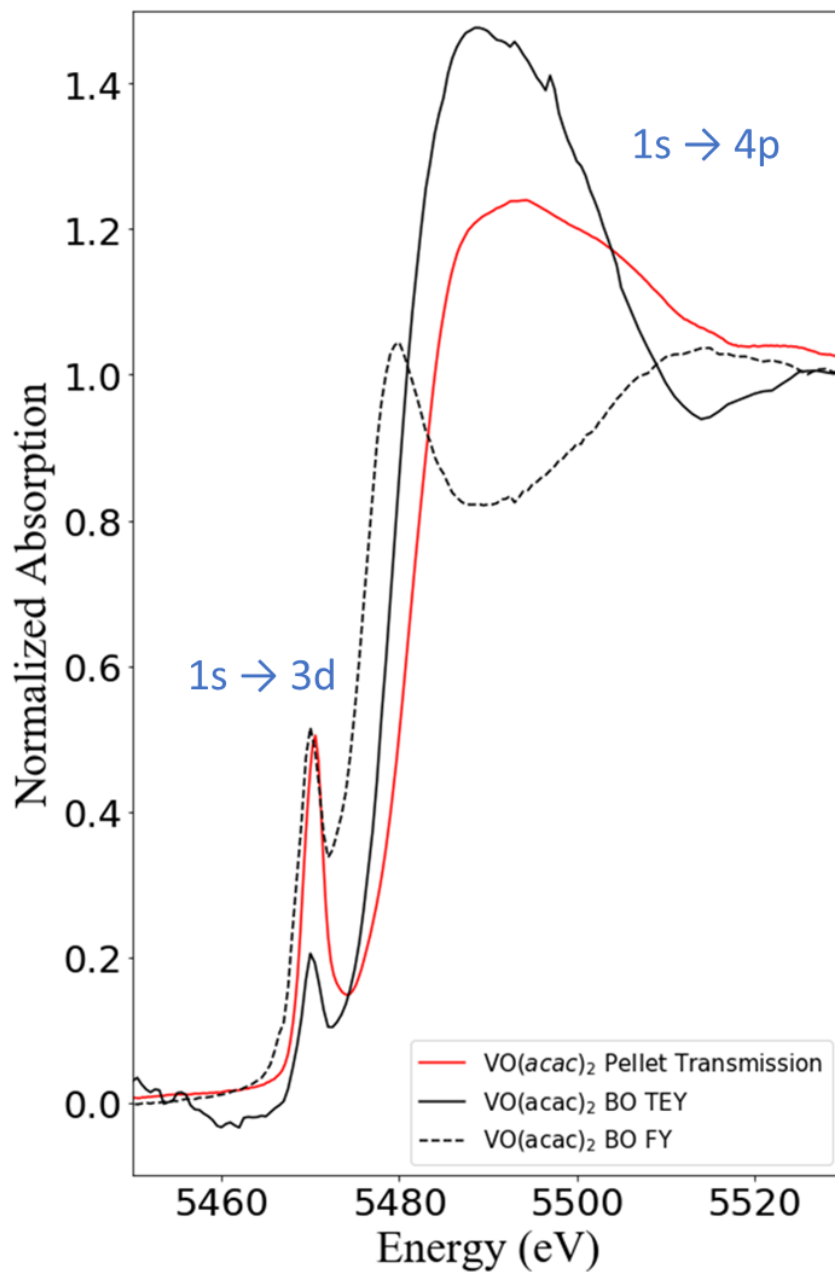
Figure 6.5.5 The figure plots the normalised absorption spectra of VO(acac)$_2$ in base oil were obtained using FY (solid black line) and TEY (dotted black line) detection techniques and transmission measurement of a VO(acac)$_2$ standard.

From the spectra obtained, the chemical distinction between the surface vanadium complex on the oil's surface and the oil's bulk vanadium complex is evident, as indicated by pronounced variations in the spectra, such as edge positions and post-edge oscillations acquired through TEY and FY detection methods. First, the chemical state of the pure additive, measured by transmission, appears to change when dissolved in the solution, as indicated by the FY spectrum in Figure 6.5.5. The oil solution of the complex is exposed to oxygen from the air prior to purging of the glove bag, which may lead to additional chemical changes. Indeed, the TEY spectrum indicates the presence of a vanadium species near the oil surface through a lower intensity of the pre-edge feature at ~5468 eV and a slightly positive shift of the edge position. The post-edge spectrum also differs significantly from that of the bulk species detected by FY XAS. These discrepancies provide compelling evidence for the differentiation of chemical species between the surface region and the bulk of the oil.

Unfortunately, while He-flow TEY successfully characterised the V complexes on the oil surface, it was not able to characterise the V complexes formed on the wear tracks. When this was attempted, an edge was observed in the FY spectra but not in the TEY spectra. This would suggest that the quantity of V on the wear track is below the detection limit of TEY. The expected absorption edge in TEY is likely obscured by the high background signal of electrons due to Auger emission from the steel, contributing to the gas phase ionisation and the measured current.

6.6   Conclusion

TEY technique is a sensitive and versatile tool for studying the surface chemistry of materials. A novel *in situ* XAS corrosion reaction cell was presented which can be used to investigate the surface chemistry of samples exposed to corrosive environments under the control of temperature and gas composition. A procedure for *in situ* measurements using this cell was demonstrated, and He-flow TEY XAS measurements were shown to be possible with this cell. However, the purity of the He flowed in the sample environment is essential for obtaining accurate results, as even small contamination with air leads to significant absorption of characteristic fluorescent photons from the sample, which then begins to dominate the TEY

signal. Monitoring the gas composition in the cell during measurements will be essential to obtain accurate TEY spectra with negligible FY contributions.

In addition, a He-flow TEY detector was developed to integrate into an existing tribometer. The detector was used to distinguish between the oil's surface and compare it with the V complex in the bulk oil obtained using FY measurements. The acquisition of surface-sensitive chemical information broadens the scope of analysis, offering valuable insights into the processes occurring at the interface. However, the quantity of V in the wear track was below the detection limit of the He-TEY, preventing the characterisation of V in the tribofilms formed in the wear tracks.

The development of these devices has demonstrated the versatility of applying He-flow TEY to tribological samples. However, the devices also highlight the challenges and limitations that must be addressed for effective implementation.

7   Conclusions and Further Work

7.1   Conclusions

The research presented in this thesis aimed to investigate the mechanism of non-aqueous Cu corrosion by lubricant additives using X-ray spectroscopies. To achieve this aim, a modified HTCBT experiment was set up and studies of the additives ZDDP and MoDTC performed. Both are additives known to have a strong affinity to corrode Cu. To monitor the chemical phases forming on the Cu surface using surface-sensitive techniques such as XPS and XAS via TEY measurement. The secondary aim of this thesis was to develop methods of characterizing lubricant systems *operando* and *in situ*. To meet this aim, two TEY detection systems were developed.

Fundamental corrosion studies of MoDTC on Cu surfaces were discussed in Chapter 4. The reaction of Cu with base oil forms Cu oxide. The oxide layer increases in thickness with increasing temperature, as observed in the Cu LMM spectra. $Cu(OH)_2$ is also observed on the surface, with increasing abundance with increasing temperature. $Cu(OH)_2$ was not observed when 0.1 wt% was added to the base oil. This was attributed to the antioxidant action readily reacting with alkyl peroxides and altering the chemical pathway such that $Cu(OH)_2$ is not produced.[128]

Additionally, HTCBT with 0.1 wt% MoDTC was conducted. Both XPS and XAS characterized the samples from these experiments via TEY. It was observed by XPS that an oxide overlayer first forms on the sample, which is attributed to the reaction of Cu with the heated base oil.   The Cu oxide layer then reacts with the MoO_xS_y particles formed by MoDTC.[67] The reaction is an ion exchange between O^{2-} on the surface of the coupon and the S^{2-} from the particles.

The cell discussed in Chapter 4 was used to characterize samples from the HTCBT with 0.1 wt%, using XAS via TEY *ex situ*. The TEY spectra were analyzed using LCF of known reference compounds measured by transmission. LCF analysis shows that a sulphide layer was

substituting the oxide layer initially formed as a function of time. This is in agreement with the observations by XPS.

The corrosion mechanism of the ZDDP on the Cu surface during the HTCBT was investigated and discussed in Chapter 5. Using XPS, it was found that the resulting composition of the thermal film formed on the surface of the substrate differed depending on the additive concentration.

With a concentration of 1.0 wt%, it was found that a glassy thiophosphate film formed on the surface. The phosphate chain length was calculated, which showed that the chain length initially decreased and then increased. The thermal film initiated the corrosion via a Zn^{2+}/Cu^{2+} ion exchange within the film. However, it is believed by the author that corrosion's main mechanism of the Cu coupon occurs when the thermal film is removed and exposing the surface of Cu, where thiols can readily react with the surface forming Cu_2S.

The thermal film formed with 0.1 wt% ZDDP contained Zn and Cu oxides with similar phosphate chain lengths as the one produced with 1.0 wt%. The tarnish formed on these surfaces is due to a carbon-based overlayer. The formation of this tarnish is likely due to the polymerisation of aliphatic carbon from the termination reactions of the free radical chain reaction.

Furthermore, using Ar^+ etching, the thermal film formed on the Cu surface after 72 h on emersion to the HTCBT with 0.1 wt% ZDDP was depth profiled. It shows that the thiophosphate chain length increases as a fiction of depth. It was also found that there is an increase in S content as a function of depth, which agrees with the literature.

Finally, in chapter 6, a cell with an integrated TEY detection system was developed. This cell is designed to subject a Cu sample to HTCBT conditions by introducing lubricants and air to the cell. The cell could then be heated externally, using a heating plate to 135°C. The design aims to characterise the metal/lubricant interface *in situ* using He-TEY. It was demonstrated that He-flow TEY is possible with this cell; however, the He introduced into the cell was contaminated with air. This led to a self-absorption distortion in the resulting spectra of pure

Cu foil. Although *in situ* studies were not performed, a procedure for *in situ* measurements using this cell was outlined.

In addition, chapter 6 also presents the development of a TEY device, capable of seamlessly integrating into an existing tribometer. The tribometer was originally designed to correlate the chemical speciation, via XAS measurement of FY, formed on the wear track with the frictional data. A He-flow TEY detector was developed to integrate into an existing tribometer seamlessly and complement the measurements obtained by FY with surface-sensitive TEY. The detector was used to distinguish V complexes in the oil's bulk and on the surface. However, the quantity of V on the surface is not detectable by TEY and could not be characterized.

In summary, the Cu corrosion mechanism by lubricant additives was investigated using surface-sensitive X-ray spectroscopy. The corrosion mechanism of ZDDP was investigated with XPS. A reaction cell with an integrated TEY detector was developed to monitor the chemical phase formed on the surface, but further optimisation of this set-up is required to perform the *in situ* experiments. Nevertheless, the cell allowed for ex situ XAS measurements, which gave valuable insight into the corrosion mechanism of MoDTC on Cu surfaces. The observations in XAS are in agreement with XPS.

7.2 Further Work

In Chapter 5, it was found that the elimination of the thiophosphate film leads to the exposure of the Cu surface to thiols. To comprehensively explain this phenomenon, further investigation is required into the mechanism by which the thermal film is removed from the surface. The results from this investigation would complete the corrosion mechanism.

One of the objectives of this thesis was to explore the synergistic corrosion mechanism involving MoDTC and ZDDP on copper surfaces. However, this remained unaddressed. Notably, prior studies have documented the potential exchange of Zn and Mo ligands in solution. This phenomenon may have implications, potentially leading to the creation of more stable thiophosphate glass films on the coupon's surface. These films, in turn, could serve as

passive protective layers, mitigating the effects of thiols on corrosion. The characterisation methodologies used in chapter 4 and 5 have successfully determined the chemical speciation formed on the Cu surface. Similar characterisation methodologies can be used to investigate the synergistic corrosion mechanisms of MoDTC and ZDDP to Cu.

In Chapter 6, the development of a novel He-flow TEY reaction cell to characterised Cu corrosion *in situ* was discussed. XAS spectra of Cu foil were obtained via He-flow TEY with self-absorption distortions due to air contamination in the gas phase. Further work is required to ensure that air does not contaminate the He is entering the cell. Replacing the polyurethane tubing with the plastic quick connect with stainless steel (metal) compression fitting from the He (bottle) to the cell and the He bag/cell would reduce contamination of the He supply. Furthermore, characterisation and monitoring of the gas composition inside the bottle could be done by mass-spectrometry (MS). In addition, further experiments could demonstrate the cell's ability to collect FY spectra of the liquid phase and XRD of the solid samples.

Other characterisation techniques can be incorporated into these studies, such as tunnelling electron microscopy (TEM) paired with energy-dispersive X-rays (EDX). A Focused ion beam (FIB) can prepare cross-sections on the tarnish layer. *In situ* tribological studies have previously been conducted using these techniques by Hu et al. 2008.[159] Such techniques complement the surface-sensitive techniques used here and confirm the Cu^{2+}/Zn^{2+} and O^{2-}/S^{2+} ion exchanges proposed in the ZDDP and MoDTC corrosion mechanism, respectively.

Finally, combustion temperature in diesel engines can reach the temperature at which NO_x can be generated. The production of NO_x can, in turn, accelerate the oxidation reactions and propagate corrosion.[160] To investigate how NO_x may alter the corrosion process, the HTCBT can be modified to incorporate NO_x into the gas bubbled through the oil. This method can potentially deepen our understanding of the intricate interplay between combustion temperatures, NO_x generation, and its corrosive impact on engine components.

8 References

1. Bowman, E. *et al. International Measures of Prevention, Application and Economics of Corrosion Technology Study*. (2016).

2. Nakada, M. Trends in engine technology and tribology. *Tribol Int* **27**, 3–8 (1994).

3. Becker, E. P. Trends in tribological materials and engine technology. *Tribol Int* **37**, 569–575 (2004).

4. Brown, S. F. B. Base Oil Groups: Manufacture, Properties and Performance. *Tribology & Lubrication Technology* (2015).

5. Jardine, F. Engine Corrosion-its Causes And Avoidance. in (1925). doi:10.4271/250030.

6. Spikes, H. The history and mechanisms of ZDDP. *Tribology Letters* **17**, 469–489 (2004).

7. ASTM. Standard Test Method for Evaluation of Corrosiveness of Diesel Engine Oil at 135 °C 1. Preprint at https://doi.org/10.1520/D6594-14.

8. Kjellén, L. Hoganas - Why make a copper-free oil cooler? *https://www.hoganas.com/en/Industries/insights-by-hoganas/why-make-a-copper-free-oil-cooler/* (2021).

9. Gebretsadik, D. W., Hardell, J. & Prakash, B. Tribological performance of tin-based overlay plated engine bearing materials. *Tribol Int* **92**, 281–289 (2015).

10. Thomson, J. *et al.* Development Of A Lead-free Bearing Material For Aerospace Applications. *International Journal of Metalcasting/Winter* **4**, 19–30 (2010).

11. Kerr, I., Priest, M., Okamoto, Y. & Fujita, M. Friction and wear performance of newly developed automotive bearing materials under boundary and mixed lubrication

regimes. *Proceedings of the Institution of Mechanical Engineers, Part J: Journal of Engineering Tribology* **221**, 321–331 (2007).

12. Langbein, F., Loidl, M., Eberhard, A. & Mergen, R. SLIDE BEARING TYPES FOR COMBUSTION ENGINES DESIGNED FOR UPCOMING EMISSION REGULATIONS. in *Proceedings of the ASME 2009 Internal Combustion Engine Division Fall Technical Conference ICEF2009* (2009).

13. Vencl, A. & Rac, A. Diesel engine crankshaft journal bearings failures: Case study. *Eng Fail Anal* **44**, 217–228 (2014).

14. Gebretsadik, D. W., Hardell, J. & Prakash, B. Friction and wear characteristics of different Pb-free bearing materials in mixed and boundary lubrication regimes. *Wear* **340–341**, 63–72 (2015).

15. American Society for Testing and Materials. Standard Test Method for Corrosiveness to Copper from Petroleum Products by Copper Strip Test1. Preprint at https://doi.org/https://doi.org/10.1520/D0130-19 (2006).

16. Gao, S., Yang, L., Deng, B. & Zhang, J. Corrosion mechanism for local enrichment of acids and copper ions in copper-insulating paper contacts leading to the acceleration of copper sulfide formation induced by dibenzyl disulfide. *RSC Adv* **7**, 52475–52485 (2017).

17. Gattinoni, C. & Michaelides, A. Atomistic details of oxide surfaces and surface oxidation: the example of copper and its oxides. *Surf Sci Rep* **70**, 424–447 (2015).

18. Alavi, K. Molecular Beam Epitaxy. in *Encyclopedia of Materials: Science and Technology* 5765–5780 (Elsevier, 2001). doi:10.1016/B0-08-043152-6/01002-0.

19. Junell, P., Ahonen, M., Hirsimäki, M. & Valden, M. Influence of surface modification on the adsorption dynamics of O 2 on Cu{100}. *Surface Review and Letters* **11**, 457–461 (2004).

20. Ahonen, M. *et al.* Adsorption dynamics of O2 on Cu(1 0 0): The role of vacancies, steps and adatims in dissociative chemisorption of O2. *Chem Phys Lett* **456**, 211–214 (2008).

21. Jaatinen, S. *et al.* Adsorption and diffusion dynamics of atomic and molecular oxygen on reconstructed Cu(100). *Phys Rev B* **75**, 075402 (2007).

22. Li, L. *et al.* Surface-Step-Induced Oscillatory Oxide Growth. *Phys Rev Lett* **113**, 136104 (2014).

23. Yang, J. C., Yeadon, M., Kolasa, B. & Gibson, J. M. Oxygen surface diffusion in three-dimensional Cu2O growth on Cu(001) thin films. *Appl Phys Lett* **70**, 3522–3524 (1997).

24. Pinnel, M. R., Tompkins, H. G. & Heath, D. E. Oxidation Of Copper In Controlled Clean Air And Standard Laboratory Air At 50 °C to 150 °C. *Applications of Surface Science* **2**, 558–577 (1979).

25. Platzman, I., Brener, R., Haick, H. & Tannenbaum, R. Oxidation of Polycrystalline Copper Thin Films at Ambient Conditions. *The Journal of Physical Chemistry C* **112**, 1101–1108 (2008).

26. Cabrera, N. & Mott, N. F. Theory of the Oxidation of Metals. *Reports on Progress in Physics* **12**, 308 (1949).

27. Iijima, J. *et al.* Native oxidation of ultra high purity Cu bulk and thin films. *Appl Surf Sci* **253**, 2825–2829 (2006).

28. Keil, P., Frahm, R. & Lützenkirchen-Hecht, D. Native oxidation of sputter deposited polycrystalline copper thin films during short and long exposure times: Comparative investigation by specular and non-specular grazing incidence X-ray absorption spectroscopy. *Corros Sci* **52**, 1305–1316 (2010).

29. Zuo, Z. J., Li, J., Han, P. De & Huang, W. XPS and DFT studies on the autoxidation process of Cu sheet at room temperature. *Journal of Physical Chemistry C* **118**, 20332–20345 (2014).

30. Lim, J.-W., Ishikawa, Y., Miyake, K., Yamashita, M. & Isshiki, M. *Influence of Substrate Bias Voltage on the Properties of Cu Thin Films by Sputter Type Ion Beam Deposition*. *Materials Transactions* vol. 43 (2002).

31. Fateh, A., Aliofkhazraei, M. & Rezvanian, A. R. Review of corrosive environments for copper and its corrosion inhibitors. *Arabian Journal of Chemistry* vol. 13 481–544 Preprint at https://doi.org/10.1016/j.arabjc.2017.05.021 (2020).

32. Hultquist, G., Szakálos, P., Graham, M. J. & Sproule, G. I. Detection Of Hydrogen In Corrosion Of Copper In Pure Water. in *17th International Corrosion Congress 2008: Corrosion Control in the Service of Society* 1–9 (2008).

33. Hedman, T., Nyström, A. & Thegerström, C. Swedish containers for disposal of spent nuclear fuel and radioactive waste. *C R Phys* **3**, 903–913 (2002).

34. Aguilar, G., Mazzamaro, G. & Rasberger, M. Oxidative Degradation and Stabilisation of Mineral Oil-Based Lubricants. in *Chemistry and Technology of Lubricants* (eds. Mortier, R. M., Fox, M. F. & Orszulik, S. T.) (Springer, 2010).

35. Jayne, D. T., Shanklin, J. R. & Stachew, C. F. Controlling the Corrosion of Copper Alloys in Engine Oil Formulations: Antiwear, Friction Modifier, Dispersant Synergy. in *SAE Powertrain & Fluid Systems Conference & Exhibition* 01–2767 (2002). doi:10.4271/2002-01-2767.

36. Khabra, A., Pinhasi, G. A. & Zidki, T. NOx and SOx Flue Gas Treatment System Based on Sulfur-Enriched Organic Oil in Water Emulsion. *ACS Omega* **6**, 2570–2575 (2021).

37. Garcia-Anton, J., Monzo, J., Guionon, J. L., Gomez, D. & Costa, J. Study of corrosion on copper strips by petroleum naphtha in the ASTM D-130 test by means of electronic

microscopy (SEM) and energy dispersive X-ray (EDX). *Fresenius J Anal Chem* **337**, 382–388 (1990).

38. García-Antón, J., Monzó, J. & Guiñón, J. L. Effect of Elemental Sulfur and Mercaptans on Copper Strip Corrosion and Use of the ASTM D 130 Test Method. *Corrosion* **51**, 558–566 (1995).

39. Reid, D. G. & Smith, G. C. The X-ray Photoelectron Spectroscopy of Surface Films Formed During the ASTM D-130/ISO 2160 Copper Corrosion Test. *Pet Sci Technol* **32**, 387–394 (2014).

40. Welbourn, R. J. L., Truscott, C. L., Skoda, M. W. A., Zarbakhsh, A. & Clarke, S. M. Corrosion and inhibition of copper in hydrocarbon solution on a molecular level investigated using neutron reflectometry and XPS. *Corros Sci* **115**, 68–77 (2017).

41. Luo, Y.-H., Zhong, B.-Y. & Zhang, J.-C. The mechanism of copper-corrosion inhibition by thiadiazole derivatives. *Lubrication Engineering* **51**, 293–296 (1995).

42. Newley, R. A., Spikes, H. A. & Macpherson, P. B. Oxidative Wear in Lubricated Contact. *J. Tribol.* **102**, 539–544 (1980).

43. Gellman, A. J. & Spencer, N. D. Surface chemistry in tribology. *Proceedings of the Institution of Mechanical Engineers, Part J: Journal of Engineering Tribology* **216**, 443–461 (2002).

44. Barnes, A. M., Bartle, K. D. & Thibon, V. R. A. A review of zinc dialkyldithiophosphates (ZDDPS): characterisation and role in the lubricating oil. *Tribol Int* **34**, 389–395 (2001).

45. Palacios, J. M. Thickness and chemical composition of films formed by antimony dithiocarbamate and zinc dithiophosphate. *Tribol Int* **19**, 35–39 (1986).

46. Suominen Fuller, M. L. *et al.* The use of X-ray absorption spectroscopy for monitoring the thickness of antiwear films from ZDDP. *Tribol Lett* **8**, 187–192 (2000).

47. Piras, F. M., Rossi, A. & Spencer, N. D. Combined in situ (ATR FT-IR) and ex situ (XPS) Study of the ZnDTP-Iron Surface Interaction. *Tribol Lett* **15**, 181–191 (2003).

48. Willermet, P. A. *et al.* Formation, structure, and properties of lubricant-derived antiwear films. *Lubrication Science* **9**, 325–348 (1997).

49. Jones, R. B. & Coy, R. C. The Chemistry of the Thermal Degradation of Zinc Dialkyldithiophosphate Additives. *A S L E Transactions* **24**, 91–97 (1981).

50. Mitchell, P. C. H. Oil-soluble Mo-S compounds as lubricant additives. *Wear* **100**, 281–300 (1984).

51. Vanderbilt, R. T. Molybdenum-containing dithiophosphoric ester compounds. (1966).

52. Sakurai, T., Okabe, H. & Isoyama, H. The synthesis of di-m-thio-dithiobis(dialkyldithiocarbamates) dimolybdenum (V) and their effects on boundary Lubrication. *Journal of the Japan Petroleum Institute* **13**, 308–314 (1971).

53. Farmer, H. H. & Rowan, E. V. Molybdenum oxysulfide dithiocarbamates and processes for their preparation. (1967).

54. Braithwaite, E. R. & Greene, A. B. A critical analysis of the performance of molybdenum compounds in motor vehicles. *Wear* **46**, 405–432 (1978).

55. Kiw, Y. M., Schaeffer, P., Adam, P., Thiébaut, B. & Boyer, C. Dithiocarbamate transfer reaction from methylene-bis(dithiocarbamates) to molybdenum dithiocarbamates in engine lubricants investigated using laboratory experiments. *New Journal of Chemistry* **46**, 22341–22352 (2022).

56. Ye, J., Kano, M. & Yasuda, Y. Evaluation of local mechanical properties in depth in MoDTC/ZDDP and ZDDP tribochemical reacted films using nanoindentation. *Tribol Lett* **13**, 41–47 (2002).

57. De Feo, M. *et al.* MoDTC lubrication of DLC-involving contacts. Impact of MoDTC degradation. *Wear* **348–349**, 116–125 (2016).

58. Morina, A., Neville, A., Priest, M. & Green, J. H. ZDDP and MoDTC interactions in boundary lubrication—The effect of temperature and ZDDP/MoDTC ratio. *Tribol Int* **39**, 1545–1557 (2006).

59. Morina, A., Neville, A., Priest, M. & Green, J. H. ZDDP and MoDTC interactions and their effect on tribological performance - Tribofilm characteristics and its evolution. *Tribol Lett* **24**, 243–256 (2006).

60. Kasrai, M. *et al.* The Chemistry of Antiwear Films Generated by the Combination of ZDDP and MoDTC Examined by X-ray Absorption Spectroscopy. *Tribology Transactions* **41**, 69–77 (1998).

61. Kasrai, M. *et al.* The chemistry of antiwear films generated by the combination of zddp and modtc examined by x-ray absorption spectroscopy. *Tribology Transactions* **41**, 69–77 (1998).

62. Winer, W. O. Molybdenum disulfide as a lubricant: A review of the fundamental knowledge. *Wear* **10**, 422–452 (1967).

63. Onodera, T. *et al.* A computational chemistry study on friction of h-MoS2. Part I. Mechanism of single sheet lubrication. *J Phys Chem B* **113**, 16526–16536 (2009).

64. Wan, G. T. Y. & Spikes, H. A. The Behavior of Suspended Solid Particles in Rolling and Sliding Elastohydrodynamic Contacts. *Tribology Transactions* **31**, 12–21 (1988).

65. Cusano, C. & Sliney, H. E. Dynamics of Solid Dispersions in Oil During the Lubrication of Point Contacts, Part II—Molybdenum Disulfide 81709. in *Annual Meeting of the American Society of Lubrication Engineers* vol. 25 190–197 (1981).

66. Grossiord, C. *et al.* MoS2 single sheet lubrication by molybdenum dithiocarbamate. *Tribol Int* **31**, 737–743 (1998).

67. De Feo, M., Minfray, C., De Barros Bouchet, M. I., Thiebaut, B. & Martin, J. M. MoDTC friction modifier additive degradation: Correlation between tribological performance and chemical changes. *RSC Adv* **5**, 93786–93796 (2015).

68. Haruna, J. Lubricating composition comprising molybdenum dithiocarbamate and having reduced copper corrosion. (1998).

69. Greczynski, G. & Hultman, L. X-ray photoelectron spectroscopy: Towards reliable binding energy referencing. *Prog Mater Sci* **107**, 100591 (2020).

70. Moretti, G. Auger parameter and Wagner plot in the characterization of chemical states by X-ray photoelectron spectroscopy: a review. *J Electron Spectros Relat Phenomena* **95**, 95–144 (1998).

71. Major, G. H. *et al.* Practical guide for curve fitting in x-ray photoelectron spectroscopy. *Journal of Vacuum Science & Technology A: Vacuum, Surfaces, and Films* **38**, 061203 (2020).

72. Voigt, W. Akademie der Wissenschaften in MünchenNaturwissenschaftliche Classe. *Akademie der Wissenschaften in MünchenNaturwissenschaftliche Classe* **216**, 603–620 (1912).

73. Krause, M. O. & Oliver, J. H. Natural widths of atomic K and L levels, Kα X-ray lines and several KLL Auger lines. *J Phys Chem Ref Data* **8**, 329–338 (1979).

74. Fuggle, J. C. & Alvarado, S. F. Core-level lifetimes as determined by x-ray photoelectron spectroscopy measurements. *Phys Rev A (Coll Park)* **22**, 1615–1624 (1980).

75. Biesinger, M. C. Advanced analysis of copper X-ray photoelectron spectra. *Surface and Interface Analysis* **49**, 1325–1334 (2017).

76. Fairley, N. & Carrick, A. *The Casa Cookbook: Recipes for XPS Data Processing.* (Acolyte Science, Knutsford, 2005).

77. Seah, M. P. & Dench, W. A. Quantitative electron spectroscopy of surfaces: A standard data base for electron inelastic mean free paths in solids. *Surface and Interface Analysis* **1**, 2–11 (1979).

78. Powell, C. J. Practical guide for inelastic mean free paths, effective attenuation lengths, mean escape depths, and information depths in x-ray photoelectron spectroscopy. *Journal of Vacuum Science & Technology A: Vacuum, Surfaces, and Films* **38**, 023209 (2020).

79. Watts, J. F. & Wolstenholme, J. *An Introduction to Surface Analysis by XPS and AES*. (John Wiley & Sons, Ltd, 2003). doi:10.1002/0470867930.

80. Newville, M. Fundamentals of XAFS. *Rev Mineral Geochem* **78**, 33–74 (2014).

81. Fricke., H. The K-Characteristic Absorption Frequencies for the Chemical Elements Magnesium to Chromium. *Physical Review* **16**, 202–215 (1920).

82. Stern, E. A., Sayers, D. E. & Lytle, F. W. Extended x-ray-absorption fine-structure technique. III. Determination of physical parameters. *Phys Rev B* **11**, 4836–4846 (1975).

83. Stern, E. A. Theory of the extended x-ray-absorption fine structure. *Phys Rev B* **10**, 3027–3037 (1974).

84. Lytle, F. W., Sayers, D. E. & Stern, E. A. Extended x-ray-absorption fine-structure technique. II. Experimental practice and selected results. *Phys Rev B* **11**, 4825–4835 (1975).

85. Gurman, S. J., Binsted, N. & Ross, I. A rapid, exact curved-wave theory for EXAFS calculations. *Journal of Physics C: Solid State Physics* **17**, 143–151 (1984).

86. Gurman, S. J. The small-atom approximation in EXAFS and surface EXAFS. *Journal of Physics C: Solid State Physics* **21**, 3699–3717 (1988).

87.   Calvin, S. *XAFS for Everyone*. (CRC Press, 2013). doi:10.1201/b14843.

88.   Anon. XANES. *Open Textbook Pilot Project* 1869–1869 https://chem.libretexts.org/@go/page/1869 (2023).

89.   Newville, M. N. XANES Analysis: Linear Combination Analysis, Principal Component Analysis, Pre-edge Peak Fitting. *Larch: Data Analysis Tools for X-ray Spectroscopy* https://cars.uchicago.edu/xraylarch/xafs/xanes.html#:~:text=As%20a%20result%2C%20%E2%80%9CXANES%20Analysis,characteristic%20such%20as%20oxidation%20state. (2020).

90.   Passut, C. A. & Kollman, R. E. Laboratory Techniques for Evaluation of Engine Oil Effects on Fuel Economy. in (1978). doi:10.4271/780601.

91.   Tang, Z. & Li, S. A review of recent developments of friction modifiers for liquid lubricants (2007–present). *Curr Opin Solid State Mater Sci* **18**, 119–139 (2014).

92.   Yamamoto, Y. & Gondo, S. Friction and wear characteristics of Molybdenum Dithiocarbamate and Molybdenum Dithiophosphate. *Tribology Transactions* **32**, 251–257 (1989).

93.   Graham, J., Spikes, H. & Korcek, S. The friction reducing properties of molybdenum dialkyldithiocarbamate additives: part i — factors influencing friction reduction. *Tribology Transactions* **44**, 626–636 (2001).

94.   Feng, I.-M., Perilstein, W. L. & Adams, M. R. Solid Film Deposition and Non-Sacrificial Boundary Lubrication. *A S L E Transactions* **6**, 60–66 (1963).

95.   Yamamoto, Y., Gondo, S., Kamakura, T. & Konishi, M. Organoamine and organophosphate molybdenum complexes as lubricant additives. *Wear* **120**, 51–60 (1987).

96. McDevitt, N. T., Donley, M. S. & Zabinski, J. S. Utilization of Raman spectroscopy in tribochemistry studies. *Wear* **166**, 65–72 (1993).

97. Zabinski, J. S., Donley, M. S., Walck, S. D., Schneider, T. R. & Mcdevitt, N. T. The Effects of Dopants on the Chemistry and Tribology of Sputter-Deposited MoS $_2$ Films. *Tribology Transactions* **38**, 894–904 (1995).

98. Grossiord, C., Martin, J. M., Le Mogne, T. & Palermo, T. In situ MoS2 formation and selective transfer from MoDPT films. *Surf Coat Technol* **108–109**, 352–359 (1998).

99. Martin, J. M., Belin, M., Mansot, J. L., Dexpert, H. & Lagarde, P. Friction-Induced Amorphization with ZDDP—An EXAFS Study. *A S L E Transactions* **29**, 523–531 (1986).

100. Reed, B. P. *et al.* Versailles Project on Advanced Materials and Standards interlaboratory study on intensity calibration for x-ray photoelectron spectroscopy instruments using low-density polyethylene. *Journal of Vacuum Science & Technology A* **38**, 063208 (2020).

101. Scofield, J. H. *Theoretical photoionization cross sections from 1 to 1500 keV.* http://www.osti.gov/servlets/purl/4545040/ (1973) doi:10.2172/4545040.

102. Miller, D. J., Biesinger, M. C. & McIntyre, N. S. Interactions of CO2 and CO at fractional atmosphere pressures with iron and iron oxide surfaces: one possible mechanism for surface contamination? *Surface and Interface Analysis* **33**, 299–305 (2002).

103. Schroeder, S. L. M. Towards a 'universal curve' for total electron-yield XAS. *Solid State Commun* **98**, 405–409 (1996).

104. Powell, C. J. & Jablonski, A. Evaluation of electron inelastic mean free paths for selected elements and compounds. *Surface and Interface Analysis* **29**, 108–114 (2000).

105. Seah, M. P. An accurate and simple universal curve for the energy-dependent electron inelastic mean free path. *Surface and Interface Analysis* **44**, 497–503 (2012).

106. Tanuma, S., Powell, C. J. & Penn, D. R. Calculations of electron inelastic mean free paths. IX. Data for 41 elemental solids over the 50 eV to 30 keV range. *Surface and Interface Analysis* **43**, 689–713 (2011).

107. Zemek, J., Jiricek, P., Jablonski, A. & Lesiak, B. Elastic electron backscattering from silicon surfaces: effect of surface roughness. *Surface and Interface Analysis* **34**, 215–219 (2002).

108. Biesinger, M. C., Lau, L. W. M., Gerson, A. R. & Smart, R. St. C. Resolving surface chemical states in XPS analysis of first row transition metals, oxides and hydroxides: Sc, Ti, V, Cu and Zn. *Appl Surf Sci* **257**, 887–898 (2010).

109. Payne, B. P., Biesinger, M. C. & McIntyre, N. S. The study of polycrystalline nickel metal oxidation by water vapour. *J Electron Spectros Relat Phenomena* **175**, 55–65 (2009).

110. Payne, B. P., Biesinger, M. C. & McIntyre, N. S. X-ray photoelectron spectroscopy studies of reactions on chromium metal and chromium oxide surfaces. *J Electron Spectros Relat Phenomena* **184**, 29–37 (2011).

111. Gaur, A., Shrivastava, B. D. & Joshi, S. K. Copper K-edge XANES of Cu(I) and Cu(II) oxide mixtures. *J Phys Conf Ser* **190**, 012084 (2009).

112. Yilmaz, M., Handoko, A. D., Parkin, I. P. & Sankar, G. Probing the electronic and geometric structures of photoactive electrodeposited Cu2O films by X-ray absorption spectroscopy. *J Catal* **389**, 483–491 (2020).

113. Kau, L. S., Spira-Solomon, D. J., Penner-Hahn, J. E., Hodgson, K. O. & Solomon, E. I. X-ray absorption edge determination of the oxidation state and coordination number

of copper. Application to the type 3 site in Rhus vernicifera laccase and its reaction with oxygen. *J Am Chem Soc* **109**, 6433–6442 (1987).

114. Rudolph, J. & Jacob, C. R. Revisiting the Dependence of Cu K-Edge X-ray Absorption Spectra on Oxidation State and Coordination Environment. *Inorg Chem* **57**, 10591–10607 (2018).

115. Sarangi, R. *et al.* MXAN Analysis of the XANES Energy Region of a Mononuclear Copper Complex: Applications to Bioinorganic Systems. *Inorg Chem* **44**, 9652–9659 (2005).

116. Sarangi, R. *et al.* X-Ray absorption spectroscopic and theoretical studies on (L) 2[Cu2(S2)n]2+ complexes: Disulfide versus disulfide(•1-) bonding. *J Am Chem Soc* **130**, 676–686 (2008).

117. Kumar, P., Nagarajan, R. & Sarangi, R. Quantitative X-ray absorption and emission spectroscopies: electronic structure elucidation of Cu2S and CuS. *J Mater Chem C Mater* **1**, 2448 (2013).

118. Donoghue, P. J. *et al.* Rapid C–H Bond Activation by a Monocopper(III)–Hydroxide Complex. *J Am Chem Soc* **133**, 17602–17605 (2011).

119. Rayment, T. *et al.* Electron-yield x-ray absorption spectroscopy with gas microstrip detectors. *Review of Scientific Instruments* **71**, 3640–3645 (2000).

120. Morina, A. & Neville, A. Tribofilms: aspects of formation, stability and removal. *J Phys D Appl Phys* **40**, 5476–5487 (2007).

121. Bird, R. J. & Galvin, G. D. The application of photoelectron spectroscopy to the study of e. p. films on lubricated surfaces. *Wear* **37**, 143–167 (1976).

122. Khaemba, D. N., Neville, A. & Morina, A. New insights on the decomposition mechanism of Molybdenum DialkyldiThioCarbamate (MoDTC): a Raman spectroscopic study. *RSC Adv* **6**, 38637–38646 (2016).

123. Reid, D. G. & Smith, G. C. The X-ray photoelectron spectroscopy of surface films formed during the ASTM D-130/ISO 2160 copper corrosion test. *Pet Sci Technol* **32**, 387–394 (2014).

124. García-Antón, J., Monzó, J. & Guiñón, J. L. Effect of Elemental Sulfur and Mercaptans on Copper Strip Corrosion and Use of the ASTM D 130 Test Method. *Corrosion* **51**, 558–566 (1995).

125. Ponjavic, A., Lemaigre, T., Southby, M. & Spikes, H. A. Influence of NO x and Air on the Ageing Behaviour of MoDTC. *Tribol Lett* **65**, 52 (2017).

126. Butrymowicz, D. B., Manning, J. R. & Read, M. E. Diffusion in Copper and Copper Alloys. Part I. Volume and Surface Self-Diffusion in Copper. *J Phys Chem Ref Data* **2**, 643–656 (1973).

127. Pham, A. N., Xing, G., Miller, C. J. & Waite, T. D. Fenton-like copper redox chemistry revisited: Hydrogen peroxide and superoxide mediation of copper-catalyzed oxidant production. *J Catal* **301**, 54–64 (2013).

128. Johnson, M., Jensen, R. & Korcek, S. Additive Interactions and Depletion Processes in Fuel Efficient Engine Oils. in (1997). doi:10.4271/971694.

129. Grossiord, C., Martin, J.-M., Le Mogne, Th., Inoue, K. & Igarashi, J. Friction-reducing mechanisms of molybdenum dithiocarbamate/zinc dithiophosphate combination: New insights in MoS2 genesis. *Journal of Vacuum Science & Technology A: Vacuum, Surfaces, and Films* **17**, 884–890 (1999).

130. Yamamoto, Y. & Gondo, S. Friction and wear characteristics of Molybdenum Dithiocarbamate and Molybdenum Dithiophosphate. *Tribology Transactions* **32**, 251–257 (1989).

131. Martin, J. M., Le Mogne, Th., Grossiord, C. & Palermo, Th. Tribochemistry of ZDDP and MoDDP chemisorbed films. *Tribol Lett* **2**, 313–326 (1996).

132. Njiwa, P., Minfray, C., Belin, M., Rigaud, E. & Martin, J. M. Friction response of ZDDP thermal film and tribofilm. *Tribology - Materials, Surfaces and Interfaces* **5**, 129–132 (2011).

133. Bancroft, G. M. *et al.* Mechanisms of tribochemical film formation: stability of tribo- and thermally-generated ZDDP films. *Tribol Lett* **3**, 47–51 (1997).

134. Aktary, M., McDermott, M. T. & Torkelson, J. Morphological evolution of films formed from thermooxidative decomposition of ZDDP. *Wear* **247**, 172–179 (2001).

135. Bardasz, E. A. *et al.* Low Volatility ZDDP Technology: Part 2 - Exhaust Catalysts Performance in Field Applications. in *SAE TECHNICAL PAPER SERIES* (2007). doi:10.4271/2007-01-4107.

136. Handley, T. H. & Dean, J. A. O,O'-Dialkyl Phosphorodithioic Acids as Extractants for Metals. *Anal Chem* **34**, 1312–1315 (1962).

137. Kennerly, G. W. & Patterson, W. L. Kinetic Studies of Petroleum Antioxidants. *Ind Eng Chem* **48**, 1917–1924 (1956).

138. Burn, A. J. The mechanism of the antioxidant action of zinc dialkyl dithiophosphates. *Tetrahedron* **22**, 2153–2161 (1966).

139. Colclough, T. & Cunneen, J. I. Oxidation of organic sulphides. Part XV. The antioxidant action of phenothiazine, zinc isopropylxanthate, zinc di-isopropyldithiophosphate, and zinc dibutyldithiocarbamate, in squalene. *Journal of the Chemical Society (Resumed)* **3323**, 4790 (1964).

140. Howard, J. A., Ohkatsu, Y., Chenier, J. H. B. & Ingold, K. U. Metal Complexes as Antioxidants. I. The Reaction of Zinc Dialkyldithiophosphates and Related Compounds with Peroxy Radicals. *Can J Chem* **51**, 1543–1553 (1973).

141. Ferrari, E. S., Roberts, K. J. & Adams, D. A multi-edge X-ray absorption spectroscopy study of the reactivity of zinc di-alkyl-di-thiophosphates (ZDDPS) anti-wear additives: *Wear* **236**, 246–258 (1999).

142. Taylor, L. J. & Spikes, H. A. Friction-Enhancing Properties of ZDDP Antiwear Additive: Part I—Friction and Morphology of ZDDP Reaction Films. *Tribology Transactions* **46**, 303–309 (2003).

143. Zhang, Z. *et al.* Tribofilms generated from ZDDP and DDP on steel surfaces: Part 2, chemistry. *Tribol Lett* **19**, 221–229 (2005).

144. Powell, C. J. & Jablonski, A. Evaluation of Calculated and Measured Electron Inelastic Mean Free Paths Near Solid Surfaces. *J Phys Chem Ref Data* **28**, 19–62 (1999).

145. Jablonski, A. & Powell, C. J. Information depth and the mean escape depth in Auger electron spectroscopy and x-ray photoelectron spectroscopy. *Journal of Vacuum Science & Technology A: Vacuum, Surfaces, and Films* **21**, 274–283 (2003).

146. Heuberger, R., Rossi, A. & Spencer, N. D. XPS study of the influence of temperature on ZnDTP tribofilm composition. *Tribol Lett* **25**, 185–196 (2007).

147. Smith, M., Scudiero, L., Espinal, J., McEwen, J.-S. & Garcia-Perez, M. Improving the deconvolution and interpretation of XPS spectra from chars by ab initio calculations. *Carbon N Y* **110**, 155–171 (2016).

148. Crobu, M., Rossi, A., Mangolini, F. & Spencer, N. D. Chain-length-identification strategy in zinc polyphosphate glasses by means of XPS and ToF-SIMS. *Anal Bioanal Chem* **403**, 1415–1432 (2012).

149. Onyiriuka, E. C. Zinc phosphate glass surfaces studied by XPS. *J Non Cryst Solids* **163**, 268–273 (1993).

150. Brow, R. K. An XPS study of oxygen bonding in zinc phosphate and zinc borophosphate glasses. *J Non Cryst Solids* **194**, 267–273 (1996).

151. Chusuei, C. C., Brookshier, M. A. & Goodman, D. W. Correlation of Relative X-ray Photoelectron Spectroscopy Shake-up Intensity with CuO Particle Size. *Langmuir* **15**, 2806–2808 (1999).

152. Johnson, D. & Hils, J. Phosphate Esters, Thiophosphate Esters and Metal Thiophosphates as Lubricant Additives. *Lubricants* **1**, 132–148 (2013).

153. Ferrari, E. S., Roberts, K. J., Sansone, M. & Adams, D. A multi-edge X-ray absorption spectroscopy study of the reactivity of zinc di-alkyl-di-thiophosphates anti-wear additives. *Wear* **236**, 259–275 (1999).

154. Schroeder, S. L. M., Moggridge, G. D., Rayment, T. & Lambert, R. M. In situ probing of the near-surface properties of heterogeneous catalysts under reaction conditions: An introduction to total electron-yield XAS. *J Mol Catal A Chem* **119**, 357–365 (1997).

155. Thompson, A. *et al. X-Ray Data Booklet. Center for X-Ray Optics. [Tables].* http://www.osti.gov/servlets/purl/6359890-t6M9J7/ (1985) doi:10.2172/6359890.

156. Sitar, B., Merson, G. I., Chechin, V. A., Budagov, Y. A. & Pontecorvo, G. B. *Ionization Measurements in High Energy Physics.* vol. 124 (Springer Berlin Heidelberg, 1993).

157. Sauli, F. *Principles of operation of multiwire proportional and drift chambers.* (1977) doi:10.5170/CERN-1977-009.

158. Dorgham, A., Neville, A., Ignatyev, K., Mosselmans, F. & Morina, A. An *in situ* synchrotron XAS methodology for surface analysis under high temperature, pressure, and shear. *Review of Scientific Instruments* **88**, 015101 (2017).

159. Hu, J. J. *et al.* Transmission Electron Microscopy Analysis of Mo–W–S–Se Film Sliding Contact Obtained by Using Focused Ion Beam Microscope and In Situ Microtribometer. *Tribol Lett* **32**, 49–57 (2008).

160. Coultas, D. R. The Role of NOx in Engine Lubricant Oxidation. *SAE Int J Adv Curr Pract Mobil* **2**, 2020-01–1427 (2020).